Design and optimization of thin film organic solar cells

Ng, Ging Meng

2009

Ng, G. M. (2009). Design and optimization of thin film organic solar cells. Doctoral thesis, Nanyang Technological University, Singapore.

https://hdl.handle.net/10356/18707

https://doi.org/10.32657/10356/18707

DESIGN AND OPTIMIZATION OF THIN FILM ORGANIC SOLAR CELLS

NG GING MENG

School of Materials Science and Engineering

A thesis submitted to the Nanyang Technological University
in partial fulfillment of the requirement for the degree of
Doctor of Philosophy

2009

Acknowledgements

I would like to express my utmost gratitude to Dr. Zhu Furong and Prof. Subodh Mhaisalkar for their selfless support, continuous guidance throughout my Ph.D studies. I believe that I would not have been able to complete my studies without their constant encouragement, fruitful suggestions and guidance.

I would like to acknowledge, Dr. Achmad Zen, Dr. Chellappan Vijila, Dr. Thomas Kietzke, Ms. Elizabeth Lekha Kietzke, Mr. Goh Wei Peng, Ms. Liu Weiling, Ms. Tan Li Wei, Ms. Liew Pooi Kwan and Mr. Ong Kian Soo, for their help in device fabrication and the discussion of the experimental results.

Next, I would like to express my appreciation to Dr. Liu Hong and Mr. Chum Chan Choy for their assistance in photo mask and shadow mask design for device fabrication. In addition, a special thank to all the technical staff and my friends in Institute of Materials Research and Engineering (IMRE) and Nanyang Technological University (NTU) for their kind support and training on the process equipments.

Lastly, I want to take this opportunity to thank my family for their constant encouragement and blessing to pursue my Ph.D. studies.

Ng Ging Meng
Singapore, May 2009

List of Publications

Patent Applications:

1. Furong Zhu, **Ging-Meng Ng**, and Pooi-Kwan Liew, An Electrically Conducting Structure For A Light Transmissible Device, PCT/SG2008/000168, Filed On 6-May-08.

2. Zhi-Kuan Chen, Richard Shin, Prashant Sonar, **Ging-Meng Ng**, Achmad Zen and Kok-Haw Ong, n-type Semiconductors for Organic Electronics, ID submitted, 17-April-09.

3. Furong Zhu, **Ging-Meng Ng**, Chellappan Vijila, Wei-Peng Goh, Device architecture preferred for efficient operation of organic solar cells, new invention disclosure, under review.

Journal Publications:

1. **Ging-Meng Ng**, Elizabeth Lekha Kietzke, Thomas Kietzke, Li-Wei Tan, Pooi-Kwan Liew and Furong Zhu, 'Optical enhancement in semitransparent polymer photovoltaic cells' Applied Physics Letters, 90, 103505 (2007).

2. Chellappan Vijila, **Ging-Meng Ng**, Zhi-Kuan Chen, Furong Zhu and Soo-Jin. Chua, 'Charge transport studies in electroluminescent biphenylyl substituted PPV derivatives using time-of-flight photoconductivity method', Journal of Polymer Science Part B: Polymer Physics, 46, 1156-1166 (2008).

3. **Ging-Meng Ng**, Chellappan Vijila, Wei-Peng Goh, Furong Zhu, 'Translucent Polymer Solar Cells', ESC Transactions - 7th ISTC/CISC 2009, 18, 869 (2009).

4. **Ging-Meng Ng**, Wei-Peng Goh, Achmad Zen, Subodh Mhaisalkar and Furong Zhu, 'Optical design and optimization of tandem organic solar cells', to be submitted to Journal of Applied Physics.

5. **Ging-Meng Ng**, Chellappan Vijila, Achmad Zen, Wei-Peng Goh, Subodh Mhaisalkar and Furong Zhu, 'Lifetime improvement of translucent polymeric solar cells by preferable device operation mode', to be submitted to Applied Physics Letters.

6. Chellappan Vijila, **Ging-Meng Ng**, Wei-Peng Goh, Achmad Zen, Subodh Mhaisalkar and Furong Zhu, 'Effect of Al/ITO translucent cathode on the charge transport characteristics in organic solar cell' to be submitted to Organic Electronics.

Conference Presentations:

1. **Ging-Meng Ng**, Chellappan Vijila, Wei-Peng Goh, Furong Zhu, 'Translucent Polymer Solar Cells', Symposium A, E-MRS'09 Spring Meeting, June 8-12, 2009.

2. **Ging-Meng Ng**, Wei-Peng Goh, Weiling Liu and Furong Zhu, 'Translucent organic solar cells', Futuropolis 2058, Singapore, October 21-22, 2008.

3. **Ging-Meng Ng**, Wei-Peng Goh, Weiling Liu, Furong Zhu and Zhi-Kuan Chen, 'Integration of organic light transmissible devices for sensor applications', Inaugural A*STAR Scientific Conference, Singapore, November 18-19, 2008.

4. **Ging-Meng Ng**, Wei-Peng Goh, Pooi-Kwan Liew, Achmad Zen and Furong Zhu, 'Optical design and optimization of tandem organic photovoltaic cells', Symposium AA4, 2008 MRS Spring Meeting, San Francisco, March 25, 2008.

5. **Ging-Meng Ng**, Elizabeth Lekha Kietzke, Thomas Kietzke, Li-Wei Tan, Pooi-Kwan Liew, and Furong Zhu, 'ITO-based cathode for application in semitransparent organic photovoltaic cells', Symposium Z, 2007 MRS Spring Meeting, San Francisco, April 9-13, 2007.

6. **Ging-Meng Ng**, Elizabeth Lekha Kietzke, Thomas Kietzke, Li-Wei Tan, Pooi-Kwan Liew, and Furong Zhu, 'Semitransparent cathode for polymer photovoltaic cells', International Conference on Materials for Advanced Technologies 2007 (ICMAT-07), Singapore, July 1-6, 2007

7. **Ging-Meng Ng**, Chellappan Vijila, Zhi-Kuan Chen and Furong Zhu, 'Charge mobility studies in a series of novel PPV derivatives using a TOF-photoconductivity technique', 6th International Conference on Electroluminescence of Molecular Materials and Related Phenomena (ICEL-6), Hong Kong, August 7-10, 2006

IMRE Postgraduate Student Poster Competition:

1. **Ging Meng Ng**, Charge mobility studies in a series of novel PPV derivatives using TOF-photoconductivity technique, August 2006, Most Creative Award

2. **Ging Meng Ng**, Optical enhancement in semitransparent polymer photovoltaic cells, August 2007, Most Creative Award

3. **Ging Meng Ng**, Translucent polymeric photovoltaic cells, August 2008, the Third Best Poster Award.

Abbreviations

PV	Photovoltaic
PCE	Power conversion efficiency
OSC	Organic solar cell
EIL	Electron injection layer
HIL	Hole injection layer
Voc	Open circuit voltage
Jsc	Short circuit current density
FF	Fill factor
EQE	External quantum efficiency
n(λ)	Refractive index
k(λ)	Extinction coefficient
VASE	Variable spectroscopic ellipsometry
XPS	X-ray photoelectron spectroscopy
AFM	Atomic force microscopy
Rms	Root mean square
T(λ)	Transmittance
$\bar{A}(\lambda)$	Integrated absorptance
PSC	Polymeric solar cell
ITO	Indium tin oxide
RZ	Recombination zone
PhotoCELIV	Photoinduced charge extraction by linearly increasing voltage
CuPc	Copper-phthalocyanine

ZnPc	Zinc-phthalocyanine
C_{60}	Buckminster fullerene
MDMO-PPV	Poly[2-methoxy-5-(3,7-dimethyloctyloxy)]-1,4-phenylenevinylene
P3HT	Poly(3-hexylthiophene-2,5-diyl)
PCBM	1-(3-methoxycarbonyl) propyl-1-phenyl[6,6]C_{60}
C_{71}-PCBM	1-(3-methoxycarbonyl) propyl-1-phenyl[6,6]C_{70}
PCPDTBT	poly[2,6-4,4-bis-(2-ethylhexyl)-4H-cyclopenta[2,1-b;3,4-b']-dithiophene)-alt-4,7-(2,1,3-benzothiadiazole)]
AM1.5	Air mass 1.5
ECD	Equivalent circuit diagram
J-V characteristic	Current density-voltage characteristic
HOMO	Highest occupied molecular orbital
LUMO	Lowest unoccupied molecular orbital
R_{Sh}	Shunt resistance
R_s	Series resistance
D/A	Donor/Acceptor
Isc	Short circuit current
IPCE	Incident photon conversion efficiency
O_2	Oxygen
H_2O	Water/Moisture
N_2	Nitrogen
OLED	Organic light emitting diode
PEDOT:PSS	poly(3,4-ethylenedioxythiophene): polystyrene sulfonate

LiF	Lithium fluoride
Al	Aluminium
Au	Gold
Mg	Magnesium
Ag	Silver
Ca	Calcium
TCO	Transparent conducting oxide
PTCBI	3,4,9,10-perylenetetracarboxylic bis-benzimidazole
ZnO	Zinc oxide
SnO_2	Tin oxide
In_2O_3	Indium oxide
IZO	Indium Zinc oxide
AZO	Aluminum-doped Zinc oxide
FTO	Fluorine-doped Tin oxide
PCPDTBT	Poly[2,6-(4,4-bis-(2-ethylhexyl)-4H-cyclopenta[2,1-b;3,4-b']dithiophene)-alt-4,7-(2,1,3-benzothiadiazole)]
TiO_x	Titanium oxide
M_w	Molecular weight
CO_2	Carbon dioxide
IPCE	Incident photon conversion efficiency
CaO	Calcium oxide
BHJ	Bulk Heterojunction

Table of Contents

Abstract

The aim of this Ph.D. project was to undertake a systematic study to develop a technique for improving the performance of solution-processed translucent P3HT:PCBM-based solar cells over the two competing indexes: power conversion efficiency and transmittance, for stacking up or transparency. A comprehensive optical admittance analysis was applied to study the optical properties of conventional opaque and translucent P3HT:PCBM-based PSCs. The simulation uses the dispersive refractive index n(λ) and extinction coefficient k(λ) of P3HT:PCBM blend and other functional layers that were measured by VASE to calculate the optical absorbance and transmittance of P3HT:PCBM-based PSCs. The optimal device structure was obtained by maximizing the light absorption of the active layer (P3HT:PCBM) and the transmission of the whole translucent PSCs. AFM was used to examine the surface roughness of the P3HT:PCBM film prepared in this work.

Based on the optimal device parameters derived from the simulation, a 60 nm thick ITO was found to be optimal and was used to fabricate the translucent PSCs with the structure of glass/ITO/PEDOT:PSS/P3HT:PCBM(75nm)/Ca(10nm)/ Ag(10nm)/ITO(60 nm). In this device configuration, a top 60 nm thick ITO layer has two functions, a transparent cathode contact to improve the lateral conductivity and an optical index matching layer to improve optical transparency T(λ) and light absorptance $\bar{A}(\lambda)$ of the devices. The results of this work have yielded a translucent P3HT:PCBM-based polymer solar cells with an average transmission of more than 30% in the visible light wavelength range and a relatively high power conversion

efficiency of 1.7%. The simulation was also extended to study the photocurrent matching condition in tandem PSCs. In this work, it was found that the matching condition can be achieved when the following tandem PSC has an 95 nm thick ITO interlayer, e.g. Glass/ITO/PEDOT:PSS/P3HT:PCBM(50nm)/Ca(3nm)/Ag(3nm)/ITO (90nm) /PEDOT:PSS /P3HT:PCBM(200nm)/Al(100nm).

The stability of the solution-processed PSCs, e.g., glsss/ITO/PEDOT:PSS/P3HT: PCBM(200nm)/Al/ITO(60nm), was studied. The effect of the Al layer thickness in the translucent Al(5-10nm)/ITO(60nm) on charge mobility and the polymer/cathode interfacial properties were investigated using PhotoCELIV and XPS techniques, respectively. The translucent PSCs with Al(5nm)/ITO(60nm) cathode have an additional PhotoCELIV peak which was assigned to the trapped electrons that were formed due to the interaction between the PCBM molecules and the migrated oxides in the P3HT:PCBM layer.

Chapter 1

Introduction

1.1 Background and Motivations

The natural energy resources of fossil fuels, coal and natural gases have enabled industrialization and modernization development in the past few centuries. The demand for energy consumption continues to grow and there is a need to search for sustainable energy resources at the same time to develop technologies to improve the efficiency of the existing energy usage. To date, the major energy resources supporting this growth are still mainly dependent on the crude oil, coal and natural gas, as depicted in Figure 1.1, showing the world total primary energy supply [1]. The type of material for energy conversion is dictated by the availability and accessibility of the source, as well as its economic viability and the convenience it offers. Although there is a gradual movement from traditional sources to cleaner fuels, the former still remains as the most important source of energy due to the matured technology and infrastructure. However, they are not abundant on the Earth, and research into new sustainable and clean alternative energy sources has attracted great attentions worldwide. Figure 1.2 illustrates world oil production over the past few decades and the projected production in the subsequent years. As depicted from the oil production curve, production is expected to peak in the next few years. Consequently, oil production is expected to decline due to depleting resources. The pollutants generated due to burning of fossil fuels are another issue resulting in a serious global warming effect we are facing today. These pollutants are extremely harmful to the environment

such as large amounts of carbon dioxide released into the atmosphere as a result of burning fosil fuels.

This aside, there are reports which revealed that temperatures at the top of the permafrost layer have generally increased up to 3°C since the 1980s. The average annual Arctic sea ice extent has shrunk by 2.7 % per decade, decreasing as much as 7.4% in the summer [2]. The consequences of such temperature changes have spawned numerous hard-hitting natural disasters such as fiercer storms. Such frequent events are likely to have a more damaging effect on mankind and other life forms on Earth within the next few decades. The seriousness of the side effects coupled with a finite amount of fossil fuels catalyzes the need to seek for an alternative source of energy. Despite all the seemingly negativities, we have renewable energy resources in the fray which are neither finite nor detrimental to the environment. One of the renewable energy resources which is being intensively investigated is photovoltaic energy.

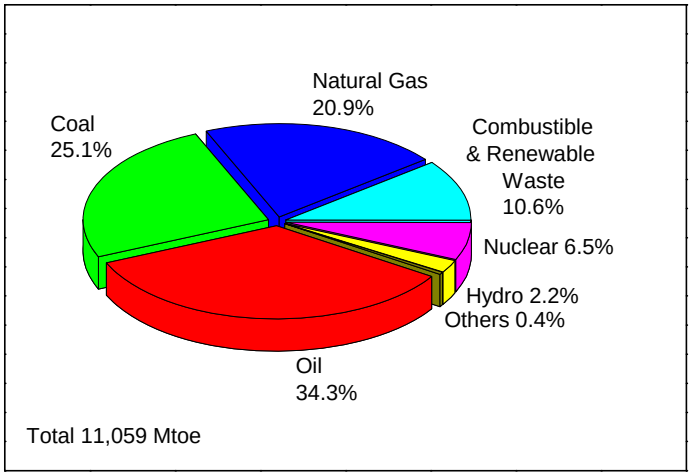

Figure 1.1: World total primary energy supply (2004) by source. Note: Mtoe is million tons of oil equivalents. [1]

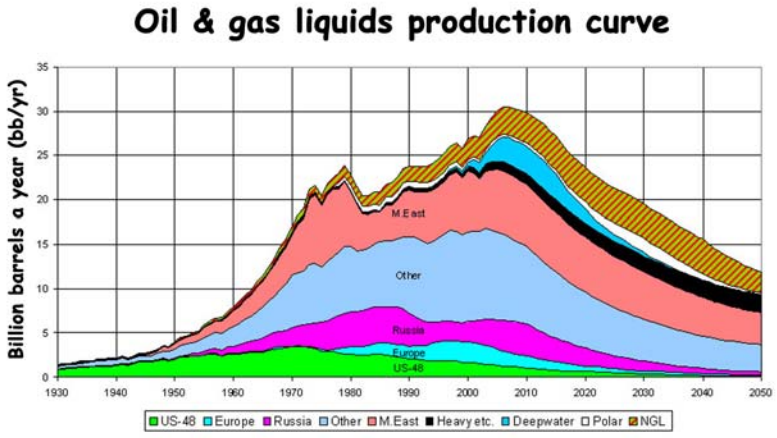

Figure 1.2: Oil and gas liquids production curve, predicted by Uppsala Hydrocarbon Depletion Study Group, UHDSG (Sweden) [3]

1.2 Photovoltaic Energy

The term "photovoltaic" comes from the combination of the Greek word, φώς:*phos*, meaning 'light', and the name of the Italian physicist, Volta, after whom the volt (and consequently voltage) is named. It literally means light and electricity. The Sun presents us with an almost infinite source of energy. Solar energy can be converted into different forms of energy, such as heat and electricity. It does not emanate harmful radiation (with the exception of ultra-violet radiation) as compared to radiation from nuclear energy. The solar energy is not only environmental friendly, but impinges the Earth's surface with an amazing total amount 32×10^{24} joules of energy per annum. The conversion of solar energy into electricity is known as photovoltaic energy conversion. A PV cell, also known as solar cell, is the technology that converts the solar energy directly into electricity. Imagine if a mere 0.1% of the Earth's surface is covered by solar cells, with PCE of 10% each, it would satisfy our present energy needs. A variety of solar cells have been developed using conventional

inorganic semiconductors and more recently the organic semiconductor materials. Each of PV technologies has its own advantages, applications and the markets. Figure 1.3 shows the development trend of the best research solar cell efficiency achieved to date. According to Figure 1.3, the research of inorganic solar cells was initiated almost one decade earlier than its organic counterpart. Intensive research and development in inorganic solar cells in the past two decades have resulted in much superior device efficiencies than that of the OSCs.

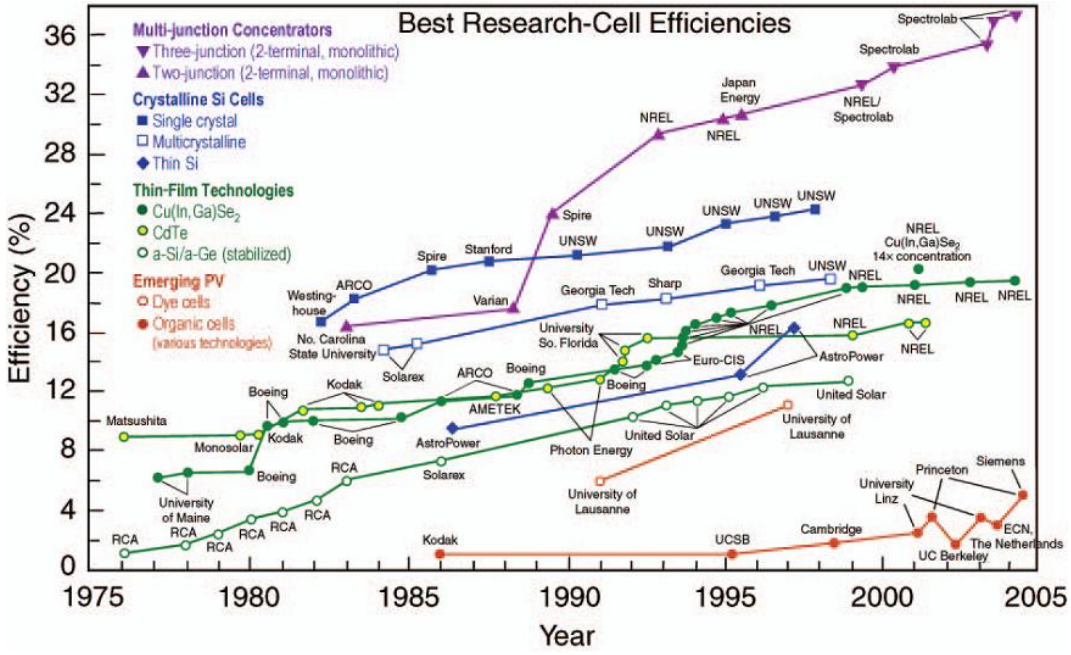

Figure 1.3: Highlights of the research progress in PCE made in different types of solar cells since 1970s (from National Renewable Energy Laboratory).

The first discovery of inorganic silicon p-n junction based solar cells was reported by Chapin, Fuller and Pearson from Bell labs in 1954 [4]. Solar panels based on the conventional inorganic solar cells have been in use since the 1970's and have primarily been built from crystalline silicon using technologies very close to those used in the semiconductor industry. The highest PCE for single crystal silicon solar cells has reached ~24%. Polycrystalline silicon solar cells are less expensive to

manufacture but offer lower efficiencies than the single-crystalline approach. Although the production of Si-based PV cells is approaching 3 GW/year with billion dollars in worldwide revenue, this figure is only representing a very small proportion of total energy generated (<1%) in the world [5]. Other PV materials such as gallium arsenides and cadmium tellurides are also penetrating into the PV market, with a desire to reduce the manufacturing cost at the same time improving the cell efficiency [6]. Recently, an inorganic solar cell with 40% of PCE was demonstrated using a metamorphic GaInP/GaareAs/Ge multi-junction structure [7]. Silicon-based solar cell technology is still dominant in today's PV market due to the maturity of the technique, sufficient material supply, e.g., 27.7% in the crust of the Earth [8], and high module efficiency (~20%). However, the cost relating to power generation is one of the several challenges with the Si-based PV technology. The production of these crystalline silicon solar cells generally requires high processing temperatures (400-1400ºC) and ultra high vacuum conditions (in the region of 10^{-9} mbar). It also involves multiple complicated photolithography steps, resulting in relatively high manufacturing costs. Hence, the development of the emerging organic and nanostructure based PV technology has attracted a lot of interests due to its great potential of low cost non-vacuum process PV technology [9]. Presently, such a technology is not a tangible reality yet. The inexpensive fabrication process such as solution-process techniques, the flexibility and light weight makes this technology attractive for application in new markets such as mobile electronics, digital applications, home appliances, outdoor lifestyle, automotive etc.

1.3 Organic Photovoltaics: Opportunities and Challenges

Silicon-based solar cells are proven PV technology, but they suffer from relatively high costs. Organic and organic-inorganic hybrid polymer-based bulk-heterojunction solar cells offer a potentially much cheaper alternative way to harness solar energy [10]. Considerable enhancements in device efficiencies are needed if this technology is to become a viable option for large scale energy production. The development of OSCs is still in its early stages, particularly the design and optimization of their structures and the performances. To date, the best PCE reported for polymer-based bulk-heterojunction cells is around 5% [10]. However, theoretical studies suggest values of at least 10% (which currently marks the minimum for a commercially viable power source) are obtainable using conjugated polymer donors with a fullerene acceptor [11].

Since the discovery of electro-luminescence behavior in conjugated polymers [12], there has been a tremendous effort to develop PV devices based on semiconducting conjugated polymers. A conjugated organic system is made of an alternation between single and double carbon-carbon bonds. Single carbon-carbon bonds, also known as σ-bonds, are associated with localized electrons, whereas double carbon-carbon bonds contain both a σ-bond and a π-bond. The electrons associated with the π-bond are generally much more mobile than those with the σ-bond due to the mutual overlapping of π-orbitals along the conjugation path, leading to the delocalization of the wave functions over the conjugated polymer backbone. The electrons associated with the π-bond can hop from one site to another between carbon

atoms. The electronic states in π-bands can be either empty, called lowest unoccupied molecular orbital (LUMO) or filled with electrons, called highest occupied molecular orbital (HOMO). The energy distance between HOMO and LUMO or the bandgap of organic semiconductors ranges from 1.0eV to 4.0 eV. The π-electron system has all the essential electronic features of organic materials, such as light absorption and emission, charge generation and transport which are crucial for application in OSCs.

The maiden discovery of PV effect for semiconducting polymers came as early as 1959, when a single anthracene crystal was studied [13]. The cell exhibited a photovoltage of 200 mV with an extremely low efficiency. Much progress in OSC has been made since the discovery of the PV effect of chlorophyll in plants by C.W. Tang in 1975 [14]. In this report, an OSC with a metal-chlorophyll-metal sandwiched structure of Al/Chl/Hg or Al/Chl/Au was shown to have a V_{oc} up to 500mV and a PCE of 10^{-3}%. That was the highest PCE reported for a single layer OSC. After this breakthrough, chemists began to work feverishly to synthesize novel organic small molecules or pigments [15, 16, 17, 18] and semiconducting polymers [19, 20, 21, 22]. This eventually heralded the development of OSCs, especially during the late 20^{th} century. Many years of research have shown that the typical PCE of PV devices based on single-layered (or homo-junction) organic materials still remain below the 0.1% mark.

With the discovery of merocyanine dyes in the early days, OSCs based on single layers, sandwiched between two metal electrodes comprising of different work functions, display a vast improvement. The power conversion efficiency reached a

remarkable value of 0.7% [23, 24]. The rectifying effect of these single layer devices was attributed to the asymmetric injection of electrons and holes into the π-π^* conjugated system in the organic materials, and to the formation of Schottky-barrier between the p-type (hole transporting) organic materials and the low work function metal electrode. However, the low PCE of single layered OSCs made them unsuitable for any possible applications.

A breakthrough in PCE of OSCs was achieved by introducing a bilayer heterojunction. In this configuration, two organic semiconducting materials (electron and hole transporting or n-type and p-type) are sandwiched between two electrodes having different values of work function. The concept of bilayer OSCs was first proposed by Tang [25], achieving a 1% PCE by using a phthalocyanine derivative as the p-type semiconductor and a perylene derivative as the n-type semiconductor. Subsequently, after the introduction of the bulk heterojunction, the PCE was boosted to 5% by using a P3HT (poly(3-hexylthiophene-2,5-diyl)) and PCBM (1-(3-methoxycarbonyl) propyl-1-phenyl[6,6]C60) blend system [26, 27] (see section 2.3).

OSCs with multilayered architecture are very promising for achieving high PCE. Organic semiconductors as the active components in PV devices have many advantages in terms of large area reproducibility, cost effectiveness, chemical tenability and mechanical flexibility. As such, there is a palpable sense of great expectation. This field is still in its development stage, particularly regarding aspects like design and optimization of device structures [26, 28, 29, 30]. There are two approaches to fabricate OSCs. While sublimed small molecules come with the

advantage of easy multilayer preparation, solution processed polymers promise a low cost and large area production by technologies such as reel to reel, screen or ink jet printing [31].

There is another type of solar cell based on organic-inorganic hybrids called electro-chemical solar cells or dye-sensitized solar cells (DSSCs). Using titanium dioxide in conjunction with an organic dye and a liquid electrolyte [32], PCEs exceeding 6% are already attained [33]. They are about to enter the commercial market due to the relatively low production costs as compared to silicon solar cells. However, the encapsulation of DSSC with liquid electrolyte still remains a challenge.

The advantage of OSCs over DSSCs is, predominantly, the absence of a liquid electrolyte, which generates problems during encapsulation. In comparison with the silicon solar cells, the fabrication process of OSCs is relatively simple and offers potentially low cost PV products that can be fabricated using roll-to roll process. Although the charge carrier mobility in an organic semiconductor is not as high as the conventional inorganic solid-state semiconducting materials, the organic semiconducting materials possess high absorption coefficient (usually $\geq 10^5$ cm^{-1}) [34] promising light absorption in a very thin film (~100nm). The layer thicknesses can be kept thin while simultaneously maintaining good charge transport to the device. In addition, the outstanding mechanical flexibility of organic semiconductor film provides good opportunity in forming it on flexible substrate. This forms the reason for rapid progress in the field recently.

However, there are challenges hindering development of OSC, such as low PCE and poor device lifetime. Limited light absorption of the solar spectrum and a relatively low V_{oc} are the two main factors limiting the PCE of current OSC. Apart from the need to improve device efficiency, stability of OSC is another essential challenge to be overcome before the products can be commercialized. Organic semiconductors are known for their instability under combined exposure to light, oxygen and moisture. Rapid degradation of the material occurs under these conditions. Hence, protection from air and humidity is absolutely necessary if the long lifetime of the cell is expected.

1.4 Thesis Objectives

It is clear that the limited utilization of the solar spectrum and the relatively poor lifetime are the two main factors hindering multilayer thin film OSC from commercialization. One of the solutions to enhance the utilization of solar spectrum is to use tandem structure solar cells. The tandem OSC is an emerging technology and has attracted a lot of research interests worldwide in recent years. This is because the unit OSCs in the tandem devices can be chosen to absorb different parts of the solar spectrum therefore to have a broad spectral response for efficient energy conversion. In order to achieve high PCE, the structure of the stacked OSCs must be optimized.

One of the challenges of the tandem OSCs is to ensure a perfect photocurrent matching as the tandem solar cells involving several sub PV units. An electrically conductive and optically transparent charge recombination interlayer is also desired. The carrier collection capability of the recombination interlayer is crucial in a tandem

OSC and is dependent on HOMO and LUMO levels of donor and acceptor in the adjacent sub PV units. This Ph.D. project has been focused on studying and optimizing the performance of solution-processed OSC with the following objectives:

1. Study the interference enhancement response to maximize the efficiency of multilayer polymeric bulk heterojunction solar cells using optical admittance analysis.

2. Develop high performance low process temperature ITO-based transparent cathode, fabricate and optimize the structure of translucent and tandem polymeric bulk heterojunction solar cells for enhanced photovoltaic performance.

3. Undertake a systematic study to develop a technique improving the performance of translucent organic solar cells over the two competing indexes: power conversion efficiency and optical transparency, for stacking up or transparency.

4. Understand the charge transport properties in polymeric solar cells using photoCELIV technique.

5. Investigate the role of polymer/electrode interfacial properties on the efficiency and stability of solution-processed polymeric bulk heterojunction solar cells.

1.5 Organization of This Thesis

This thesis consists of seven chapters, starting with an introduction Chapter followed by an overview of organic PVs in Chapter 2. The organic materials for application in OSC will first be introduced. The fundamentals of OSCs including the excitonic energy conversion process, equivalent circuit diagram and the physical meaning of important PV parameters such as V_{oc}, J_{sc}, FF, EQE and PCE are also described in Chapter 2. The materials processing techniques, the device fabrication conditions are described in Chapter 3. Experimental materials including hole transporting layer, active layer (P3HT:PCBM), electrode contacts and the process optimization are outlined in Chapter 3. The materials characterization techniques and the device fabrication procedures are also reviewed. The absorption spectrum, n(λ) and k(λ) of the functional materials used in OSC fabrication were measured using UV-Vis Spectrometer and VASE, respectively. XPS and AFM were used to study the surface morphological and electronic properties, respectively. The performance and the stability of the OSCs were also investigated using I-V and EQE measurement systems.

The optical properties of the organic thin films and the OSC systems are discussed in detailed in Chapter 4. The rms roughness of P3HT:PCBM films optimized for OSCs in this work was less than 1nm, suggesting a smooth film surface morphology at organic/electrode interface for optical enhancement by the simulation. The thickness evaluation and the model used in VASE to determine the n(λ) & k(λ) values are illustrated. By gathering the film thickness, n(λ) & k(λ) values of P3HT:PCBM thin film, optical admittance analysis was used to calculate the optimal condition for OSC architectures. It is shown that a thicker active layer did not always

exhibit a higher light absorption due to the strong interference effect, which dominates in the thin film system. The devices were fabricated and characterized based on the parameters calculated from the simulation. The experimental results agree well with the device parameters optimized by the optical admittance analysis.

The application of the ITO-based translucent cathode in OSCs is discussed in Chapter 5. The processing of low temperature ITO and its electrical and optical characteristics were discussed. The ITO-based translucent cathode serves as an optical index matching layer to enhance two competing processes, i.e. $T(\lambda)$ and $\bar{A}(\lambda)$ for a P3HT:PCBM type of PSC. The performance of the translucent PSCs was characterized and compared with the reference conventional PSC. The experimental results showed enhancement in the $T(\lambda)$ when an ITO-based cathode is used as an optical index matching layer, which exhibited a same agreement with the simulated results optically. This device was laterally integrated and shown a success in powering up small toys. The ITO-based translucent cathode was shown to be suitable for the application as RZ in tandem PSC which will be discussed in this chapter.

The results of the PSC stability are presented in Chapter 6. In this work, the device stability was correlated to the exciton generation profile in an OSC, which is directly proportional to the light absorption profile in a PSC and was calculated using the optical admittance analysis. The effect of the charge transport, interface properties at the polymer/cathode and their influence on device stability was investigated using PhotoCELIV and XPS techniques. A summary of achievements of this work is given in Chapter 7 with some recommendations for future research on the topic.

Chapter 2

Overview of Organic Photovoltaics

2.1 Materials for Application in Organic Photovoltaics

Generally, organic PV materials have a unique system of delocalized π electrons. These materials are categorized as conjugated polymers since they behave like a semiconductor. They can absorb sunlight, create photogenerated charge carriers and provide a pathway to transport the charge carriers. Nowadays, OSC research either focuses on solution processed organic semiconducting polymers or vacuum deposited small molecule materials. Phthalocyanine is a representative p-type or hole conducting material that works as an electron donor, e.g., CuPc and ZnPc. The perylene and its derivatives are examples of n-type or electron conducting materials that work as electron acceptors. Phthalocyanine and perylene, bulkminster fullerene and their derivatives are small molecule based materials which are often incorporated into sublimed OSCs. The molecular structures of these small molecule organic materials are depicted in Figure 2.1.

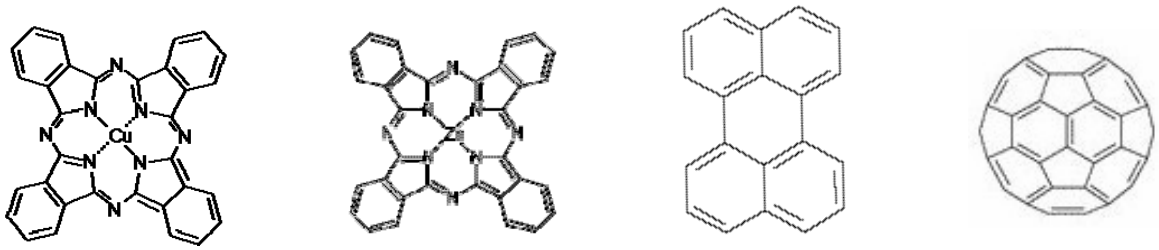

Figure 2.1: Some organic molecules commonly applied in sublimed OSCs: CuPc, ZnPc, perylene and fullerene.

Usually, organic semiconductors have an optical bandgap of around 2.0 eV. The intrinsic charge carrier concentrations at room temperature in the dark are nearly negligible. Since the charge carrier mobilities are relatively small as compared to their inorganic counterparts, they can be nearly regarded as insulators. However, there are a few ways to increase the charge carrier concentration through methods such as chemical, photochemical or electrochemical doping. These procedures introduce extrinsic charge carriers into the organic semiconductors. Donor or p-type materials can be doped by exposing to oxygen or other strong oxidizing agents such as iodine. The doping effect is achieved by transferring an electron from the ground state of an organic semiconductor to the oxidizing agent, resulting in an increased charge carrier concentration in the hole conductor. However, gas doping is not very easy to control. Another common approach is to form a blend or mixture by co-evaporating the donor and acceptor materials. A mixture of CuPc and C_{60} or its derivatives is often used because C_{60} is reported as a strong electron acceptor [35]. This mixture of CuPc:C_{60} system does not show an improved behaviour in charge transport properties when it is in the dark, but it leads to an enhancement in photoconductivity under illumination [36, 37, 38]. This is a result of the photoinduced charge transfer [39] and hence, this process is known as "photodoping" [20].

For conjugated polymers, some important examples of hole conducting donor type polymers are MDMO-PPV and P3HT. On the other hand, electron transporting (acceptor) solution processable materials include the derivatives of C_{60}, namely PCBM and C_{71}-PCBM. The molecular structures of MDMO-PPV, P3HT, C_{61}-PCBM and C_{71}-PCBM are depicted in Figure 2.2. These materials show electroluminescence

and photoluminescence properties, and can be solution-processed due to the presence of the side chains that improve the solubility of the materials [12, 40, 41]. The best reported PCE so far (around 5-6%) [26, 27] are based on mixture of these types of donor/acceptor materials. For the device architectures, donor polymers and acceptor fullerene derivatives can either in bilayer or in blend structures when used for devices. These will be explained in detail in section 2.4.

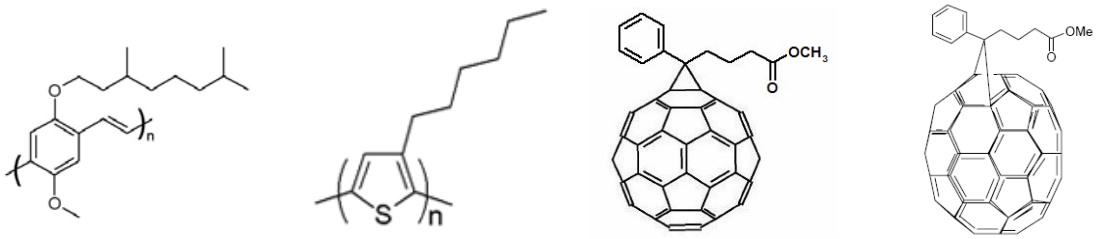

MDMO-PPV P3HT C61-PCBM C71-PCBM

Figure 2.2: Several solution processable conjugated polymers and fullerene derivative used in OSCs.

Although remarkable efficiencies have been achieved, organic PV materials such as P3HT, MDMO-PPV, PCBM have only utilized the short wavelength part of the solar spectrum, leaving the long wavelength part unused. The limited light absorption of these materials leads to a lower PCE (~5%) value as compared to silicon solar cells (~30%). There has been an increased interest in synthesizing novel organic PV materials to fully utilize the low band gap region of the solar spectrum. Recently, J. Peet et al. reported a novel low band gap conjugated polymer [42]. A PCE of 5.5% for solution processed PSC using PCPDTBT with alkane dithiols was achieved. Alkane dithiols are believed to control the morphology of PCPDTBT in the drying process. This achievement is encouraging because it demonstrated that higher

efficiency can be realized by using low band gap conjugated polymeric materials. However, the low band gap materials are unable to fully utilize the solar spectrum with the single cell configuration as well since the short wavelength part of solar spectrum will be neglected. One of the possible ways to fully utilize the solar spectrum is to form a tandem structure by integrating both organic materials with different energy band gaps together. Figure 2.3 shows the comparison between the absorption coefficients of the commonly used PV materials and the AM1.5 solar spectrum. As illustrated in the diagram, the overlapping region of the materials still does not cover the entire solar spectrum. This is one of the main inferiorities as compared to silicon (bandgap = 1.17eV), which can extend up to 1100nm.

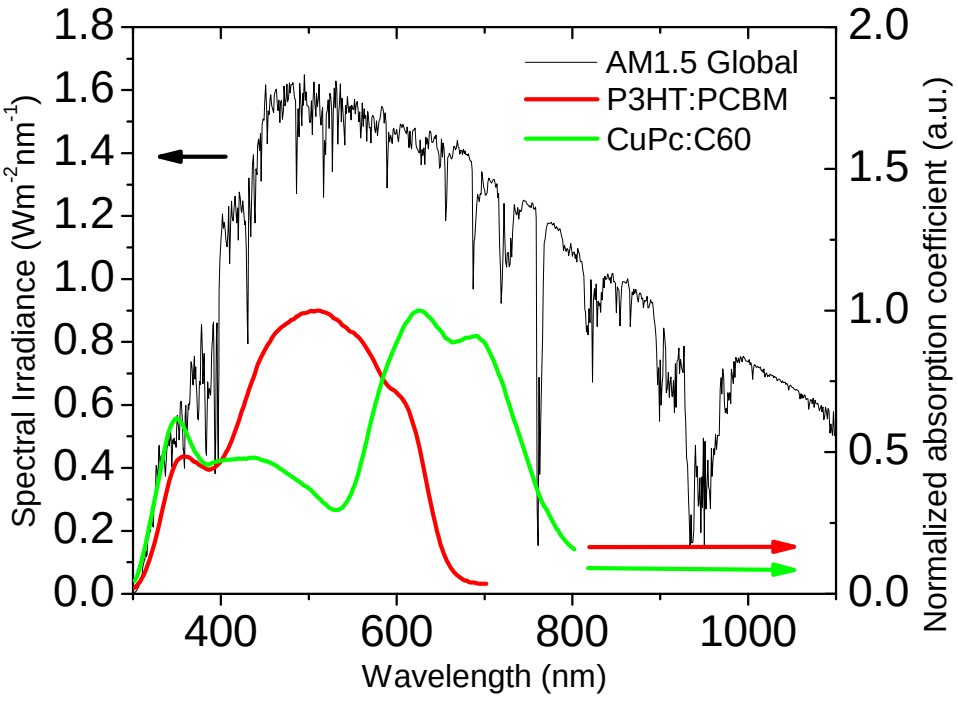

Figure 2.3: Comparison between the absorption coefficients of the films of commonly used OSC materials and the simulated AM1.5 solar spectrum.

2.2 Fundamentals of Organic Solar Cells

In the following section, the excitonic energy conversion process, ECD and the I-V characteristics of OSCs will be discussed.

2.2.1 Excitonic Energy Conversion Process

The excitonic energy conversion process of incident photons into electricity in OSCs can be divided into five major steps. Shown schematically in Figure 2.4, the different steps of the conversion process together with the prevalent loss mechanisms in OSCs are described below:

1) Light absorption and spectral mismatch:

The first step, which defines the workability of an OSC, is the response ability of the active semiconductor materials to solar energy. Most semiconducting polymers have a higher absorption coefficient ($\alpha \sim 10^5$ cm^{-1}) than that of crystalline silicon ($\alpha \sim 10^4$ cm^{-1}). This means that a thinner layer of semiconducting polymer is able to absorb the same amount of sunlight as compared to a thicker crystalline silicon. However, due to the mismatch factor in the refractive indices of semiconducting polymers and air, an appreciable amount of the light is lost due to reflection. The reflection loss at the interface of two materials becomes significant in a multilayered thin film OSC because it reduces the light absorption in the active layer. Inefficient light absorption in OSCs is a major impediment in achieving higher PCEs so far.

From a materials point of view, the incident photon energy, $E = h\upsilon$ has to be larger than or equal to the energy difference between the HOMO and the LUMO, or simply called the bandgap energy, of the semiconducting polymers. Due to the large

bandgap in most semiconducting polymers, only a small fraction of the incident solar light is absorbed. A material with a band gap of 1.1eV, such as Si, is able to absorb 77% of the solar irradiation on Earth. However, most of the commercially available semiconducting polymers have bandgaps higher than 2.0 eV, which is a limiting factor in harvesting sunlight [26]. Hence, polymers with lower bandgaps are desired as they are able to harvest the remaining unutilized solar energy in the long wavelength range. When the sub-cells with different spectral responses stacked together to form a tandem structure, theoretically, a high energy conversion in the OSCs can be expected.

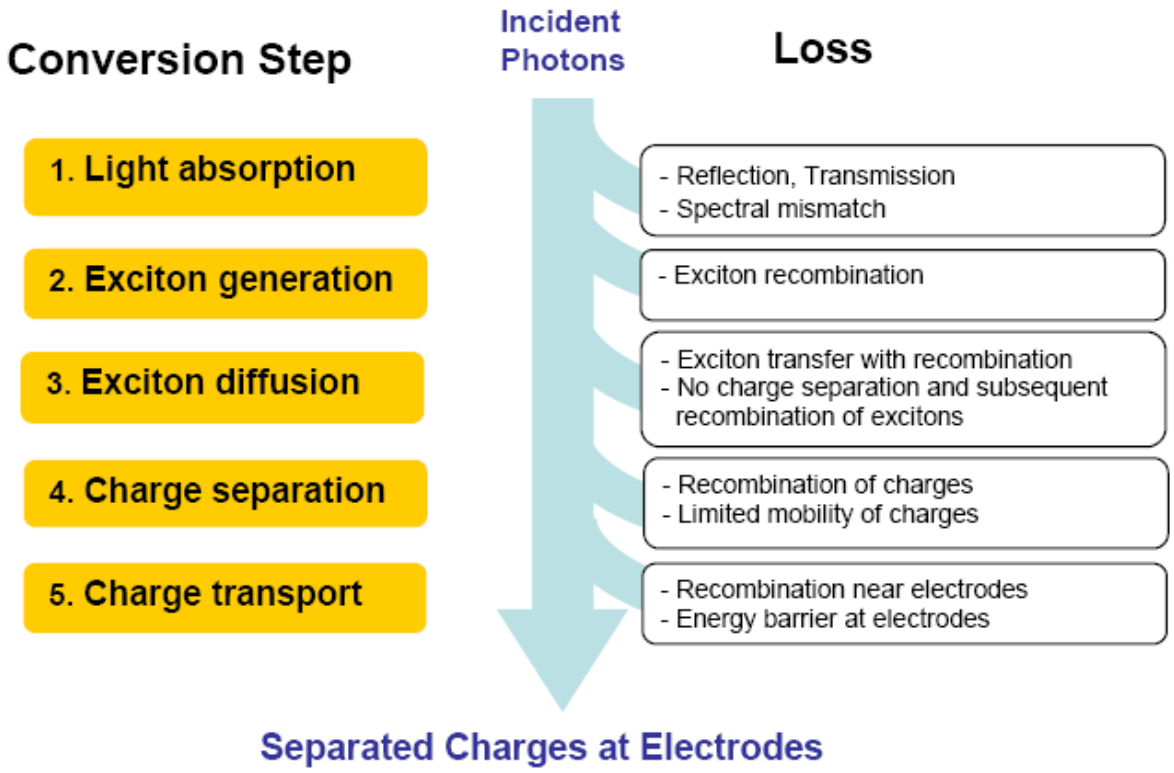

Figure 2.4: The conversion steps and the corresponding loss mechanisms for the conversion of photons to electrons in semiconducting PSCs.

2) Exciton generation:

The primary photoexcitations in organic materials do not directly and quantitatively lead to free charge carriers but to coulombically bound electron-hole pairs, or called excitons. The exact binding energy of this exciton is still under debate but it is thought to be in a range of 200-500 meV [43, 44]. With that, the exciton binding energy for conjugated polymers is roughly one order of magnitude larger than that of inorganic semiconductors like silicon, where photoexcitations typically lead to free carriers directly at room temperature. It is estimated that only 10% of the photoexcitations will lead to free charge carriers in pure conjugated polymers [45].

3) Exciton diffusion:

For efficient dissociation of excitons, strong electric fields are necessary to break the coulombically bound electron-hole pairs. Such localized electric fields can be supplied via externally applied electrical fields as well as via interfaces. At the interface, a strong electric field exists since there is an abrupt difference in the potential energy. Photoinduced charge transfer can occur if an exciton reaches such an interface within its lifetime. Therefore, an exciton diffusion length becomes an important parameter to be considered as it not only limits the thickness of a bilayer (donor-acceptor configuration), it also affects the PCE of the whole device. In a bulk heterojunction configuration, the exciton diffusion length should be of the same order of magnitude as the donor-acceptor phase separation length. Otherwise, excitons decay via radiative or non-radiative path ways before reaching the interface. Exciton diffusion length in polymers and in organic semiconductors is usually in the range of 10 to 20nm.

4) Charge separation:

It is reported that fullerene and its derivatives are strong electron acceptors [46]. They are able to break photoexcited excitons apart into free charge carriers efficiently. Ultrafast photophysical studies showed that the photoinduced charge transfer in such blends happens within a time scale of 45 fs. This is much faster than other relaxation processes such as photoluminescence (usually occurs at around 1 ns) [47]. The reverse electron transfer from fullerenes back to the polymer is extremely slow. Thus, the quantum efficiency of this dissociation process is close to 100 % at the polymer-fullerene interface. Furthermore, the separated charges in such blends are metastable at low temperatures.

5) Charge transport:

Photogenerated charges in OSCs have to be transported to the respective electrodes within their lifetime. These charge carriers are unable to travel independently unless a driving force is applied. A chemical potential gradient in electrons and holes is built up at the donor-acceptor interface. This gradient is generally defined by the difference between the HOMO of the donor and LUMO of the acceptor. This internal electric field determines the maximum V_{oc} and contributes to a field-induced drift of the charge carriers. In order to enhance the charge transport, asymmetrical contacts are used , e.g., a cathode with a low work function for electron collection and an anode with a high work function for hole collection, to generate an external field in short circuit conditions according to a metal-insulator-metal configuration [48]. The charge transport is also dependent on the morphology of the active layers. The donor and acceptor have to generate a percolation pathway for the photogenerated charge

carriers to travel before it is successfully collected by the electrodes. This is also one of the challenges in the field where numerous ways are performed to control the morphology of the active layers. Methods such as thermal annealing and using different kinds of organic solvents are adopted so that a donor-acceptor phase separation in a range of 10-20 nm can be achieved.

2.2.2 Equivalent Circuit Diagram

To understand the electronic behavior of a solar cell, it is useful to create a model which is electrically equivalent, and is based on discrete electrical components with known behavior. An ideal solar cell may be modeled by a current source in parallel with a diode. In practice, there is no ideal solar cell hence a shunt resistance and a series resistance component are added to the model. The resulting equivalent circuit diagram (ECD) of a solar cell is shown in Figure 2.5. Since the loss mechanisms are basically the same for organic and inorganic solar cells, the ECD can be similarly applied to OSCs, even though the specific physical processes are significantly different. The basic electrical components can be described as follows:

- The photogenerated current, I_G, is the resulting current from the dissociation of excitons into free electrons and holes after photon absorption. I_G does not take into account any recombination but only considers the charge carrier creation efficiency.
- The shunt resistor, R_{Sh}, represents the recombination of electrons and holes near the exciton dissociation site (donor/acceptor interface) before the charge transport within the bulk can occur.

- The series resistor, R_S, takes into account the mobility of charge carriers in the bulk of the solar cell. The carrier mobility is influenced by the defects, traps, interface barriers and space charges in the device. R_S increases with the thickness of the device since the distance that the charges travel to the respective electrode increases.
- The diode, D, describes the asymmetric conductivity in the OSC due to the built in field in a D/A cell (difference between the acceptor LUMO and the donor HOMO) or the nature of the semiconductor electrode interface (blocking contact) in single layered cells.
- An external load resistor, R_L, indicates that a solar cell is contacted to an external load. Alternatively, a source meter can be connected to the cell and it measures the I-V characteristics of a solar cell.

For an ideal solar cell, R_{Sh} would be infinitely large and R_S would be zero. The value of R_{Sh} for an inorganic solar cell is larger than 1000 Ohms and that of R_S is just a few Ohms. These values can be significantly different for organic devices since the mobility is usually lower (increasing R_S) and charge recombination can be an issue (lowering R_{Sh}).

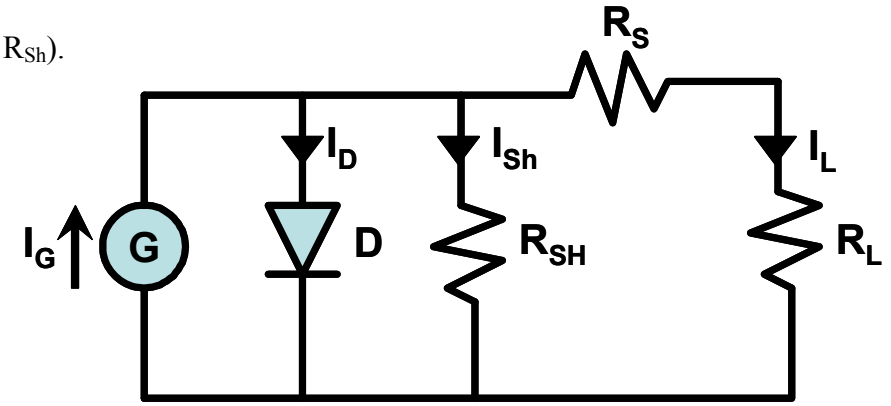

Figure 2.5: Equivalent circuit diagram for a typical solar cell.

In addition to the simplified ECD for solar cell shown in Figure 2.5, a more comprehensive ECD for organic devices has been proposed and is shown in Figure 2.6. The revised ECD may comprise of extra electrical components which takes into account the additional loss mechanism.

- A diode D_2 takes into account a possible extra blocking contact at the electrode. For example holes blocking the contact at the ITO electrode. This diode is always present but seldom considered in the analysis.
- An extra shunt resistor, R_{sh2}, is added to take into consideration possible shorts due to pinholes or significant conductivity of the bulk material. It may also account for recombination losses near the electrodes. The effect of R_{sh2} is considered in R_{sh} if R_s is considerably smaller than any of the two shunts.
- A capacitor, C, that takes into account for the charging and discharging effects in the device. Since the device area is usually much larger than the device thickness, the capacitance can become an important part of the device ($C=\varepsilon A/d$).
-

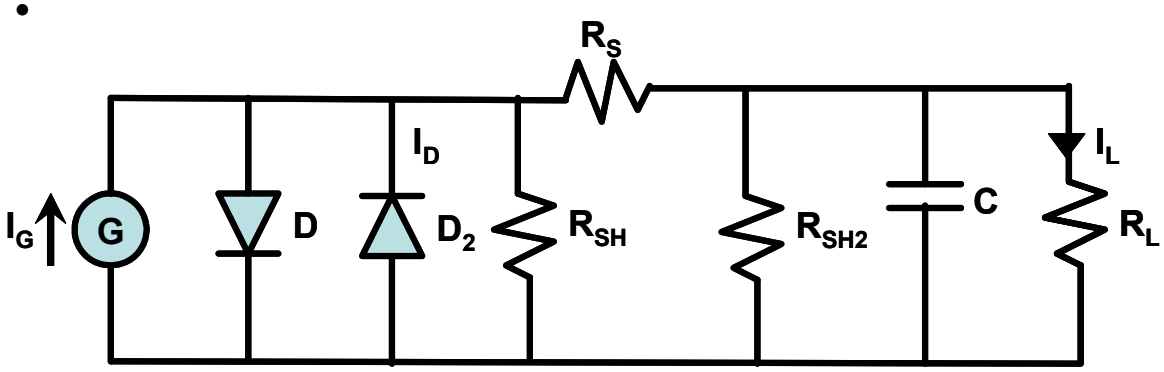

Figure 2.6: Extended equivalent circuit diagram for a solar cell.

This extended ECD can be used to analyze I-V curves measured for an organic solar cell. The shape of the curve obtained from the I-V measurement can be corresponded to the electrical components in the ECD. From there, a correlation between the electrical components and the physical properties of the solar cell can be concluded. Problems can then be figured out and possible actions be undertaken to improve the devices.

2.2.3 Current-Voltage Characteristics

The current-voltage characteristics of an OSC in dark condition and under illumination are depicted in Figure 2.7. Since organic semiconductors exhibit extremely low intrinsic carrier concentrations, the metal-insulator-metal system can be the best model to explain the current-voltage characteristics of an OSC. The energy diagram, based on the metal-insulator-metal theory, is depicted for each point in Figures 2.7(a) and (b). In the dark, there is almost no current flow (no intrinsic carriers) in the device unless an external forward bias is applied. The current will increase substantially when the forward bias is larger than the built in potential of the device (dotted curve). Under illumination condition, the current of a solar cell flows in the opposite direction, againsting the injected current as shown in Figure 2.7 (a) (point a). As it reaches point b, the maximum photocurrent generated is obtained under short circuit conditions or called I_{sc}. If the bias is continuously applied after this point, it reaches a flat band condition where the photogenerated current equates to zero (point c). At this point, the voltage is denoted as the V_{oc}. Between point b and c, it is also the forth quadrant of the I-V characteristic, the device generates power which is equal to the product of the applied voltage and photogenerated current. At a certain point, the

power generated reaches its maximum. In order to determine the PCE of a solar cell, this maximum generated power is needed to compare with the incident light power intensity. Therefore, the PCE can be calculated by using Equation 2.1.

$$PCE, \eta = \frac{P_{out}}{P_{in}} = \frac{I_{MPP} \times V_{MPP}}{P_{in}} \tag{2.1}$$

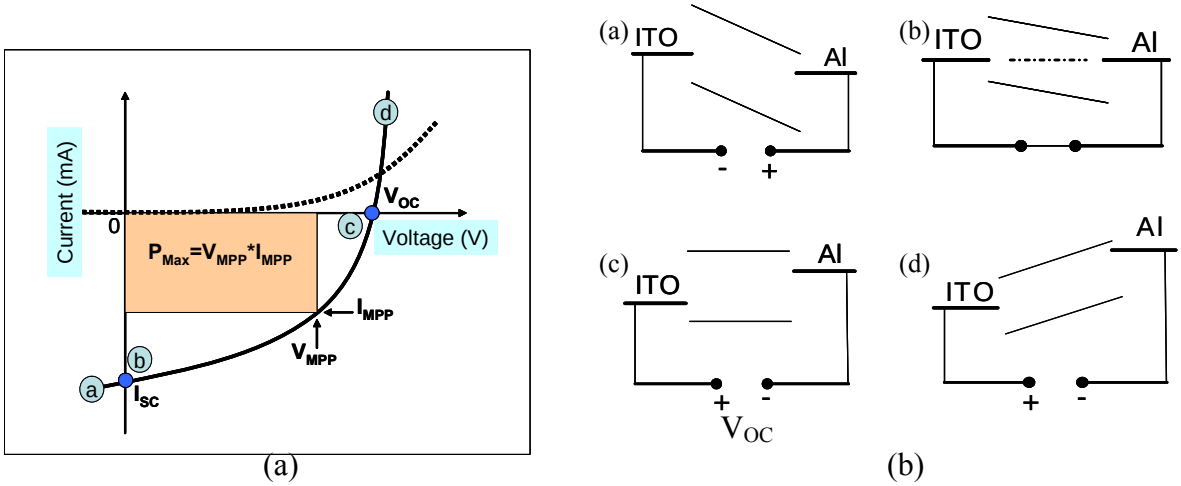

Figure 2.7: (a) The I-V characteristics of a solar cell. (b) Brief energy diagrams at different conditions using a metal-insulator-metal model (MIM).

Another important parameter which characterizes a solar cell is the fill factor (FF). The FF is defined as the ratio of the maximum output power (V_{MPP} * I_{MPP}) divided by the I_{sc} and V_{oc}. Therefore, Equation 2.1 can be rewritten as

$$PCE, \eta = \frac{P_{out}}{P_{in}} = \frac{FF \times V_{OC} \times I_{SC}}{P_{in}} \tag{2.2}$$

The spectral response of a solar cell is also an important parameter to be considered for an OSC characterization. It involves illuminating the device under a

monochromatic light source. This consists of a broadband illumination from a xenon light source diffracted through a monochromator. Before the light reaches the monochromator, it is dispersed via a chopper. The photocurrent is measured as a function of wavelength and then compared to the incident light intensity or incident photon flux. This parameter is called EQE, also known as IPCE. It is given by the number of electrons generated per incident photon (Equation 2.3):

$$EQE = \frac{\eta_e}{\eta_{ph}} = \frac{I_{sc} hc}{P_0 \lambda e} \tag{2.3}$$

where P_0 is the incident optical power, h is Planck's constant, c is the speed of light, λ is the wavelength of light, and e is the electrical charge. This generally follows the absorption spectrum of the materials constituting the OSCs. In the following section, the deposition techniques for organic semiconductor materials will be discussed.

2.3 Deposition of Organic Semiconductor Materials

Organic materials processing techniques are seen to be important because it will affect the morphology of the active layer. There are two commonly used techniques to process organic materials, i.e. wet processing and dry processing. Wet-processed methods include inkjet printing, screen printing, doctor blading, dip coating, spin casting etc, whereas for dry processing, it mainly refers to the thermal evaporation or sublimation. Small molecule organic semiconductor materials are less soluble than polymers. They can be normally sublimed in a vacuum chamber. The solubility of the small molecule material can be improved using side-chain-solubilization, e.g., PCBM.

The solubility of PCBM is improved by attaching the solubilizing groups on the bulky ball C_{60}. Some short chain polymers or oligomers may also be evaporated to fabricate efficient OSCs [49, 50]. On the other hand, conjugated polymers will decompose under extreme heat and their large molar mass mean that they are unsuitable for evaporation. However, the solubility of these materials is generally good, which allows them to be processed in solution form.

2.3.1 Dry Processing (Thermal Evaporation)

The dry processing technique refers to thermal evaporation or sublimation. In order to form a film by thermal evaporation or sublimation, a vacuum of less than 10^{-5} mbar is usually required. This will ensure that the mean free path of the evaporated/sublimed molecule is longer than the distance between the evaporation/sublimation source and the sample holder. In addition, contaminants such as O_2 and H_2O can be effectively eliminated by applying an ultra high vacuum. It can also be done by setting up an evaporator inside a glove box with an inert N_2 environment. This aside, co-evaporation can be done to create an interpenetrating donor-acceptor network or to achieve molecular doping for efficient device performances. One drawback of dry processing is that the size of the device is limited by the vacuum chamber. Hence this affects the potential of production upscaling.

2.3.2 Wet Processing (Solution Processing)

Wet processing technique refers to dissolving organic semiconducting materials in an appropriate solvent such as water or any other polar or non-polar organic solvents. Solution-proceed technology is generally more preferable compared to vacuum

evaporation/sublimation. This is due to the potential of production upscaling and low energy consumption during the production of OSCs. It is not feasible if the energy output generated by an OSC within its lifetime is less than the energy input that has been consumed to produce it. The most effective wet processing technique, which consistently gives high PCEs, is to spin coat a blend of a donor and an acceptor in a selected organic solvent (eg. blend P3HT and PCBM in chlorobenzene, PCE~5%) [26]. A device with bulk heterojunction architecture is formed this way. In this thesis, the preparation of bulk heterojunctions is mainly prepared using the spin-coating method.

2.4 Device Architectures

2.4.1 Bilayer Organic Solar Cells

Generally, there are two types of cell architectures that show promising device performances, namely, bilayer and bulkheterojunction systems. In a bilayer heterojunction device, the donor and acceptor layers can be prepared sequentially by thermal evaporation / sublimation [25, 51-53], or by solution casting one material followed by evaporation / sublimation of another material [54-56], or by sequential solution casting using a polymer precursor route [57]. Such device configuration has been demonstrated by many groups using different material combinations [58, 59]. Power conversion efficiency of about 4.2% under AM 1.5 illumination was reported for OSCs with a thermally sublimed bilayer device using CuPc and C_{60} [60].

The advantage of bilayer OSCs is the monomolecular transport of the charge carriers after the dissociation of the excitons. The holes can travel in the donor material unimpeded whereas the electrons are able to move in the acceptor material unobstructed. Hence, the opposite migration of the charge carriers will prevent the holes and electrons from recombining.

However the thickness of the active layer in a bilayer OSC cannot be too thick due to the nature of the short exciton diffusion length (10-20nm) in organic materials. The excitons can decay before they reach the donor-acceptor heterojunction interface, leading to low PCE values. A thick organic film will also cause an optical filter for the incident light before it reaches the heterojunction, resulting in a limited amount of photogenerated current. Lastly, due to the interference effect in a multiple thin film system, the active layer has to be optimized in order to locate the heterojunction interface at the position where the maximum incident light is. Figure 2.8 shows the schematic diagram of a P3HT and C_{60} bilayer heterojunction PV device.

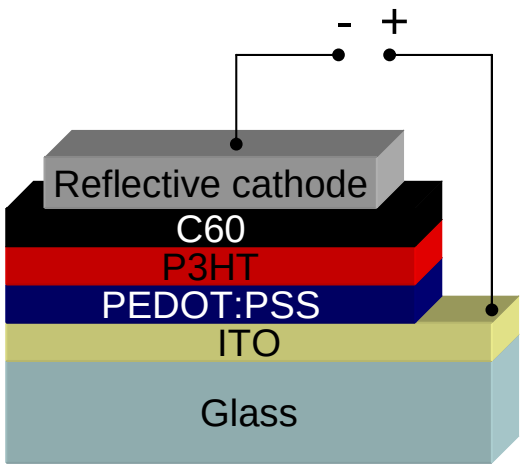

Figure 2.8: Bilayer heterojunction configuration in OSCs.

2.4.2 Bulk Heterojunction Organic Solar Cells

In a bulk heterojunction device, the donor and acceptor are blended together in a bulk volume. By proper device processing control, the blend exhibits a donor-acceptor phase separation within a 10nm-20nm length scale. In this nanoscale interpenetrating network, each donor-acceptor interface is less than the exciton diffusion length. Hence, the excitons are efficiently dissociated at the interface within its lifetime, resulting in an improved PCE.

The main advantage of the bulk heterojunction concept is that it exhibits a large interfacial area where exciton dissociation can occur. The excitons are assumed to be 100% dissociated within their lifetime, hence, the recombination is reduced to a great extent and this leads to higher photocurrent density. However, the bulk heterojunction requires percolation pathways for the holes and electrons to be collected at the respective electrodes. In other words, the donor and acceptor phases have to form a bicontinuous and interpenetrating network. Therefore, a bulk heterojunction is more sensitive to the nanoscale morphology than a bilayer, which can normally be controlled by proper thermal annealing. A bulk heterojunction of P3HT and PCBM gives the highest reported PCE (5-6%) so far [26, 27]. In this thesis, the solution-proceed PSCs were fabricated based on this configuration. Figure 2.9 shows the schematic diagram of the bulk heterojunction PSC.

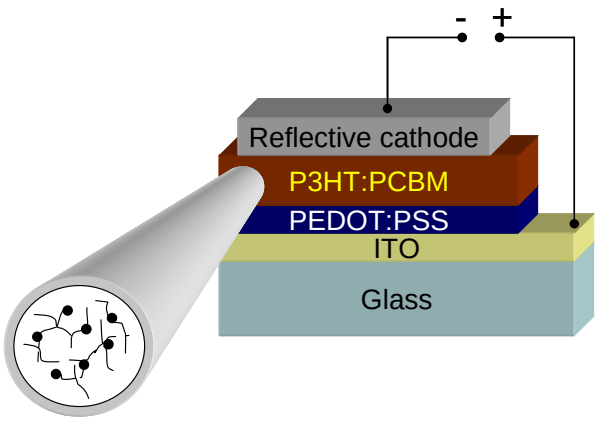

Figure 2.9: Bulk heterojunction configuration in PSCs.

2.4.3 Translucent Organic Solar Cells

A typical conventional OSC consists of a front transparent anode, a stack of photoactive organic layers or blends material that absorbs photons and converts them into electrons and holes, and a reflective cathode. When a thin metal layer or translucent cathode is used to replace the opaque cathode, the cell becomes semitransparent. A schematic drawing of a translucent OSC is shown in Figure 2.10. A variety of translucent cathode structures have been developed for top emitting or stacked OLEDs [61, 62], inverted [63, 64] tandem [65-68] and translucent OCSs [69-71].

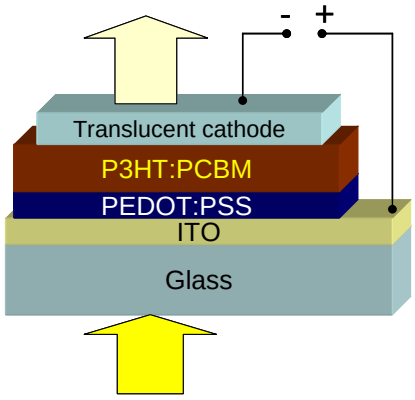

Figure 2.10: Schematic diagram of translucent OSC.

In recent years, several research groups have demonstrated the performance of translucent small molecule or PSC with different cathodes. For instance, Gadisa *et al.* reported a translucent OSC by adopting a transparent polymer cathode. The PCE is not satisfactory due to the poor conductivity of the vapour phase polymerization of PEDOT (VPP-PEDOT) [70]. Shrotriya *et al.* reported the performance of the tandem OSCs processed using a variety of translucent cathodes [67]. The results show that a semitransparent cathode of LiF/Al/Au showed the highest transparency. The reason is that the evaporated Au film on top of LiF/Al formed a rather flat and continuous film avoiding the voids and thus reduced the scattering sites for light wave. However, an ultra-thin metallic layer usually exhibits poor lateral conductivity resulting in a high series resistance and reduces the PCE of an OSC. Improving the cathode conductivity can be done by simply increasing the thickness of the metal layer, but the transparency of the cell will be suppressed.

In general, devices such as translucent OSCs, ultrathin metal films are typically used as transparent cathodes. However, the ultrathin metal cathodes, e.g. Mg:Ag, LiF/Al, LiF/Al/Ag, Ca/Ag etc, also exhibit low resistance to moisture and oxygen resulting in a short device lifetime. The ultrathin metal cathode typically generates a relatively high internal reflection at the electrode/air interface due to the mismatch of its refractive index compared to the air. In addition, ultrathin metal cathode usually has a high absorption in the visible light wavelength region leading to a low device transmittance. Therefore, the technology of high performance TCO based transparent is long sought for organic electronics including OSCs.

Slazman *et al.* reported a OSC based on small molecules with a translucent cathode structure of thin Ag/ITO [69]. The results showed that an average transmission of 26% and a maximum PCE of 0.62% were achieved. The transparency of the cell can be increased by simply reducing the thickness of Ag, but this will reduce the PCE at the same time. However, the overall poor efficiency obtained is mainly due to the limited light absorption and charge separation sites of a D/A bilayer system, comprising of CuPc and PTCBI. Kawano *et al.* also illustrated a tandem OSC with ITO as the separation layer [71]. The bottom cell showed a relatively low V_{oc} as compared to the top cell although both are fabricated with the same conjugated polymer system. This is due to the formation of a non-ohmic contact between the acceptor and the ITO.

Thin films of TCOs have many applications due to their properties of e.g. good electric conductivity and high optical transparency in the visible light wavelength range. Doped oxide materials, e.g. ZnO, SnO_2 and In_2O_3, are typically used individually, in separate layers or as mixtures such as ITO and IZO for making TCO thin films. From the plurality of TCO thin films, ITO, AZO and FTO are more commonly used TCO materials. TCO is typically used as an integral part of device applications, such as anti-static coatings, heat mirrors, solar cells, flat panel displays, sensors, and OLEDs etc.

ITO-based cathode also encounters a number of problems. For fabricating high conductivity and transparent ITO films on glass substrates, a process temperature of more than 200ºC is typically required for achieving high quality ITO. It has been

recognized that ITO films formed at process temperatures below 100ºC typically have relatively higher resistivity and lower optical transparency than TCO films prepared at a substrate temperature of more than 200ºC. Typically, ITO-based transparent electrode is deposited on active materials/layers that may not be compatible with a high process temperature. For example, ITO films made by DC/RF magnetron sputtering typically require heating substrates at elevated temperatures during film preparation or an additional post annealing treatment at a temperature above 200ºC. One problem is that high process temperatures are unsuitable for applications in organic electronics. For example, translucent and tandem OSCs are not compatible with a high temperature ITO deposition process.

When an ultra-thin metallic translucent cathode is used for OSCs, an index matching layer is typically required to improve the current spreading and light coupling efficiency to boost the light absorption in OSCs, e.g., ultra-thin metal/ITO. From process point of view, high performance ITO with deposition-rate at low process temperatures with no or little damage to the underlying functional materials is desired. The transparent electrode is required to have properties of high optical transparency, high electrical conductivity, smooth surface morphology and high stability. Also, it has to be a scalable process for mass production at low-cost.

Another challenge with ITO-based cathode is its relatively low deposition rates. G. Gu et al. have reported a RF-sputtered ITO cathode using combination gas Ar and O_2 with the growth rate of the cathode was below 1.0 nm/min [72]. It was found that the developed ITO-based cathode form at low temperature exhibits a relatively

high sheet resistance. A combination of metal/ITO structure is used to improve its lateral conductivity. The improvement in the electrical conductivity can lead to decrease in optical transparency and a possible increment in cost.

An attempt to develop an organic-buffer layer/ITO cathode was also reported [104-106]. However, fabrication of an organic-buffer layer/TCO cathode may give rise to a number of problems including the following. As an organic buffer layer is required, the fabrication process can be quite challenge. Due to the high requirement of electrical, optical and surface electronics properties, there is a limited set of materials that are suited for application in organic/ITO cathode. The organic-buffer layer/ITO cathode usually has a relatively high contact resistance causing an imperfection of the carrier collection/injection property at organic/cathode interface.

Therefore, in view of the above, there exists a need for forming high conductivity, high transparency, high deposition rate and low deposition damage ITO-based thin film for a translucent OSC. In this thesis, low temperature ITO-based cathode was developed for application in translucent and tandem PSCs. The results are discussed in Chapter 5.

2.4.4 Tandem Organic Solar Cells

As discussed in section 1.3, one of the limitations for achieving high PCE in OSC is the inefficient utilization of the solar spectrum due to a relative high bandgap in small molecules and semiconducting polymers resulting in a limited overlap of their absorption spectrum with the solar spectrum. One of the possible solutions to

overcome this limitation is to use tandem cell architecture, stacking the sub-cells different absorption properties thereby to broaden the spectral response for efficient energy conversion.

Usually, the sub-cells in tandem OSCs are connected by a composite middle electrode. The middle electrode serves two different purposes. Firstly, it creates a charge recombination site for electrons and holes generated from the bottom and top cells. Hence, this middle electrode is often called RZ. Secondly, it serves as a passivation layer to protect the bottom cell during the subsequent device fabrication. As the subcells are coupled together in series, the total V_{oc} of the tandem cell equals to the sum of the V_{oc} of individual sub-cell. This creates another advantage for tandem cell as much higher V_{oc} can be expected in a tandem OSC. In order to efficiently collect the electrons from the bottom cell and the holes from the top cell, RZ should form an ohmic contact for two adjacent subcells, meaning one side of the RZ should have low work function to align with the LUMO level of the acceptor from the bottom cell, while the opposite side of RZ should maintain high work function to align with the HOMO level of donor from the top cell. The RZ with high optical transparency and good electric conductivity is desired for tandem OSC. A schematic drawing of a tandem OSC is shown in Figure 2.11.

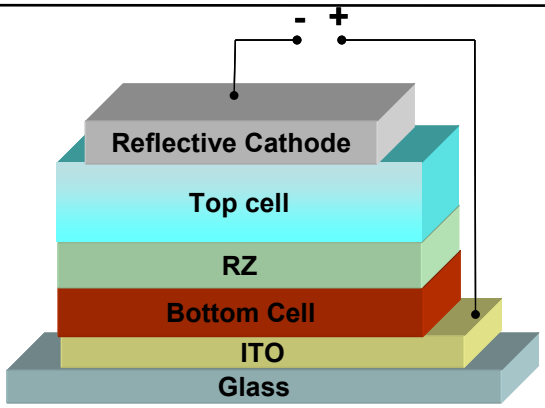

Figure 2.11: Schematic diagram of a tandem OSC.

A PCE of 6.5% for all-solution processing tandem OSC was reported by Kim et al. recently. In this report, the bottom cell had a layer structure of PCPDTBT and C_{61}-(PCBM), while the top cell was based on P3HT and C_{71}-PCBM and a thin TiOx layer was used as the RZ. [73]. The absorption bands for these two systems complement each other. The bottom subcell is protected by TiOx which is transparent in the visible region, during the formation of top subcell. A V_{oc} of 1.24 V is achieved which equals to the sum of the individual subcell. Tandem OSCs with different device structures have been proposed using:

1. Tandem OSC using small molecule subcells [52, 74, 75],
2. Hybrid tandem OSC with a combination of polymeric and small molecule subcells [66],
3. All solution processing tandem OSCs [67, 71, 76].

In this work, high performance ITO-based interlayer was applied as RZ for solution-processed tandem solar cells, using two P3HT:PCBM based sub-cells. The aim of this work was to demonstrate the suitability of low process temperature ITO-RZ for for application in translucent and tandem OSCs.

Chapter 3

Experimental

3.1 Materials Preparation

The functional polymeric semiconducting P3HT and PCBM were used for fabrication of OSCs in this work. P3HT was purchased from Sigma Aldrich, which has an average M_w of 87,000. PCBM is supplied by American Dye Source (ADS), with a purity of more than 99.95%. Prior to the deposition of the polymer blend of P3HT:PCBM, a layer of PEDOT:PSS (Baytron P VP Al4083) was coated on ITO using spin coating method. The presence of PEDOT:PSS on ITO favours the energy alignment between the work function of the ITO and the HOMO of P3HT to facilitate better hole collection. A thin layer of PEDOT:PSS also helps to planarize the ITO surface for improving the adhesion of the subsequent polymer blend layer on the substrate. PEDOT:PSS was purchased from Bayer and its molecular structure is shown in Figure 3.1. PEDOT:PSS is a polymer mixture of two ionomers. One component in this mixture is made up of sodium polystyrene sulfonate which is a sulfonated polystyrene. Part of the sulfonyl groups is deprotonated and they each carry a negative charge. The other component, poly(3,4-ethylenedioxythiophene) or PEDOT, is a conjugated polymer and carries positive charges. It is based on polythiophene together with the charged macromolecules form a macromolecular salt. ITO glass substrates were purchased from Merck Display Technologies (MDT) with an average sheet resistance of approximately 10 Ω/□. The cathode materials, such as Ca, Ag and Al, were purchased from Sigma Aldrich.

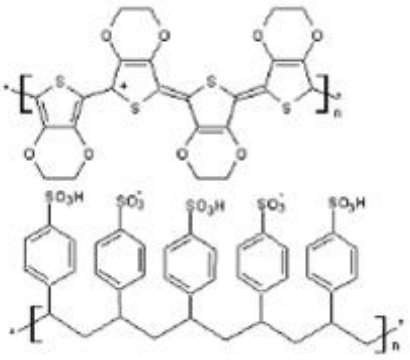

Figure 3.1: Molecular structure of PEDOT (top) and PSS (bottom).

3.2 Materials Characterization

3.2.1 Variable Angle Spectroscopic Ellipsometry

The optical response of conjugated polymers to the solar spectrum is essential to determine the feasibility of such materials in OSCs application. In this thesis, VASE was used to determine the wavelength dependent refractive index, n(λ) and extinction coefficient, k(λ) of P3HT:PCBM film. VASE is a very sensitive measurement technique that uses polarized light to characterize thin films, surfaces and material microstructures. It measures the change in the polarization state of light reflected from or transmitted through the surface of a sample. The measured quantities are not physically significant and are only used to infer useful information about the sample under test, by fitting an optical model of the sample to the measured ellipsometrric data. Figure 3.2(a) shows a typical ellipsometry configuration, where linearly polarized light is reflected from the sample surface and the polarization change is measured to determine the sample response. The polarization change is represented by the amplitude ratio, Ψ, and the phase difference, Δ. The measured response depends on the optical properties and thicknesses of each respective material. VASE is also

used to characterize composition, crystallinity, roughness, doping concentration, and other material properties associated with a change in optical response. In this work, VASE technique was used to determine film thicknesses and optical constants such as the n(λ) and k(λ) of the thin films required for device modeling and simulation using optical admittance analysis.

Early work in ellipsometry used a single wavelength laser light source, a polarizer and a compensator that were rotated by hand to measure the ellipsometric parameters [77, 78]. The principle remains the same and spectroscopic measurements are now considered to be the most accurate method for measuring film properties. Figure 3.2(b) is a picture of a rotating compensator VASE setup used in this work. During the measurement, ellipsometric ψ and Δ data were acquired at three angles of incidence (65º, 70º and 75º) over the spectrum range of 300-1000nm in steps of 10nm. ψ is the amplitude ratio upon reflection, and Δ is the phase shift (difference). Multiple angles and wavelengths were fitted simultaneously in the optical model, i.e. Cauchy model, to obtain the optical constants and the thickness of the film. The fitting process will be discussed in Chapter 4.

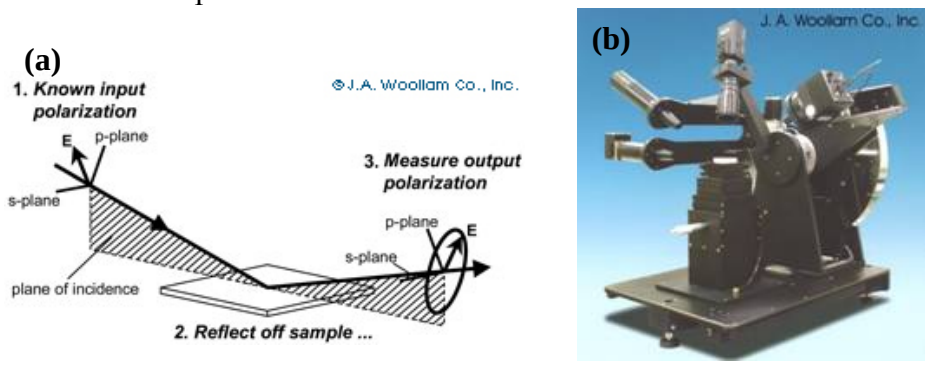

Figure 3.2: (a) An ellipsometry configuration and (b) the setup of a Variable Angle Spectroscopic Ellipsometry (VASE) used in this work

3.2.2 UV-Vis Absorption Spectroscopy

Apart from the n(λ) and k(λ) values measurements, UV-Vis spectroscopy was used to measure the absorption spectrum of P3HT:PCBM film with different weight ratios, and the blend having wt% ratio of 1:0.8 for P3HT:PCBM was found to be the optimal combination for OSCs in this work and was used for the device fabrication. UV-Vis spectroscopy measures the absorption of the sample which usually takes place through an energy transfer from the radiation field (light) to the atomic or molecular level in the spectral range from 200nm to 800nm. Figure 3.3(a) and (b) shows the schematic diagram of UV-Vis instrumental setup and the real system used in our lab respectively. According to Figure 3.3(a), the monochromatic light form in a continuous light source is obtained using a grating monochromator. The response of the P3HT:PCBM films was recorded by scanning the selected wavelength range. Experimental measurements are often recorded in term of transmittance (T), which is defined as

$$T(\lambda) = \frac{I}{I_0} \tag{3.1}$$

where I is the transmitted light intensity and I_o is the initial light intensity. It is also common to use term absorbance (A) which is related to the T as:

$$A(\lambda) = -\log\frac{I}{I_0} = -\log T \tag{3.2}$$

UV-Vis instruments usually display the data in the format of either transmittance or absorbance. Figure 3.3(c) shows the absorption spectrum of P3HT:PCBM with wt% of 1:0.8 measured using Shamadzu UV-VIS-NIR Scanning

Spectrophotometer. The peak at 332nm predominantly from the PCBM and the light absorption in P3HT is reflected with the main peak at 515nm and shoulders at 550nm and 605nm. The absorption spectrum of P3HT:PCBM thin film helps to further verify the validity of the k(λ) value obtained from VASE as k(λ) is defined as the fraction of light lost to scattering and absorption per unit distance in a participating medium. In electromagnetic terms, k(λ) can be explained as the decay, or damping of the oscillation amplitude of the incident electric field.

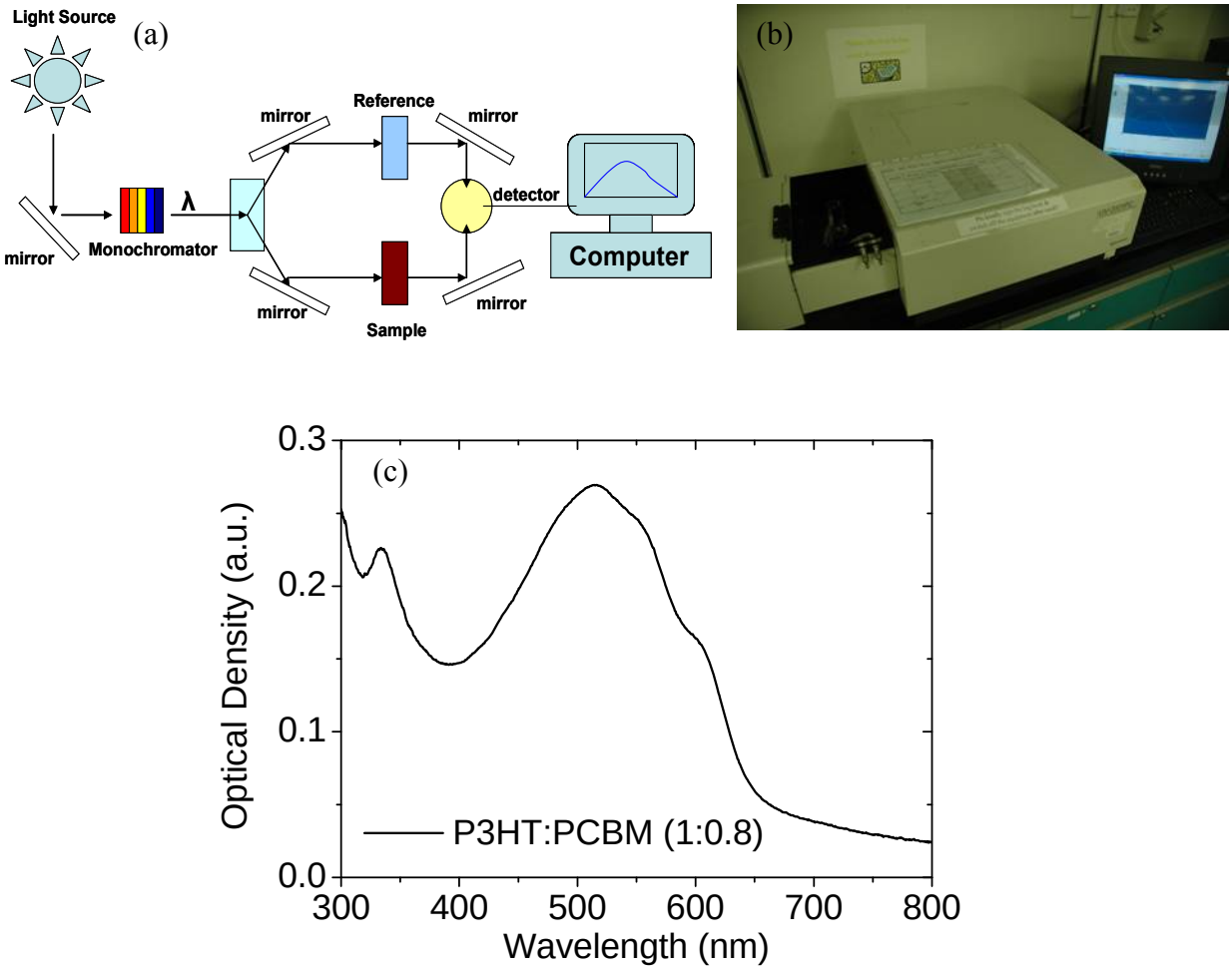

Figure 3.3: (a) Schematic diagram of UV-Vis instrumental setup, (b) Shamadzu UV-VIS-NIR Scanning Spectrophotometer used in this thesis and (c) the absorption spectrum of P3HT:PCBM thin film with a wt% of 1:0.8.

3.2.3 X-ray Photoelectron Spectroscopy

X-ray photoelectron spectroscopy, also known as Electron Spectroscopy for Chemical Analysis (ESCA), has been widely used in retrieving the chemical information of various material surfaces. This technique was developed by a Nobel Prize winner, Kai Siegbahn in 1981 (79). XPS technique is based on the photoelectric effect where the core-level electrons are emitted from a surface of a material after it is irradiated with soft X-rays (1.5 kV) in an ultra high vacuum condition. XPS spectral lines are identified by the shell from which the electron was ejected (1s, 2s, 2p, etc). The photoelectron energy has a kinetic energy, E_k:

$$E_k = h\upsilon - E_b - \Phi_{spec} \tag{3.3}$$

where E_b is the electron binding energy and Φ_{spec} is the work function of the spectrometer. XPS is a very sensitive technique to measure the chemical state and elemental composition on a surface of the sample. The detection depth normally is in the range of few nanometers. However, depth profiling of the sample is possible to achieve by scanning the sample a few times at a particular spot. Photoelectrons are collected and analyzed by the instrument to produce a spectrum of the emission intensity versus the electron binding energy. Small shifts in the elemental binding energies provide information about the chemical state of the elements on the sample surface. Ultrahigh vacuum (10^{-8} to 10^{-11} Torr) is required to remove adsorbed gases from the sample, eliminate the adsorption of contaminants on the sample, prevent arcing and high voltage breakdown and increase the mean free path for electrons, ions, and photons.

In this thesis, the XPS experiments were performed using a VG ESCALAB 220i-XL instrument equipped with a monochromatic Al Kα X-ray source with photon energy of 1486.7 eV and an unmonochromated Mg Kα X-ray source having a photon energy of 1253.6 eV, a concentric hemispherical analyzer and a magnetic immersion lens (XL lens) to increase the sensitivity of the measurement. The background pressure in the XPS chamber was below 10^{-10} mbar range during XPS measurements. The instrument was calibrated with pure gold, silver and copper standard samples by setting the Au $4f_{7/2}$, Ag $3d_{5/2}$ and Cu $2p_{3/2}$ peaks at binding energies of 83.98±0.02 eV, 368.26±0.02 eV and 932.67±0.02 eV, respectively. All XPS spectra were recorded in the constant pass energy mode of the analyzer using a monochromatic Al Kα X-ray source. Survey spectra were recorded with a pass energy of 150 eV and a 1.0 eV step width. After a Shirley-type background subtraction, an XPS spectral deconvolution was achieved by a curve-fitting procedure based on Lorentzians broadened by a Gaussian. Component peak shape and full-width-at-half-maximum (FWHM) value for a particular peak envelope were kept the same during curve fitting. Quantification was done using relative sensitivity factors (RSFs) for the XPS instrument, which takes into consideration both the corresponding photoionization cross-sections of Scofield and the transmission function of the spectrometer. The XPS is used to investigate the chemical state of cathode in the polymer/cathode interface for a translucent OSC developed in this work. The XPS analyses were correlated with the performance of OSCs and the results and the discussion are presented in Chapter 6. Figure 3.4 is a photo picture of IMRE XPS system used in this work.

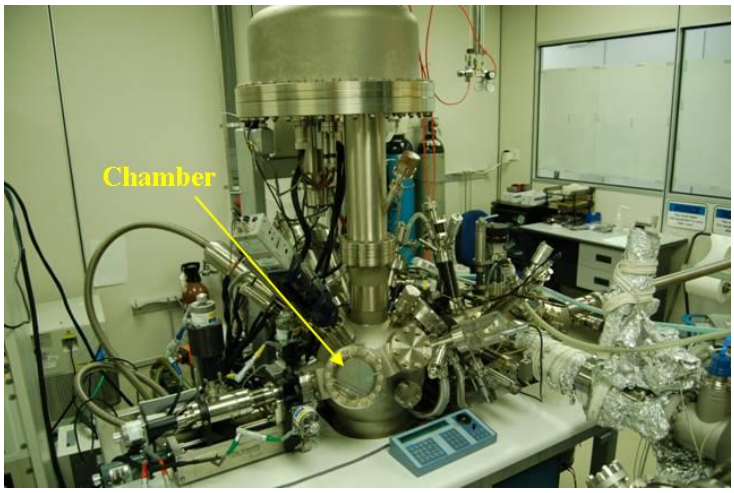

Figure 3.4: A photo picture of IMRE XPS system used in this work.

3.2.4 Atomic Force Microscopy

The surface morphology of the polymer layers was analyzed using AFM with a typical scanning area of 1.0 μm × 1.0 μm. The probe consisted of a tip on the end of a cantilever which bends in response to the force between the tip and the sample. The AFM used in this work was DI Nanoscope-IV Multimode AFM as shown in Figure 3.5. AFM tapping Mode was used to scan the surface morphology of P3HT:PCBM samples. AFM measurements were conducted in ambient evironment. The cantilever is oscillated at its resonant frequency (often hundreds of kilohertz) and was positioned above the surface so that it only tapped the surface for a very small fraction of its oscillation period. This mode was still contact with the sample in the sense defined earlier, but only for very short time during the cantilever oscillation. This is especially important when a polymer film is scanned which usually behaves soft and poorly immobalised. The results were analyzed by software called NanoScope V530r3 providing the information of surface roughness, grain size and etc.

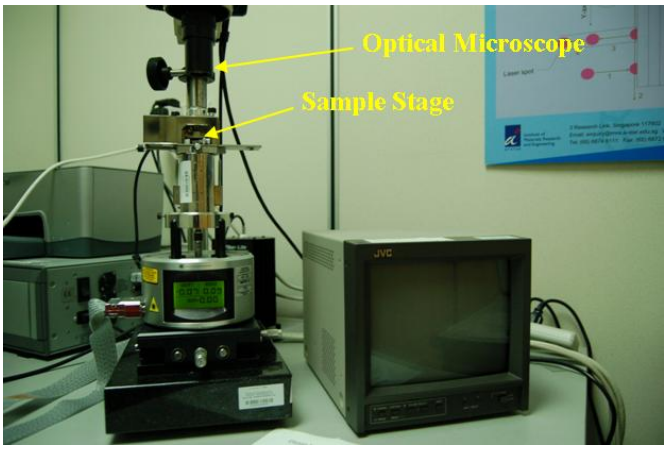

Figure 3.5: A picture of Atomic Force Microscope set-up used in this work.

3.2.5 Photoinduced Charge Extraction by Linearly Increasing Voltage

The PhotoCELIV set-up, as shown in Figure 3.6 was composed of a pulsed N_2 laser (wavelength: 337nm, pulse width <5 ns, pulse repetition rate 1 Hz), a pulse generator (SRS-DG535), a function generator (SRS-DG345) and a digital oscilloscope (Agilent, 1GHz). The sample was encapsulated and the measurement was carried out in the ambient conditions. The sample was illuminated from the glass/ITO side of the device and the photocurrent under the influence of linearly increasing voltage pulse was monitored across a variable resistor using an oscilloscope. Upon application of a reverse bias linearly increasing voltage pulse with a voltage rise speed A=dU/dt, the typical electrical response is a rectangular-shaped current transient with a plateau value corresponding to the capacitive displacement current $j(0) = \varepsilon\varepsilon_0 A/d$, where ε is the dielectric constant of the material, ε_0 is the permittivity of free space, and d is the thickness of the dielectric. The photocharge carriers can be generated throughout the film when the sample is excited with a suitable laser pulse. The

photogenerated charge carriers can be extracted by adjusting the delay between the laser pulse and the voltage pulse. The time taken to reach the extraction current maximum (t_{max}.) and the maximum current due to photoexcitation (Δj) can be estimated from the PhotoCELIV transients. The charge mobility (μ) can be calculated using the equation (3.4) as given below;

$$\mu = \frac{2d^2}{3At^2_{\max}\left[1+0.36\frac{\Delta j}{j(0)}\right]} \qquad (3.4)$$

Equation 3.4 is corrected for the electric field re-distribution during the charge extraction process. The PhotoCELIV transients were recorded by varying the voltage rise speed (A), the sample temperature and the delay between the laser and voltage pulse in order to understand the complete transport and recombination properties in these composites.

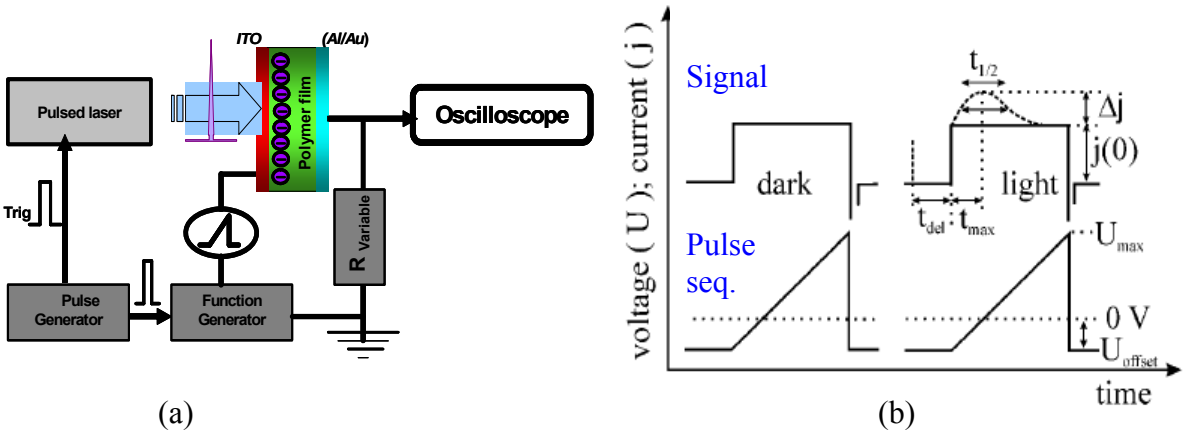

Figure 3.6 (a) A schematic drawing of the experimental arrangement of PhotoCELIV measurement and (b) the pulse sequence and schematic response of PhotoCELIV

3.3 Device Fabrication

The fabrication of bulk heterojunction OSCs in this work involved several consecutive steps. A blend of P3HT and PCBM was used as the light harvesting active layer in our P3HT:PCBM-based OSCs. P3HT and PCBM were dissolved separately in dichlorobenzene at a concentration of 20 mg/ml for P3HT and 16 mg/ml for PCBM (weight ratio = 1:0.8). After homogeneity was achieved, both solutions were mixed. 160 nm thick ITO-coated glass substrates, with an average sheet resistance of 10Ω/□, were used for the device fabrication. The ITO was patterned using standard photolithography process. After that, the ITO/glass substrates were cleaned in acetone, isopropanol and distilled water sequentially for 1 hour each. The substrates were then baked at 100^{o}C to remove any possible residual solvents. Next, the dried substrates were subjected to oxygen plasma cleaning for 10 minutes prior to spin coating a 40 nm thick PEDOT:PSS hole transporting layer. Besides removing organic contaminants, oxygen plasma treatment also helped to increase the surface work function of the ITO. Subsequently, P3HT:PCBM blends with different layer thicknesses were spun coat with a spinning speed of 1200rpm for 60 seconds in a glove box under nitrogen atmosphere. For improving the crystalinity of P3HT:PCBM film, P3HT:PCBM was annealed at 120ºC for 30 minutes. The relationship of the solution concentration to the film thickness was calibrated and the correlation between the blend thickness and the concentration of P3HT in the blend is shown in Figure 3.7(a.). Figure 3.7(b) shows the colour gradient of the resulting P3HT:PCBM film using different concentrations. Film thickness were measured using a Tencor Instruments Alphastep Semiconductor Surface Profiler. The metal cathode layer was evaporated through a shadow mask at a pressure of 8×10^{-5} Pa to obtain devices with

an active area of 9 mm^2.

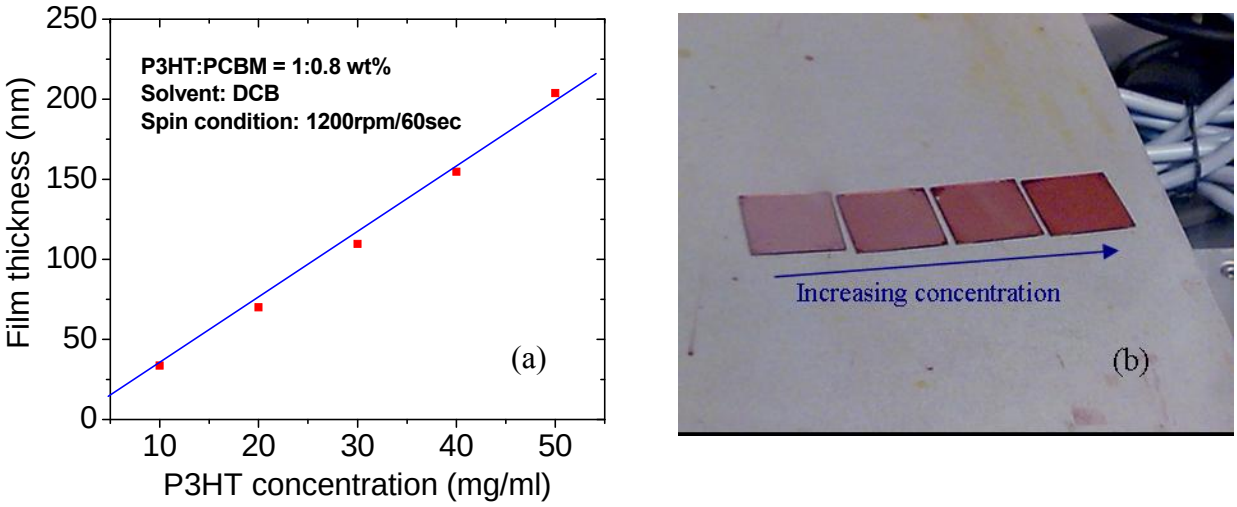

Figure 3.7: (a) P3HT:PCBM thin film thickness as a function of P3HT concentration. (b) the resulting P3HT:PCBM films right after spin coating on a glass substrate.

For a translucent OSC, a high electrical conductivity and optically transparent ITO-based cathode was prepared by magnetron sputtering, a photo picture of the sputtering chamber is shown in Figure 3.8. Sputtering is one of the most versatile techniques used for deposition of high quality ITOs for device applications. Compared to other deposition techniques, sputtering process provides the following advantages: (a) high uniformity of film thickness, (b) good film adhesion to the substrate, (c) better reproducibility of films and (d) large area deposition. Sputtering process involves the creation of gas plasma, usually an inert gas such as Ar is used, by applying voltage between a cathode and anode. The sputter target is connected to a negative voltage supply and the substrate holder forms the anode and faces the target. Sputter target is subjected to intense bombardment by accelerated ions. By momentum transfer, particles are ejected from the surface of the sputter target to form a thin film on the substrate. Sputtering is normally performed at a processing pressure of about $1x10^{-1}$

Pa. Magnetron sputtering is particularly useful when high deposition rates and low substrate temperatures are required for a specific sputtering process. In this work, a low processing temperature ITO technique was developed. The ITO thin film was prepared using an argon-hydrogen gas mixture at room temperature. As ultrathin metal interlayer of Ca, Ag or Al was introduced to improve the electron collection efficiency. The entire electrode deposition was conducted in a vacuum to eliminate possible metal oxidation from moisture and oxygen. The thickness of ITO layer was controlled by the deposition time and was optimized in order to enhance the performance of OSCs.

Figure 3.8: The magnetron sputtering chamber used in this work.

3.4 Device Characterizations

The performance of the OSCs discussed in this thesis was characterized under simulated AM1.5G solar irradiation of 100 mW/cm^2. AM1.5G solar irradiation is defined as the amount of radiation, both direct and diffused, that can be received at

any given location on Earth. The spectrum of a solar irradiation is close to that one of a black body emitter, with a temperature ~5800K. About half of the radiation is in the visible short wavelength range of the electromagnetic spectrum. The other half is mostly in the near-infrared region. A fraction of them occupies the ultraviolet part of the spectrum. Ultraviolet radiation, which is responsible for the change of color in skin pigments, is not absorbed by the atmosphere or other protective coating. A standard spectrum of AM1.5G was used in this work. AM is defined as the ratio of the mass of Earth's atmosphere through which a radiation beam will pass through as compared to the mass of Earth's atmosphere it will passes through if the sun were at its zenith (directly overhead) position. At sea level, AM = 1 when the sun is at the zenith; AM= 2 for a zenith angle, θz, of 60º. For $0 < \theta z < 70º$ AM = $1/\cos \theta z$.

The path length of the solar irradiation through the Earth's atmosphere, in units of AM, increases with the angle from the zenith. The easiest way to estimate the air mass in practice is to measure the length of the shadow, *s*, cast by a vertical structure of height, *h*, using Equation 1.1. Figure 3.9 shows the definition of AM 1, AM 1.5 and AM 2.

$$AM = \sqrt{1+\left(\frac{s}{h}\right)^2} = \frac{1}{\cos\theta_z} \tag{3.5}$$

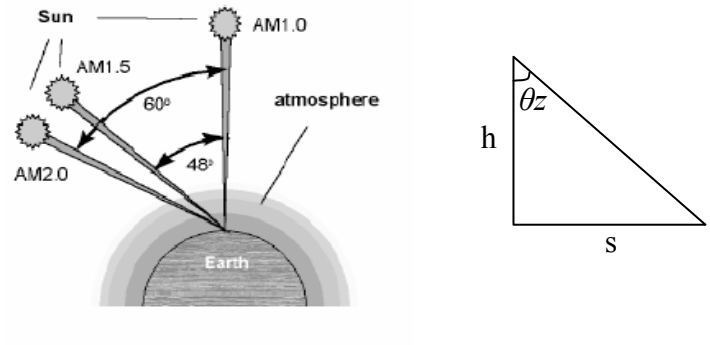

Figure 3.9: Definition of AM 1 (sun at zenith), AM 1.5 (sun at θz =48º) and AM 2 (sun at θz=60º).

AM 1 is the standard spectrum for space applications. On the other hand, a zenith angle of 48°, corresponding to AM 1.5, was chosen for the characterization of solar cells. The spectrum of the sun (Figure 3.10) follows the spectrum of a black body emitter at a temperature of 5800 K, which corresponds to the temperature of the sun's surface. Due to the absorption of light by molecules such as H_2O and CO_2 present in the atmosphere, the definition of a solar spectrum takes on a different picture. Hence, there are two distinct spectra: AM 1.5 direct and AM 1.5 global. AM 1.5 direct only takes into account the spectrum measured in the direction of the sun, whereas AM 1.5 global also takes scattered sunlight into consideration. Note that the term AM 1.5 is commonly used to refer to the solar spectrum defined by AM 1.5 global. Under these conditions, the global irradiation power incident on one square meter on the earth surface equals to 1000 W.

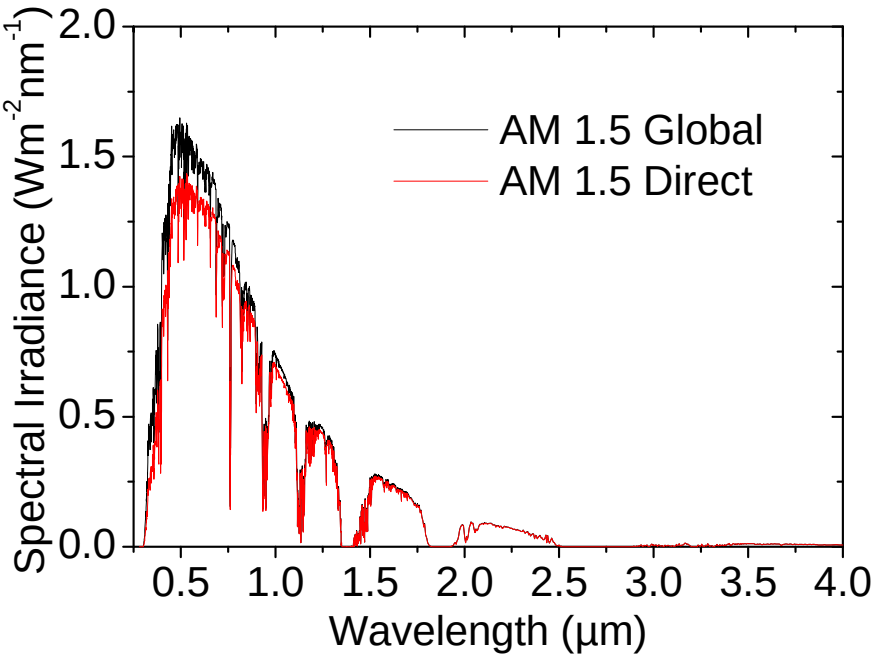

Figure 3.10: A comparison between the AM 1.5 direct and AM 1.5 global standard spectra. [80]

Most of the organic semiconductors are hole conductors and they have an optical band gap of around 2.0 eV. This is considerably higher than that of silicon (1.17 eV) and, thus, this limits the photon harvesting of the solar spectrum to a great extent. Therefore, the chemical flexibility for modifications on organic semiconductors via chemical synthesis, as well as the perspective of low cost and large-scale production drives the research in this field in academia and industries.

The measurement of current-voltage (I-V) and spectral response of OSCs is important to characterize the device performance. The I-V curve allows us to obtain the PCE, whereas for a spectral response measurement, it yields the number of collected electrons per incident photon. The latter efficiency is named EQE or IPCE.

For the I-V measurement, a schematic drawing of the setup is shown in Figure 3.11. In the system, a xenon lamp is used as the light source. The light passes through an AM1.5G optical filter, allowing the output light spectrum to match the solar spectrum closely. The measurement is usually carried out in the range of -1 to 1 volts for the P3HT:PCBM system, with an interval step of 0.05V. The OSC is illuminated under the calibrated AM1.5G solar simulator and the photocurrent generated was detected using a Keithley 2400 source-meter. The light intensity was calibrated using a solarimeter with a reference Si solar cell (certified by National Renewable Energy Lab (NREL)) and was adjusted to 100 mW/cm^2. The measurements were carried out in a nitrogen glove box system.

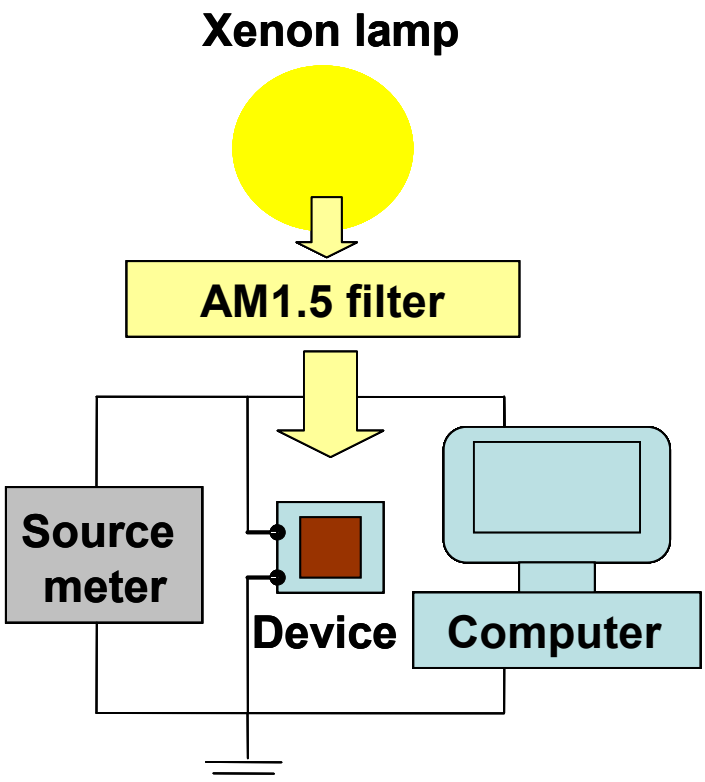

Figure 3.11: A schematic diagram of a I-V characterization measurement setup used in this work.

For an EQE measurement, it was recorded under the illumination of a monochromatized xenon lamp. The incident beam was first chopped by a mechanical chopper at a pre-determined frequency. The chopped beam was directed to a monochromator with a grating system, so that individual wavelengths was separated. Next, the monochromatized beam was guided through an optical fiber or liquid waveguide. Sample diode illumination was effected. The photogenerated current was then detected using a lock-in-amplifier. Calibration of the xenon lamp was done using a calibrated silicon photodiode prior to each device measurement. The EQE was calculated using Equation 2.3. A schematic drawing of the setup is shown in Figure 3.12.

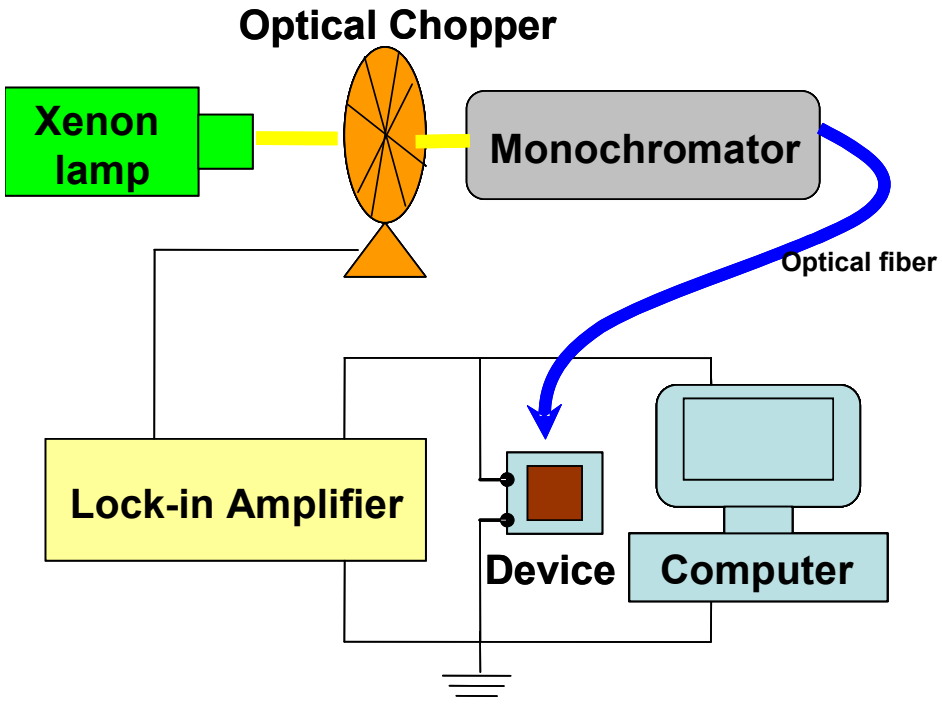

Figure 3.12: A schematic diagram of an external quantum efficiency measurement setup used in this work.

The stability of OSCs was monitored under a continuous shinning of simulated solar irradiation AM1.5. The testing cell was positioned in a sample holder as shown in Figure 3.13. The sample holder was then directed towards solar simulator and electrically connected to a high performance computer with an auto-recorded software monitoring system. The system has 24 channels and is able to measure 24 testing devices and record parameters of Jsc, Voc, FF and PCE simultaneously. Figure 3.14 shows the schematic diagram of OSCs lifetime testing system developed in our lab.

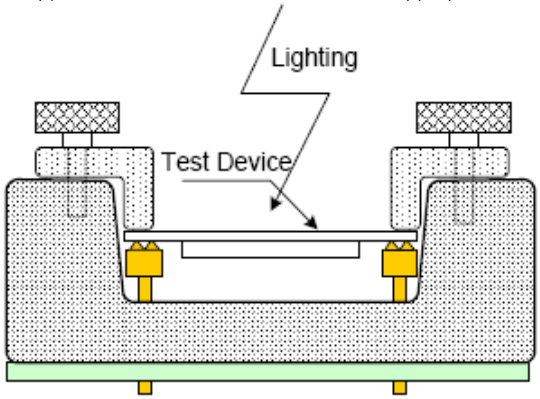

Figure 3.13: Testing device was positioned in a sample holder for lifetime measurement.

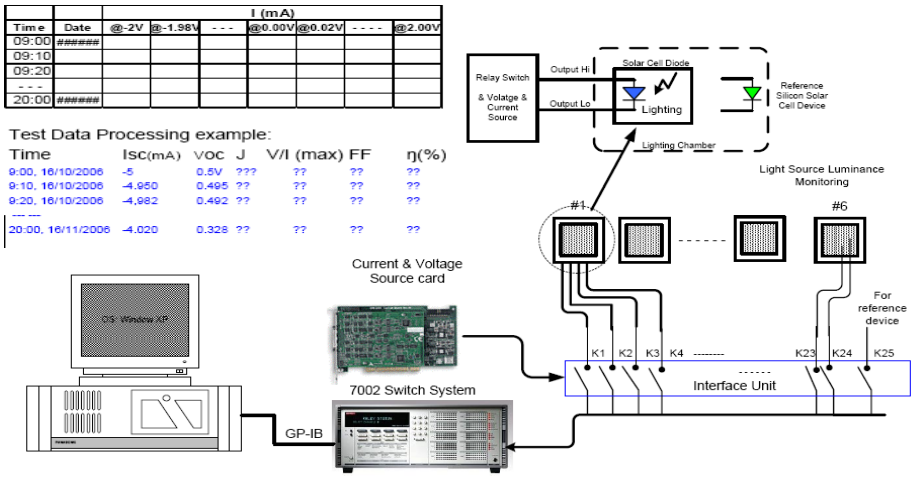

Figure 3.14: Schematic drawing of organic PV lifetime test system with the essential electronic components.

Chapter 4

Optical and Optimal Design of Organic Photovoltaics

4.1 Optical Admittance Analysis

From the optical point of view, an OSC can be considered as a multilayered thin film system composing of light absorbing and non-absorbing materials. Therefore the optical properties and optimal structure of such a multilayered device can be investigated by applying thin film optical analysis techniques. For example, if a thin film OSC has m layers, the effective optical admittance, y_{eff} , of this multilayer structure can be defined as $y_{eff} = C/B$, where B and C can be determined by solving the following matrix equation [81, 82]:

$$\begin{pmatrix} B \\ C \end{pmatrix} = \left[\prod_{j=1}^{m} \begin{pmatrix} \cos\delta_j & (i\sin\delta_j)/y_j \\ iy_j \sin\delta_j & \cos\delta_j \end{pmatrix} \right] \begin{pmatrix} I \\ y_{m+1} \end{pmatrix}, \qquad (4.1)$$

where y_j and y_{m+1} are the admittances of the jth layer and substrate respectively. I is the unit matrix, δ_j is the angular phase given by:

$$\delta_j = \frac{2\pi N_j d_j \cos\theta}{\lambda} \quad , \qquad (4.2)$$

where d_j is the actual thickness of the jth layer in this m layered structure, and Nj is the corresponding complex refractive index given by $N_j = n_j(\lambda) - ik_j(\lambda)$, where $n_j(\lambda)$ and $k_j(\lambda)$ are the real and imaginary parts of N_j, respectively. The matrix Equation (4.1)

takes into account the effect of multiple reflections in a multilayered structure. Using the value y_{eff} calculated from a m layered thin film system, the total reflectance as a function of wavelength, $R(\lambda)$, can be expressed as:

$$R(\lambda) = \left| \frac{N_0 - y_{eff}}{N_0 + y_{eff}} \right|^2 , \tag{4.3}$$

where N_0 is the refractive index of air. The reflectance thus obtained depends on the wavelength of the incident radiation. Assuming normal incidence, the total transmittance, $T(\lambda)$, of these m layers can be expressed as [81, 82]:

$$T(\lambda) = [1 - R(\lambda)] \prod_{j=1}^{m} \Psi_j , \tag{4.4}$$

where

$$\Psi_j = \frac{\mathrm{Re}(Y_{j+1})}{\mathrm{Re}(Y_j) \left| \cos\delta_j + \frac{Y_{j+1} \sin\delta_j}{N_j} \right|^2} \tag{4.5}$$

The total absorptance as a function of wavelength, the net absorptance of the jth layer, $A_j(\lambda)$, in an m layered structure can be determined by [81]:

$$A_j(\lambda) = [1 - R(\lambda)][1 - \psi_j(\lambda)] \prod_{i=1}^{j-1} \psi_i(\lambda) , \tag{4.6}$$

Using the flux of the incident solar irradiation $F(\lambda)$, measured in Wm^{-2} nm^{-1}, the integrated absorptance of any individual layer, $\bar{A}_j$, in an m-layered system can be calculated as [81, 82]:

$$\bar{A}_j = \frac{\int A_j(\lambda) F(\lambda) d\lambda}{\int F(\lambda) d\lambda} \quad , \tag{4.7}$$

Using Equations (4.6) and (4.7), it is possible to optimize the OSC structure through optimizing the light absorptance in the active region. The OSCs studied in this work have a typical structure of glass/ITO/PEDOT/P3HT:PCBM/cathode. In order to improve the OSC performance, it is necessary to optimize the layer thickness by aligning with the maximum total absorption, while keeping the active layer as thin as possible to achieve good transport properties. An OSC adopts a translucent status when the opaque metallic cathode is replaced with a translucent electrode. An optimal cell structure is then designed to sufficiently enhance the total transparency of the OSC, while maintaining the maximum light absorptance in the active P3HT:PCBM layer.

In this work, two assumptions on thin film system were made in the modeling. Firstly, the individual layer included in the organic PV thin film system is homogeneous and isotropic during deposition. Hence, the linear optical response can be described by a wavelength dependent scalar complex index of refraction. Secondly, the interfaces in the thin film system are flat and parallel compared to the wavelength of the incident light. This eliminates the consideration of light scattering effect in the interfaces of the thin film system. Before the simulation was proceeded, the information on the roughness of the polymer surface, n(λ) & k(λ) values were measured in order to perform a reasonable device simulation.

4.2 Surface Roughness of P3HT:PCBM Thin Film

Prior to the measurement of the optical constants of functional materials used in the device fabrication and also for the simulation, the surface roughness of P3HT:PCBM thin film, which is spun coat on a bare glass substrate was examined using AFM. The thin film preparation condition is already discussed in chapter 3. The film went through an annealing process of 120ºC for 30 minutes in order to increase the crystalinity. Figure 4.1 shows the height image of P3H:PCBM film with the root mean square (rms) roughness of 0.7nm (<1nm), which suggests that the assumption of smooth film surface used in the optical simulation is valid. Hence, the possible light scattering at polymer/electrode can be neglected during the optical modeling and the simulation.

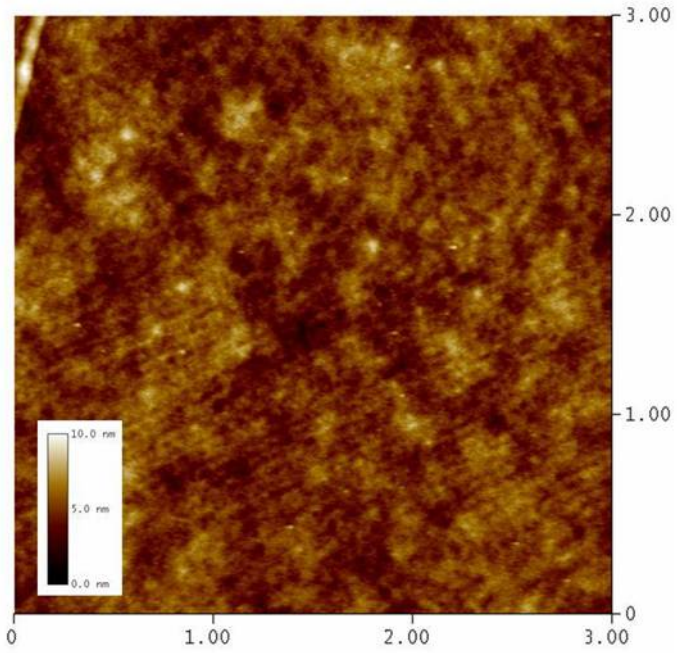

Figure 4.1: Surface morphology of P3HT:PCBM film with a surface rms roughness of 0.7nm.

4.3 Measuring the Optical Constants of Functional Layers

Initially VASE fitting process was done to obtain the optical constants of P3HT:PCBM system before performing the optical admittance analysis. In this testing sample preparation, the P3HT and PCBM blend solution was spun coat on the fused silica (glass) substrate to form a homogeneous layer with a surface roughness less than 0.7nm as shown in Figure 4.1. The flow chart in Figure 4.2 illustrated the procedure used to deduce material properties from VASE measurement. Regression analysis is required because an exact equation cannot be written. Often the answer is over-determined with hundreds of experimental data points for a few unknowns. Regression analysis allows all of the measured data to be included when determining the solution.

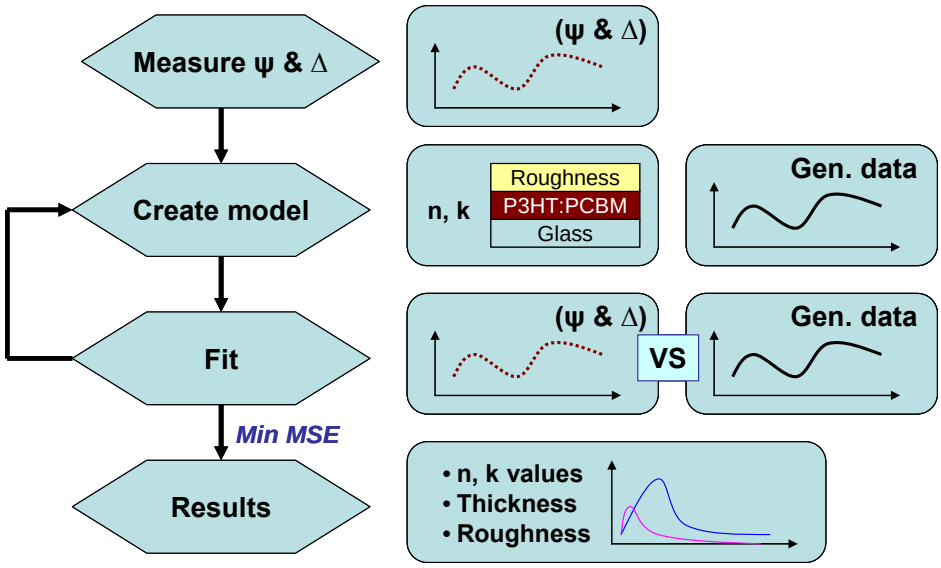

Figure 4.2: Flowchart for ellipsometry data analysis

According to Figure 4.2, the data analysis proceeds as follows: after the P3HT:PCBM sample was measured, a Cauchy model was constructed to describe

P3HT:PCBM layer. This Cauchy dispersion relation can be written as $n(\lambda)=A+B/\lambda^2+C/\lambda^4$, and k=0 at wavelength greater than 650nm for P3HT:PCBM system as the film is transparent above this region. A, B and C are the fitting parameters. The optical constants of the substrate (fused silica) were kept constant during fitting. If all the parameters are not known, an estimate is given for the purpose of the preliminary calculation. The calculated values were compared to experimental data. Any unknown material properties can then be varied to improve the match between experiment and calculation. The number of unknown properties should not exceed the amount of information contained in the experimental data. For example, a single-wavelength ellipsometer produces two data points (Ψ, Δ) which allows a maximum of two material properties to be determined. Finding the best match between the model and the experiment was typically achieved through regression. An estimator, like the Mean Squared Error (MSE), was used to quantify the difference between curves. The unknown parameters are allowed to vary until the minimum MSE is reached.

In this work, A, B and C were set to 1.7, 0.001 and 0.0001 respectively for the initial fitting parameters. A, B and C are defined as fit parameters, thereby varying the index of refraction through the Cauchy. The thickness of the Cauchy layer was estimated using surface profiler and the thickness of the film was defined as a fit parameter. To simplify the fitting process, a transparent region for P3HT:PCBM thin film was located which usually happened at a wavelength above 650nm as shown in Figure 3.3. The organic film was assumed transparent up to the longest measured wavelength, i.e. 1000nm. A point-by-point fitting is conducted to fit as much of the

measured data as possible in the transparent region which is essentially useful information for the normal fitting at a later step.

A normal fit was performed in the transparent region and yielded an MSE of around 3, obtaining a good fit to the experimental data in the wavelength greater than 650nm. The film optical constants over the measured wavelength range of 300-1000nm were determined. The fitting parameters were switched to n(λ) and k(λ). By performing a point-by-point fit starting from the long wavelength end, the resulting Ψ and Δ fit was shown in Figure 4.3(a) and (b) respectively. Generally the fitting between the experimental data and generated data were quite good, only a small portion of the curve was out of shape. The possible reason for this could be the grading effect for the polymer film which is neglected during the fitting. The Cauchy model was created with the assumption of perfect homogeneity in its depth profile. However, P3HT:PCBM might have morphology variation in z-axis in reality. The fitting was still within the satisfactory limit, and the resulting optical constants of P3HT:PCBM with wt% 1:0.8 were extracted from Cauchy model and are plotted in Figure 4.4. The values of k(λ) should have a similar curve shape with the absorption spectrum of the material, which can be used to further verify the validity of the data from the fitting process. The n(λ) and k(λ) values of ITO, PEDOT:PSS, Ca, Ag, Al used in this work were obtained from literature for simulation.

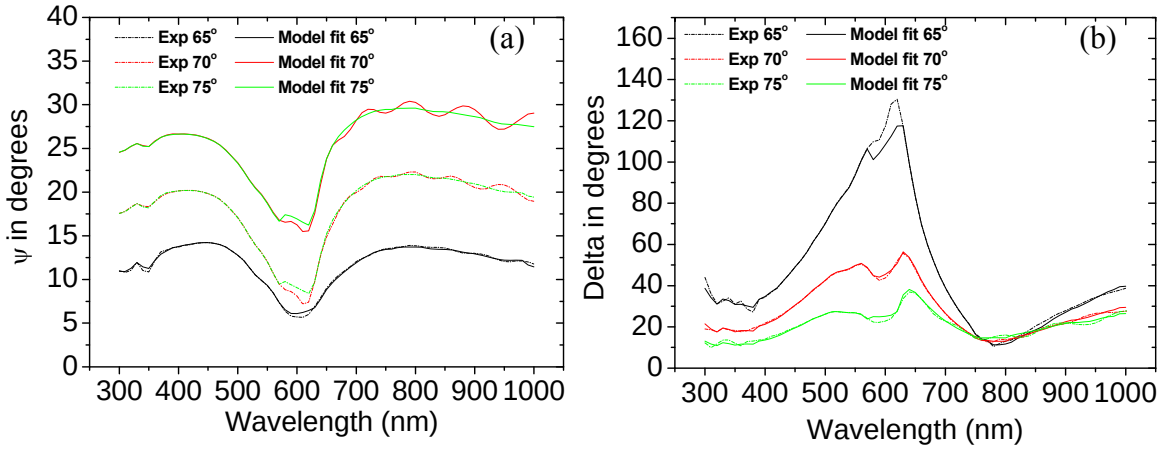

Figure 4.3: Generated and experimental (a) Ψ and (b) Δ data for P3HT:PCBM on fuse silica transparent substrate, from point-by-point fit with the film thickness fixed.

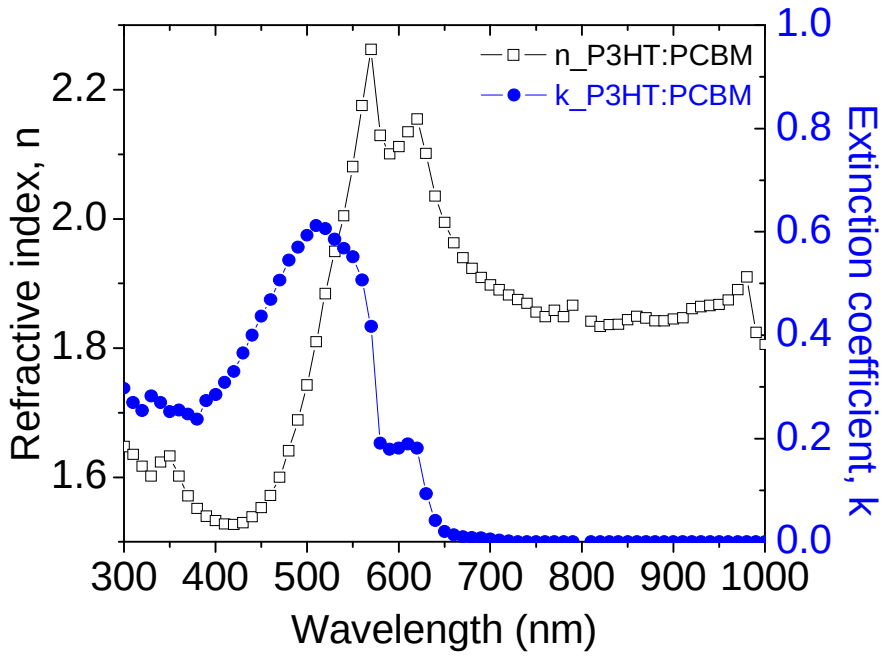

Figure 4.4: The n(λ) and k(λ). of P3HT:PCBM obtained from VASE.

4.4 Device Design and Optical Enhancement in Organic Solar Cells

The optical properties of OSCs of the type: glass/ITO/PEDOT:PSS/P3HT:PCBM(25-300nm)/Ca(10nm)/Ag(100nm) were studied using optical admittance analysis. An ultrathin layer of calcium in OSCs serves as a work function matching contact for enhancing the electron collection property. Figure 4.5 illustrated the contour map of light absorbance calculated for a set of P3HT:PCBM-based OSCs with an active layer varied over a thickness range from 0nm to 300nm. It can be seen that the light is absorbed mainly by the P3HT:PCBM blend layer and light absorption in PEDOT layer does not play a critical role in the glass/ITO/PEDOT/P3HT:PCBM/Ca/Ag structure. The results show that the device possessed maximum light absorption when the OSC having polymer blend at layer thickness of 75nm, 200nm and 250nm. The absorbance contour map, as shown in Figure 4.5 indicated that a thinner OSC with a 75 nm thick P3HT:PCBM layer adsorbs more light at short wavelength range and a thicker OSC with P3HT:PCBM over the thickness range from 200nm to 250 nm adsorbs more light in the entire visible light region. However, the polymer thickness in the range of 100 nm to 150nm showed relatively less absorbance in the entire absorbance contour. The correlation between the integrated absorptance and polymer blend over the P3HT:PCBM layer thickness range from 25nm to 300 nm for opaque OSCs was calculated using Equation 4.7 and shown in Figure 4.6. The results show clearly that the light absorption in P3HT:PCBM-based OSCs has an oscillation behaviour in relation to the P3HT:PCBM layer thickness. The relative absorption peaks are located at the P3HT:PCBM layer thickness of 75 nm and 200 nm respectively. The calculation agrees with the reported results in showing that a 200 nm thick active layer was suitable for P3HT:PCBM based OSCs [83], which exhibited

good absorption .

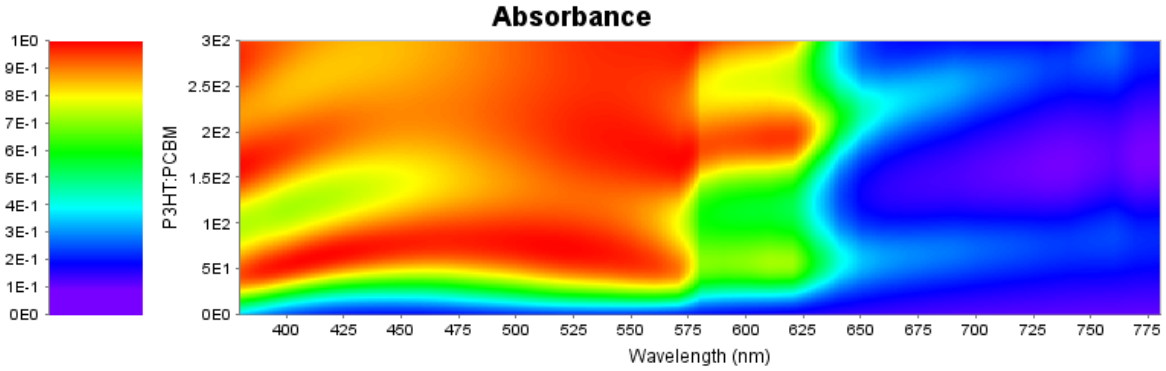

Figure 4.5: The contour map of light absorbance calculated for OSCs having a configuration of glass/ITO/PEDOT/P3HT:PCBM/Ca/Ag.

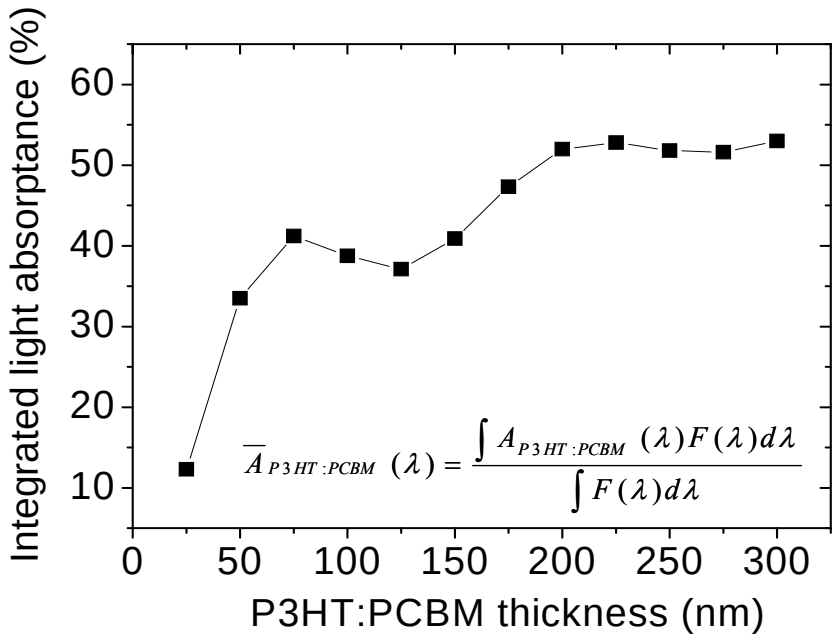

Figure 4.6: Calculated integrated absorptance as a function of the P3HT:PCBM layer thickness for PSCs of type ITO/PEDOT:PSS(40nm)/P3HT:PCBM(25-300nm)/Ca(10nm) /Ag(100nm).

To understand this further, the optical electric field or optical density, $|E|^2$ in OSCs with two different active layer thickness, 75nm and 125nm at λ=500nm was

calculated as shown in Figure 4.7. Since the optical electric field energy absorbed (number of photons absorbed), $Q_j(x)$, is proportional to the product of the refractive index, extinction coefficient and the square of the optical electric field, $|E|^2$ with the following relationship:,

$$Q_j(x) = \frac{2\pi c \varepsilon_0 k_j n_j}{\lambda} \left| E_j(x) \right|^2 \tag{4.8}$$

where c is the speed of light, ε_0 is the permittivity of free space, the penetration profiles of $Q_j(x)$ and $|E|^2$ are assumed to be identical. For thin film system, there are many interfaces involved. These interfaces normally generate large reflection due to the difference in the refractive index with the adjacent layers. The distribution of the optical electric field inside the thin film system will be affected especially a highly reflective metal electrode is used in PV devices. This phenomenon is called interference effect, which usually dominates the light distribution in a multilayer thin film system.

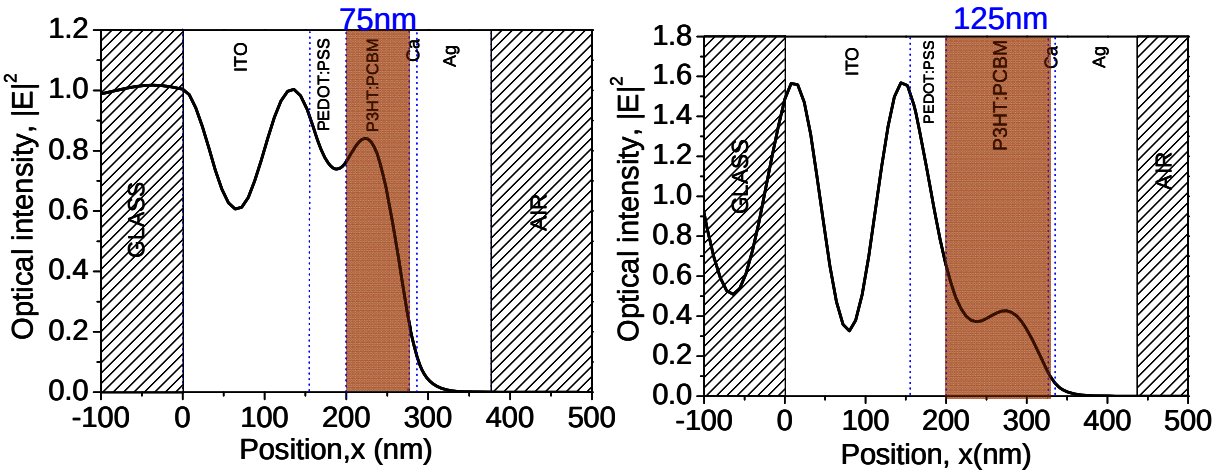

Figure 4.7: The optical electric field distribution in PSC (a) 75nm and (b) 125nm of P3HT:PCBM layer in the structure: glass/ITO/PEDOT:PSS/P3HT:PCBM/Ca/Ag at λ=500nm.

As can be seen, the peak position of optical electric field in 75nm of P3HT:PCBM is higher than the one with 125nm P3HT:PCBM. Both cases experience second light absorption after the light reflected back to the system at the polymer/metal interface, but the amount is different. The reflected light might cause a destructive interference effect with the next incident light when 125nm P3HT:PCBM is used.

To further verify the validity of Figure 4.7, we fabricated three structurally identical OSCs with different P3HT:PCBM layer thickness. The preparation condition was already described in section 3.2 and the concentration used to achieve these three thicknesses can be referred to Figure 3.7. The reference devices with the configuration: glass/ITO/PEDOT:PSS/P3HT:PCBM(75, 125 and 200nm)/Ca(10nm)/ Ag(100nm) are fabricated based on the results obtained from simulation as shown in Figure 4.6. The active layer thickness of 75nm, 125nm and 200nm were chosen because they showed the local minimum and maximum of the integrated absorptance of active layer. The active layer thickness, greater than 200nm, was expected to achieve higher integrated absorptance which will lead to a higher photogenerated current theoretically, but the fill factor remains an issue due to the difficulty of the charge carriers to be transported to the respective electrodes in such a thick active layer as compared to 75nm. Figure 4.8(a) and (b) show the spectral response and J-V characteristics of the organic PV references devices with 75nm, 125nm and 200nm of P3HT:PCBM blend layer thickness. The important PV parameters have been extracted and summarized in Table 4.1.

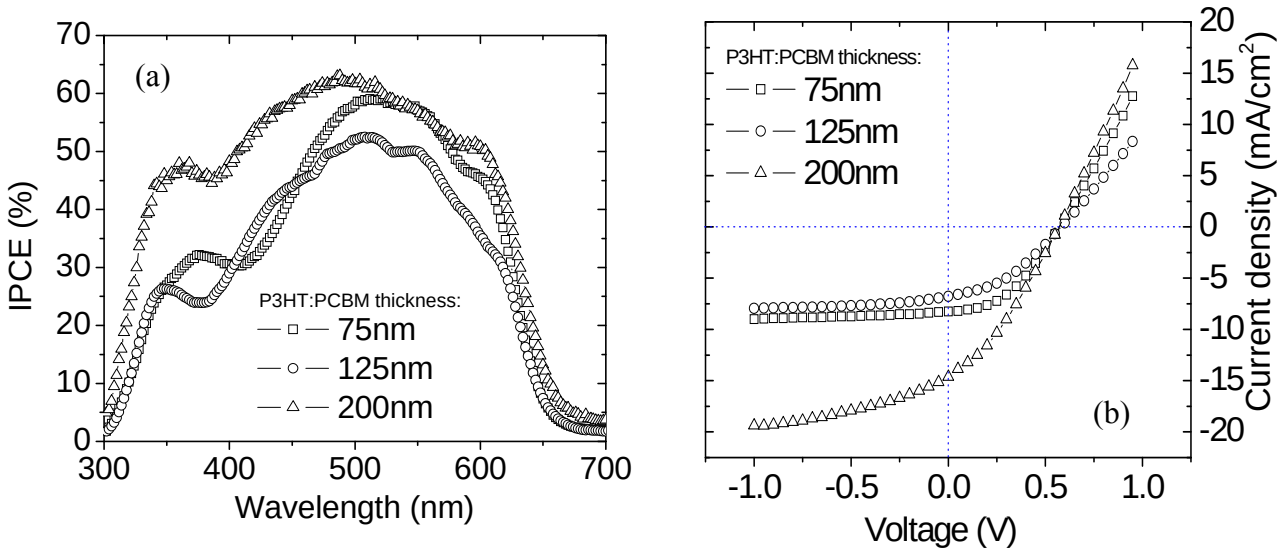

Figure 4.8: A comparison of the IPCE spectral (a) and I–V characteristics (b) measured for a control PSC with the active layer thickness of 75nm, 125nm and 200nm.

According to Table 4.1, the reference OSC with the thicker active layer, 200nm in this case, exhibits Jsc of 14.77mA/cm^2. This is higher than the one with 125nm and 75nm of P3HT:PCBM blend layer thickness. This experimental result is reasonable based on the simulations in Figure 4.6 which proved that 200nm of P3HT:PCBM layer thickness tends to absorb more incident light (53%) than the one with 75nm and 125nm. However, the device with 125nm P3HT:PCBM layer shows poorest performance among the three selected thicknesses due to the interference effect which was already discussed in the previous section. The experimental results generally agreed with the calculation from optical admittance analysis. This aside, OSCs with thicker P3HT:PCBM layer generally had a lower fill factor, resulting to an increased series resistance in the cell. In this work, a 75 nm thick P3HT:PCBM layer was used for translucent and tandem OSCs.

Table 4.1: A summarized photovoltaic characteristics of the reference OSCs

P3HT:PCBM thickness	IPCE (%)	V_{oc} (V)	J sc (mA/cm^2)	FF (%)	PCE (%)
75 nm	59.00	0.57	8.22	43	2.02
125nm	52.70	0.58	6.73	39	1.52
200 nm	63.11	0.57	14.77	34	2.80

In general, optical admittance analysis was implemented and applied to calculate the light distribution in OSCs prior to the material process and device fabrication. The procedure was based on an optical thin film analysis which took into account the interference effects in multilayer thin film systems and enabled calculation of the optical properties of thin film OSC with a multilayer configuration. Not only it allowed to optimize the structure of such cells and utilize interference effects to maximize usage of incident solar irradiation, but also shortened the conventional device optimization process. The simulation approach was used to study the optimum device architecture for translucent and tandem OSCs.

Chapter 5

Translucent Polymeric Solar Cells

The research efforts surrounding organic small molecule and polymer based solar cells have been centered on optimizing the device structures and PCE [26, 28-30] of, OSCs with PCE = 5% under simulated AM1.5G illumination have been demonstrated using both the vacuum sublimation and the solution process approaches [26, 84, 85]. However, the limited use of the solar spectrum is still an open challenge for OSCs. One way to improve the performance of OSCs is to use tandem structures, which can be formed using a translucent cathode. Recently, the research in translucent OSCs has attracted a lot of attentions for consumer electronics, energy window and application in other architecture surfaces. This chapter discusses the improvement/enhancement of translucent OSCs over the two competing performance indexes: power conversion efficiency and transmittance, for stacking up or transparency. The high performance ITO-based cathode developed in this work can be formed at room temperature, without causing damage to the underlying functional organic layers, which is suited for application in organic electronics including translucent and tandem OSCs.

5.1 Low Processing Temperature ITO

Thin films of ITO have been widely used as transparent electrode in opto-electronic devices such as displays and solar cells because of the unique characteristics of high electrical conductivity and optical transparency over the visible light wavelength region. Generally, ITO thin films are deposited on the rigid glass substrates over a

processing temperature range of 150 – 250 ^{o}C [86-92].

The present OSC technologies are focused on rigid substrates, such as glass, but flexible devices are getting more attention nowadays due to their lightweight, low cost, and flexibility. The success of the flexible OSC will open the possibility of fabricating devices by roll to roll processing, thus providing the basis for very-low-cost mass production. However, organic PV components set the limit of the ITO processing temperature below 150 ^{o}C [86]. ITO thin films formed at a processing temperature below 200 ^{o}C usually have relatively higher resistivity and poorer optical transparency than the films prepared at a higher substrate temperature. When ITO thin film is deposited on the functional organic layer, e.g., organic PV materials, the high temperature deposition process is not compatible with OSC process. Therefore the development of high quality ITO films with smooth surfaces, low resistivity and high transmission over the visible spectrum and at a low processing temperature, is of practical importance. There remains a need for high quality ITO-based cathode that can be fabricated at a low processing temperature for application in OSCs.

In this work, a process of producing high quality ITO films at a low processing temperature was developed using magnetron sputtering process. A hydrogen-argon gas mixture was used for ITO deposition. The hydrogen partial pressure was varied to modulate and optimize the properties of the ITO films. The film properties, including electrical, optical and surface electronic properties were investigated.

5.2 Electrical and Optical Properties of ITO Thin Films

Traditional ITO thin film often requires high processing temperature of over 200ºC and is thus not suitable for application in organic electronics. A high performance ITO-based cathode is desired for application in organic electronics including organic photovoltaic cells. In ITO films, both tin dopants and ionized oxygen vacancy donors provide the charge carriers for conduction. The number of oxygen vacancies that provide a maximum of two electrons per oxygen vacancy plays a dominant role in determining the charge carrier density in an ITO film with high oxygen deficiency. It is also affected by the deposition conditions such as sputtering power, substrate temperature, Sn/In composition in target and sputtering species in the plasma during the film preparation.

In this work, the electrical properties of ITO films were optimized by varying the hydrogen partial pressure in the gas mixture. The substrate was not heated during the film deposition. The substrate temperature induced by the plasma was lower than 60°C. The sheet resistance and resistivity of ITO films on a glass substrate as a function of hydrogen partial pressure are plotted in Figure 5.1. Both the sheet resistance and resistivity decreased dramatically after introducing hydrogen into the sputtering gas mixture. When hydrogen is added in the sputtering gas mixture, the grow flux during the magnetron sputtering includes a significant amount of energetic hydrogen species with energies over the range of 10-250eV [112]. These active hydrogen species can remove weakly bound oxygen in the depositing films. As a result, the addition of hydrogen in the sputtering gas mixture shows a reducing effect on oxide and leads to an increase in the number of oxygen vacancies in the films and

hence an increase in the number of charge carriers. Because of the electrical conductivity is proportional to the product of charge carrier concentration and the mobility, the decrease of the film resistivity is mainly due to the increase of carrier concentration in ITO films.

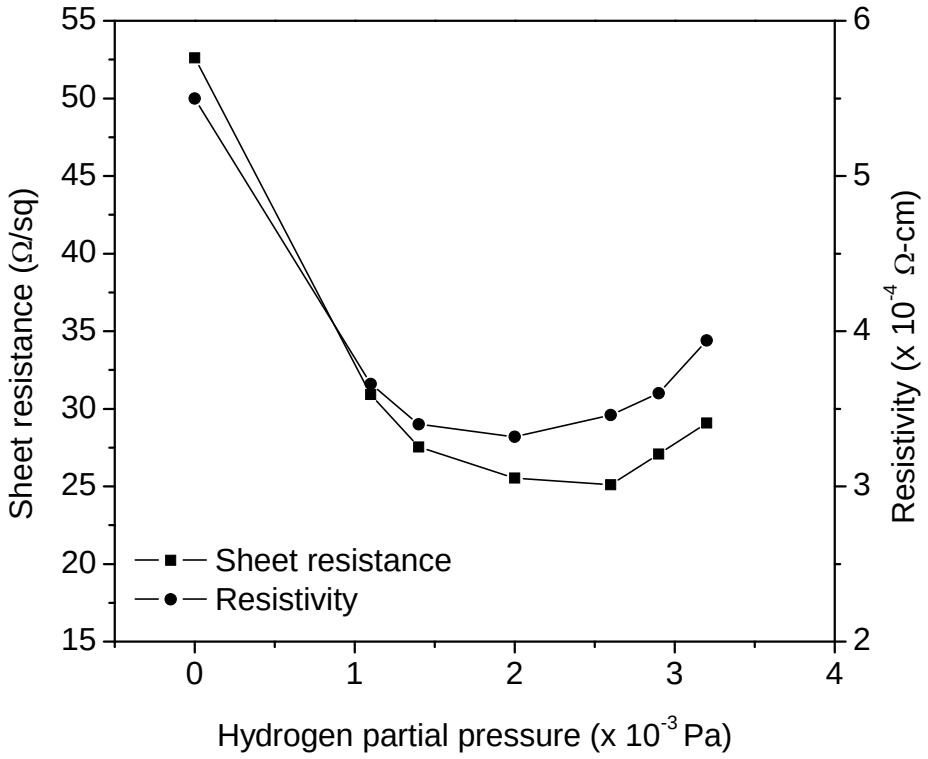

Figure 5.1: Sheet resistance and resistivity of ITO films as a function of hydrogen partial pressure.

When the ITO films prepared at the presence of reactive hydrogen species, the enhancement in the conductivity of ITO films prepared at a presence of hydrogen can be attributed to a high carrier concentration in comparison with those ITO films made without hydrogen in the gas mixture. The use of a hydrogen-argon gas mixture allowed a broader process window for preparation of the ITO film with a high conductivity, e.g. ITO film with a thickness of 130 nm and sheet resistance of 25 ± 5

Ω/sq can be fabricated over the hydrogen partial pressure from about $1 – 3 \times 10^{-3}$ Pa. The relative minimum sheet resistance, ~25 Ω/sq was obtained at a hydrogen partial pressure of 2.6×10^{-3} Pa.

The optical properties of ITO films prepared on glass substrates at different hydrogen partial pressures were also measured. The optical transmittance of the film was measured by a double beam spectrophotometer over the wavelength range from 200 nm to 1000 nm. A blank glass substrate was used as a reference to subtract the baseline absorption from the glass substrate. Measured film transmittance over the visible wavelength range was also used to estimate the optical energy band gap of the films. Figure 5.2 shows the transmittance of a set of 210 nm thick ITO films as a function of hydrogen partial pressure. ITO films with average transmittance of 86%, 89%, 90% and 89% over the visible wavelength of 400 – 800 nm were obtained at the hydrogen partial pressures of 0, 1.1×10^{-3}, 2×10^{-3} and 2.6×10^{-3} Pa, respectively. The hydrogen partial pressure that produced the most transparent ITO film was almost the same as that which gave the most conductive film as shown in Figure 5.1. Except for obvious deviations in the infrared wavelength region, T(λ) of the films prepared at different hydrogen partial pressures also shows a slight difference over the short wavelength range. Figure 5.2 reveals that the short wavelength cutoff in the T(λ) of ITO films prepared at the optimal hydrogen partial pressure of 2.6×10^{-3} Pa shifts towards shorter wavelengths in comparison with that in the T(λ) of ITO films prepared with argon gas. The shift of short wavelength cutoff in T(λ) is related directly to the variation of band gap in the ITO films. In this work, the ITO sputtering

condition (H_2 = 2.6×10^{-3} Pa) which exhibited the best electrical and optical film properties was used for the fabrication of translucent OSC.

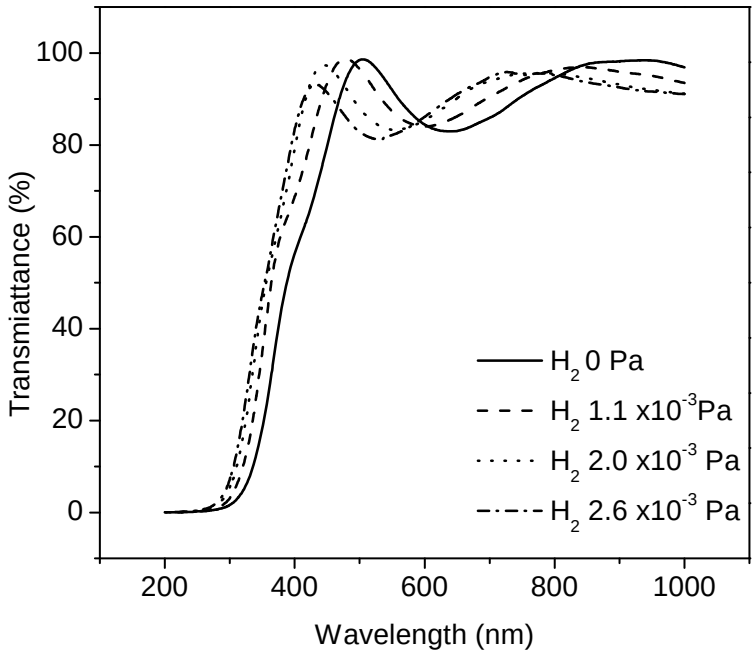

Figure 5.2: Transmittance of ITO thin films as a function of hydrogen partial pressure.

5.3 ITO-based Translucent Cathode

A variety of transparent cathode structures have been developed for application in organic electronics including top-emitting or stacked OLEDs [61, 62] inverted [63, 64], tandem [65-68] and translucent OSC [69-71]. For example, a translucent cathode of Al/Ag/tris-(8-hydroxyquinoline) has been proposed to improve the light coupling in OSCs [64]. Also, an ultrathin layer of Ag nanoparticles [65] or C60:Au [66] and a LiF/Al/Au multilayer [67] have been used as the interlayer in tandem OSCs. A multilayer translucent cathode consisting of a dielectric or an ITO capping layer is often used in order to protect the thin metallic cathode. The capping layer serves as an

optical index matching layer to improve the light coupling in OSC [64]. Bailey-Salzman et al. [69] demonstrated translucent OSCs using a bilayer compound cathode of Ag/ITO. The results show that an average transmission of 26% and a maximum PCE of 0.62% were achieved. The low power conversion efficiency was attributed to the relative low light absorption in translucent OSCs. Recently, a low work function transparent polymer cathode for OSC was also reported [70]. However, the device performance is less than satisfactory due to the poor conductivity of the polymer cathode as compared to that of the ITO layer. In this work, the ITO-based cathode prepared at low processing temperature using Ar/H_2 gas mixture was developed for translucent PSCs. The performance of the PSCs will be discussed in the following sections.

5.4 Optical Properties of Translucent Polymeric Solar Cells

The structure of a translucent PSC was optimized prior to the device fabrication. The integrated absorptance and the total transmittance as a function of P3HT:PCBM thickness for translucent PSCs of the type: glass/ITO/PEDOT:PSS/P3HT:PCBM(25-300nm)/Ca(10nm)/ Ag(10nm)/ITO(60nm), were also calculated and depicted in Figure 5.3. In order to perform a realistic simulation, a 10 nm thick Ag layer was considered in the calculation of the optical properties for translucent PSCs. In the device application, a thin Ag layer was used to improve the lateral electrode conductivity and also prevents the possible damage to the underlying Ca and polymer blend during the ITO deposition. It shows that the transmittance of a translucent cell decreases from about 50% to 25% when the thickness of the P3HT:PCBM layer increases from 25 nm to 300 nm. According to the simulation results shown in Figure

4.6, it was considered that a 75 nm thick P3HT:PCBM layer for a translucent OSC was more preferred. This is because a thinner PSC, e.g., a relative maximum light absorption occurred at a 75 nm P3HT:PCBM layer, enables to achieve good charge transport properties and also posses a good transmission in the visible light wavelength region.

According to Figure 5.3, the translucent PSC with the type: gls/ITO/PEDOT:PSS(40nm)/P3HT:PCBM(75nm)/Ca(10nm)/Ag(10nm)/ITO(60nm) shows a transparency of 42% and an integrated absorptance of P3HT:PCBM of 34%. The curve does not show strong oscillating behaviour because lesser reflection is obtained at the polymer/metal interface for translucent PSC. Ultrathin conventional opaque solar cells have significant constraints on the placement of the peak position of the incident light with respect to the highly reflective cathode used. The use of translucent cathode generally eliminates this constraint. When the P3HT:PCBM thickness increases, the integrated absorptance of OSC increases while the transparency decreases.

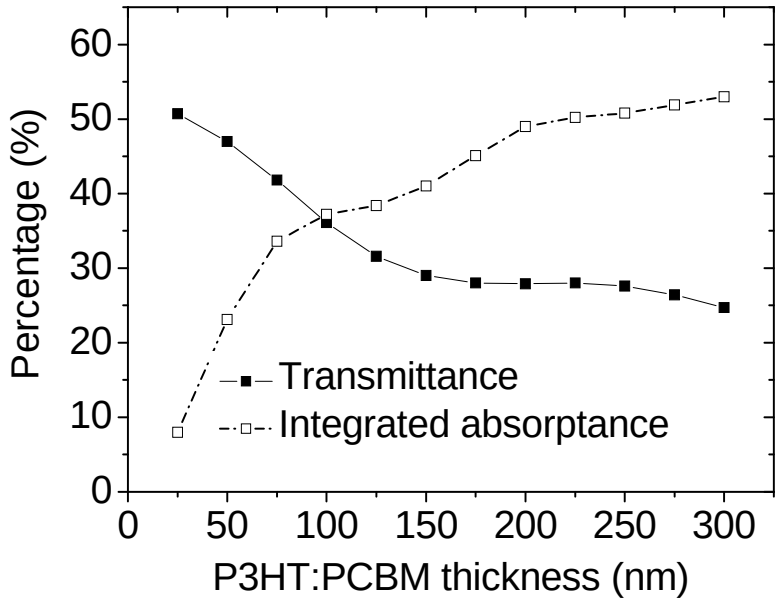

Figure 5.3: Calculated transmittance and integrated absorptance as a function of the active P3HT:PCBM layer thickness for translucent PSCs of the type: glass/ITO/PEDOT:PSS(40nm)/P3HT:PCBM(25-300nm)/Ca(10nm)/Ag(10nm)/ITO(60nm)

In a practical application a translucent PSC with an optimized Ca(10nm)/Ag(10nm)/ ITO cathode is superior to a layer of a thin transparent metal cathode. A translucent OSC finished with a thin metal cathode, e.g., Ca(10nm)/Ag(10-15nm), causes a large internal reflection at the metal/air interface due to its high refractive index. When Ca(10nm)/Ag(10nm)/ITO cathode is used, the unique electric and optical properties of ITO layer allow it to serve as a transparent conducting index matching layer to enhance the total light transmission. This aside, the upper ITO contact also acts as a passivation layer to protect the underlying functional organic layers in OSCs.

The effect of ITO cathode thickness on the total transmittance and integrated absorptance of P3HT:PCBM layer in OSCs was also analyzed and the calculated

results are plotted in Figure 5.4(a). For PSCs with a configuration of glass/ITO/PEDOT:PSS(40nm)/ P3HT:PCBM(75nm)/Ca(10nm)/Ag(10nm)/ITO, the calculated results indicated that a maximum transmittance of the translucent PSCs can be achieved at an ITO cathode thickness of 50nm, whereas the maximum light absorption is occurred in P3HT:PCBM(75nm) at an ITO cathode thickness of 80nm. In order to illustrate the point clearly, a grey region is depicted in Figure 5.4(a), which corresponds to an ITO layer thickness chosen in the region that could result in the demonstrated PSC achieving possible maximum light absorption and transmission simultaneously. In this work, a 60 nm thick ITO-cathode contact was used as an optimal cathode layer, leading to a total transmittance 42% and an integrated absorptance of 34% for a PSC of the type glass/ITO/PEDOT:PSS(40nm)/P3HT:PCBM(75nm)/Ca(10nm) /Ag(10nm)/ITO(60nm).

The wavelength dependent transmittance, T(λ), of the translucent PSCs with two different cathode structures of Ca(10nm)/Ag(10nm) and Ca(10nm)/Ag(10nm)/ITO(60nm) were also calculated and shown in Figure 5.4(b). It can be seen clearly that T(λ) of the PSC with Ca(10nm)/Ag(10nm)/ITO(60nm) cathode has a higher transmittance throughout the whole visible light wavelength region as compared to the structurally identical OSC using Ca(10nm)/Ag(10nm) as a translucent cathode. The above analysis and the thin film simulation approach are useful for optimizing the structure of tandem OSCs as well [93].

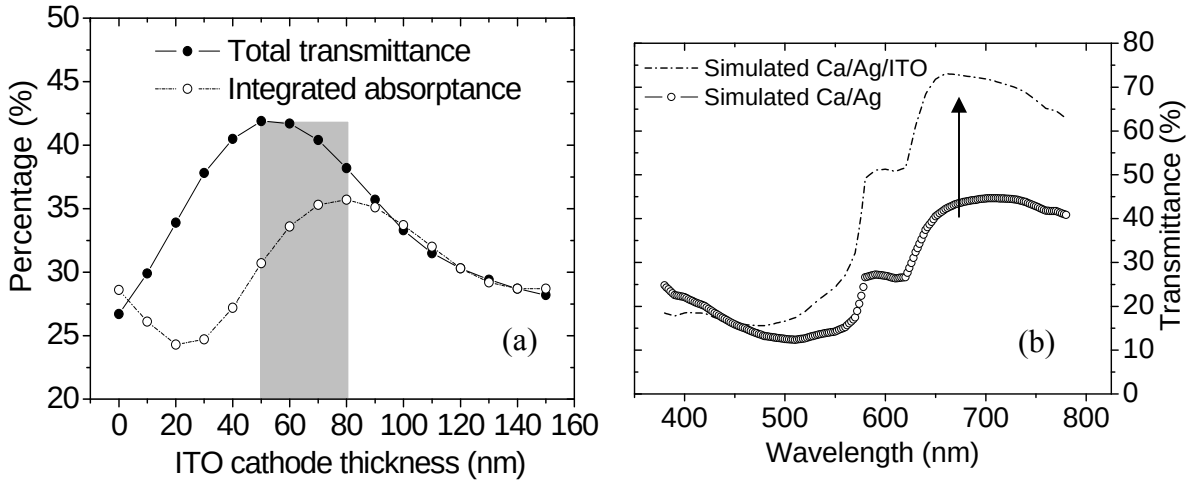

Figure 5.4: (a) Calculation of the effect of the ITO cathode layer thickness on the integrated absorptance of P3HT:PCBM layer and the transmittance of PSCs of the type: glass/ITO/PEDOT:PSS(40nm)/P3HT:PCBM(75nm)/Ca(10nm)/Ag(10nm)/ ITO(0-160nm). (b) Transmission spectra calculated for two structurally identical PSCs with a translucent cathode of Ca(10nm)/Ag(10nm) and Ca(10nm)/Ag(10nm)/ITO(60nm).

5.5 Photovoltaic Performance of Translucent Polymeric Solar Cells

The devices using a translucent ITO-cathode layer were prepared based on the layer thickness obtained by the optical admittance analysis (Figure 5.4a). In the following discussion, a control PSC (A1) with a configuration of glass/ITO/PEDOT(40nm)/ P3HT:PCBM(75nm)/Ca(10nm)/Ag(100nm) was used as a reference device, and the J-V characteristics of the control PSC was compared with that of a structurally identical PSCs (A2 and A3) made with a translucent cathode of the type Ca(10nm)/Ag(10nm)/(optimized-ITO) and Ca(10nm)/Ag(10nm)/(ITO, prepared using high sputtering power), respectively. The spectral response and J-V characteristics for all control and translucent PSCs were measured under calibrated AM1.5 solar simulator in the nitrogen glove box.

The IPCE of a control cell A1 (59%) was higher than that of a translucent cell A2 (34%) and A3 (8%) at λ=510nm. The IPCE curves are similar in shape as shown in Figure 5.5(a). The shoulder at 362 nm was predominantly from the PCBM and resembles the light absorption in P3HT with the main peak at 507 nm and shoulders at 550 and 605 nm for control device. A shift of the PCBM peak for A2 could be attributed to the interference effects in the thin film system. For device A3, the curve shape is totally deformed and different from A1 and A2 with the high possibility that the active layer was damaged by the high sputtering power used during ITO-cathode deposition process.

The control device A1 yielded a higher current density of 8.22 mA/cm^2 in comparison with that of the translucent cells A2 (Jsc=6.89 mA/cm^2) and A3 (Jsc=0.41 mA/cm^2). At the same time, the fill factor of A3 is lower than that of A1 and A2 limiting the energy conversion efficiency. The increment in the photocurrent density of A3 is lower than that observed for the device A1 and A2 (Figure 5.5(b)). This indicates that the series resistance of A3 is much higher than that of A1 and A2. The high series resistance is responsible for the low short circuit current density in A3 according to ECD diagram shown in Figure 2.5. For the comparison in Voc, both A1 in A2 devices are nearly the same while A3 shows a dropped of 0.2V. Since the Voc is generally influenced by the work function difference between cathode and anode materials, the possible reason for the decrement in Voc for A3 is that the polymer/cathode interface has been deteriorated by the high power sputtering process even a capping 10nm Ag layer is used. The deterioration of the cathode contact during the ITO preparation, which was deposited by the high power sputtering

process, is the possible reason of the formation of a thin poor conducting CaO layer at the Ca/Ag interface. This could be an origin of the unexpected increased in series resistance of the translucent polymer PV device. This explains the clear kink showed in the J-V characteristic of A3.

For the comparison between A1 and A2, The use of high quality translucent Ca(10nm)/Ag(10nm)/optimized-ITO(60nm) cathode yielded a higher fill factor (FF), but a relatively lower J_{sc} of 6.89 mA/cm^2 in comparison with that of 8.22 mA/cm^2 measured for the control PV cell (A1), as shown in Figure 5.5(b). The slight decrease in the photocurrent density of A2 is expected as more than 30% of the incident light is transmitted through the cell. The V_{oc} measured for A1 and A2 are nearly the same. The PV characteristics measured for the control and translucent PSCs are summarized in Table 5.1 [94].

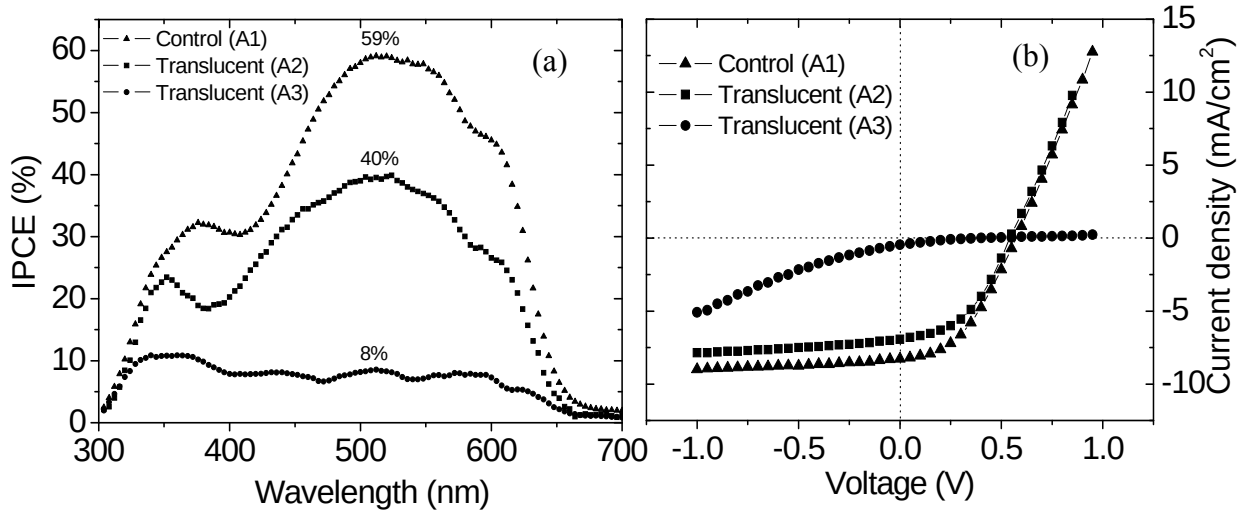

Figure 5.5: A comparison of the IPCE spectral (a) and I–V characteristics (b) measured for a control PSC A1 and translucent PSC A2 and A3.

Table 5.1: PV characteristics of control OSC (A1) and translucent PSC A2 and A3.

	IPCE (%)	**V_{oc} (V)**	**J sc (mA/cm^2)**	**FF (%)**	**PCE (%)**
A1	59.0	0.57	8.22	43	2.02
A2	40.0	0.54	6.89	46	1.70
A3	8.00	0.36	0.41	20	0.03

The simulated and measured light transmission of translucent PSCs made with two different cathode structures of Ca(10nm)/Ag(10nm) and Ca(10nm)/Ag(10nm)/LP-ITO is shown in Figure 5.6. It can be seen clearly that PSCs with a Ca(10nm)/Ag(10nm)/ITO(60nm) cathode have a higher transmittance throughout the whole visible light wavelength region (red curve) as compared to a structurally identical PSC having a thin layer Ca(10nm)/Ag(10nm) cathode (green curve). The Ca(10nm)/Ag(10nm) cathode in OSC causes a large amount of internal reflection at the metal/air interface, leading to a low transmittance.

When a Ca(10nm)/Ag(10nm)/ITO cathode is used, the top ITO layer serves as a transparent conducting index matching layer that enhances the total light transmission, resulting in an average light transmission of ~ 30% over the visible light wavelength. This aside, the simulated and measured transmittance for both translucent cells with and without ITO index matching layer show an overall good agreement with each other. The measured transmittance of the translucent OSC does not overlap exactly as compared to that of the simulated transmittance obtained for the same device, the deviation in the transmittance between the experimental and calculated transparency in the devices may be attributed to the assumption of a perfect film

smoothness, while it might be not true in reality as the inhomogeneity of the actual organic thin films may be expected [94].

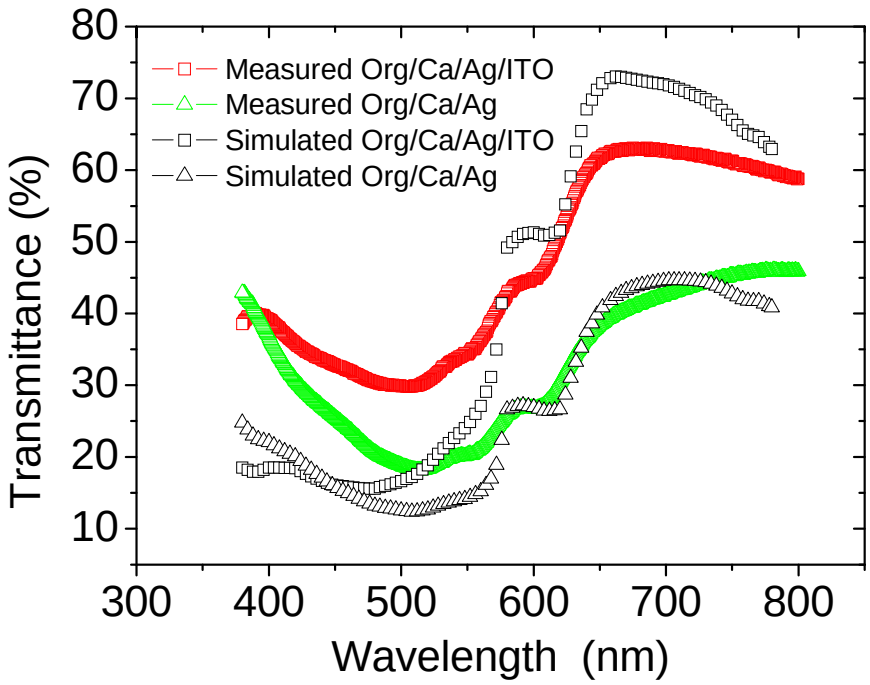

Figure 5.6: Comparison of transmission spectral measured for translucent PSCs with configuration of glass/ITO/PEDOT:PSS(40nm)/P3HT:PCBM(75nm)/Ca(10nm)/ Ag(10nm)/LP-ITO (red curve) and a control PSC of glass/ITO/PEDOT:PSS(40nm)/ P3HT:PCBM(75nm)/Ca(10nm)/Ag(10nm) (green curve). The simulated curves for both configurations are drawn in open rectangle and triangle curve respectively

Upon successful demonstration of the high performance translucent PSCs, we laterally integrated the devices to maximize the output power. Figure 5.7 shows a schematic diagram of a lateral integration design for translucent PSC which has been developed in this research work. The integrated translucent PSC is able to generate sufficient electricity to power up small toys and calculator as shown in Figure 5.8, which shows great potential in applications such as tinted windows, architecture surfaces and antistatic coating application.

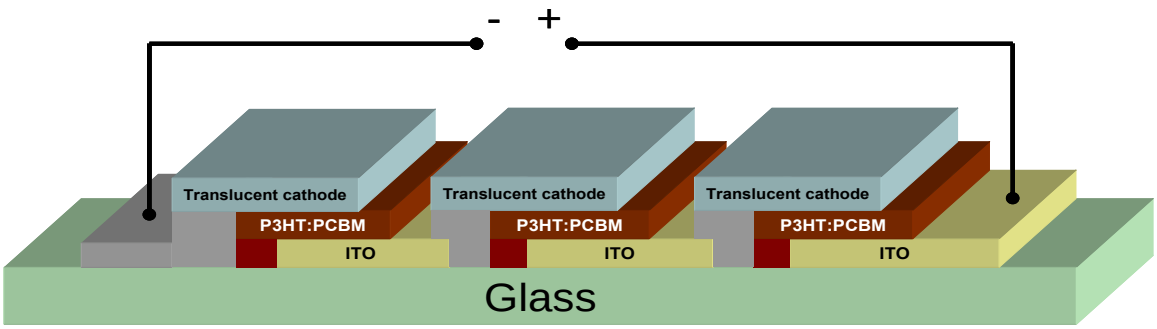

Figure 5.7: A schematic diagram of lateral integration of translucent PSCs.

Figure 5.8: (a) A lateral integrated translucent PSC demonstrator with total active area of 1.5cm^2. (b) a photo picture of a calculator which was powered up using a translucent PSC, and (c) a photo picture of electronic device (toy) running using the power generated by a translucent PSC.

5.6 ITO Interlayer for Tandem Polymeric Solar Cells

With the success of demonstrating ITO-cathode for application in translucent OSCs, the research work was expanded to study the ITO cathode as an interlayer, also known as RZ, for application in tandem PSCs. The purpose of this section was to study the feasibility of ITO as RZ for the solution-processed tandem PSCs. The tandem PSC was formed by stacking a sub-cell on top of the translucent PSC using the same organic solvents. This was to verify whether the ITO interlayer developed in this work was able to prevent the possible damage to the bottom cell using the same organic solvent for the top cell. As the two sub-cells are connected in series, the photocurrent generated in the tandem PSC is determined by the one which generates lesser photocurrent. Hence, the current matching condition in tandem OSC is essential and prerequisite for meeting performance and stability. The bottom cell eventually acted as an optical filter to limit the incident light reaching to the top cell. In other words, the top cell absorbs lesser incident photons and led to lesser overall photogenerated current. The active layer in the bottom cell had to be thinner to minimize the filtering effect. Due to the high absorption coefficient of conjugated polymers such as P3HT and PCBM, thin layer thickness (~75nm) was sufficient to absorb about 30% of the incident photons (Figure 5.2). Hence, stacking another P3HT:PCBM PSC on top of the bottom cell was expected to capture the remaining 70% incident photons

The optimal structure of P3HT:PCBM-based tandem PSC was studied using optical admittance analysis. The ITO layer served as an optical spacer to redistribute the light propagation in the multilayer thin film system so that the relative maximum light absorption were then located in the active region in both the bottom and the top

cells, hence maximizing balanced absorption for both stacked cells since the photogenerated exciton exhibited direct relationship with the light absorption.

A high performance ITO-based cathode developed in this work was used for application in organic photovoltaic cells. The thickness of the ITO-based RZ is also optimized to address the enhancement of light distribution in both top and bottom PSC units**.** Figure 5.9 shows the energy band level of each component material in the tandem cell structure used in this work. The relatively high work function of ITO (4.8eV) as compare to most of the metals such as Ag and Al, minimizes the energy barrier for hole collection from the top cell. The use of ITO enables the stacking of repeating cell to absorb the uncaptured light by the bottom cell. The ITO-based RZ also potentially acted as an intermediate protection firm foundation and also protection layer to prevent possible damage to the first cell during the subsequent fabrication of a top unit solar cell.

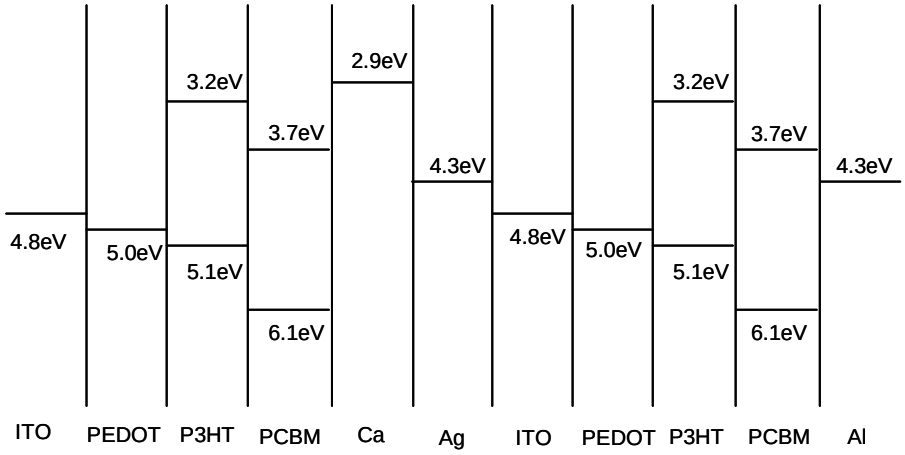

Figure 5.9: Energy level diagram showing individual HOMO and LUMO energies of each of the component materials used in this work.

The integrated absorptance and transmittance of the translucent PSC as a function of Ca and Ag thicknesses cathode combination were shown in Figure 5.10. When a translucent cathode of Ca(3nm)/Ag(3nm)/ITO(60nm) was used, the transmittance of the cell was as high as 56% as compared 42% obtained for an identical cell with the translucent cathode of Ca(10nm)/Ag(10nm)/ITO(60nm). The difference in the integrated absorptance in both cases was only 4%. Hence, Ca(3nm)/Ag(3nm)/ITO(60nm) was used as the RZ in order to enhance the light absorption in the top cell, at the same time without losing the light absorption of the bottom cell significantly.

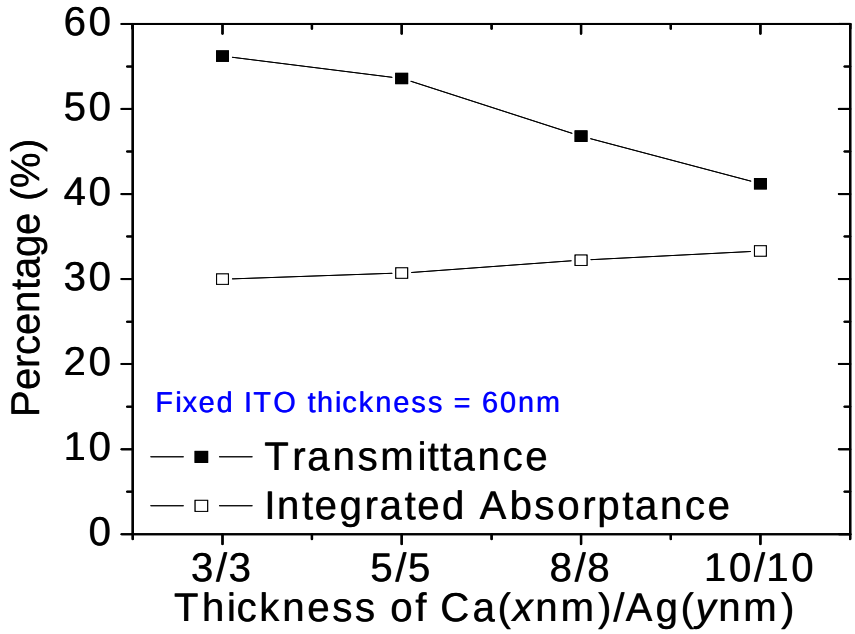

Figure 5.10: The integrated absorptance and transmittance of the translucent PSC as a function of the Ca/Ag thickness.

The translucent PSC (A4) with the structure of A4: glass/ITO/PEDOT:PSS(40nm)/ P3HT:PCBM(75nm)/Ca(3nm)/Ag(3nm)/ITO(60nm) was fabricated and the comparison of J-V characteristic and a spectral response with

Ca(10nm)/Ag(10nm)/ITO(60nm) (A2) are plotted in Figure 5.11. According to Figure 5.11(a), a slight difference in the spectra response is observed due to the interference effect. However, the translucent PSC with the structure of glass/ITO/PEDOT:PSS(40nm)/P3HT:PCBM(75nm)/Ca(3nm)/Ag(3nm)/ITO(60nm) showed a decreased in Jsc value from 6.89mA/cm^2 to 5.30mA/cm^2 as shown in Figure 5.11(b). The relatively low photocurrent density generated in device A4 could be due to the charge collection efficiency is not as good as the one with Ca(10nm)/Ag(10nm)/ITO(60nm). It is possible that Ca(3nm)/Ag(3nm)/ ITO(60nm) might not form a uniform continuous layer as compared to the Ca(10nm)/ Ag(10nm)/ITO(60nm). However, the 14% increment in the transparency favoured the construction of tandem cell. This aside, the newly developed ITO-cathode generates almost no damage to the underlying layer even though only 3nm of Ag is used as a protection layer. A summary of OSC characteristics is given in Table 5.2.

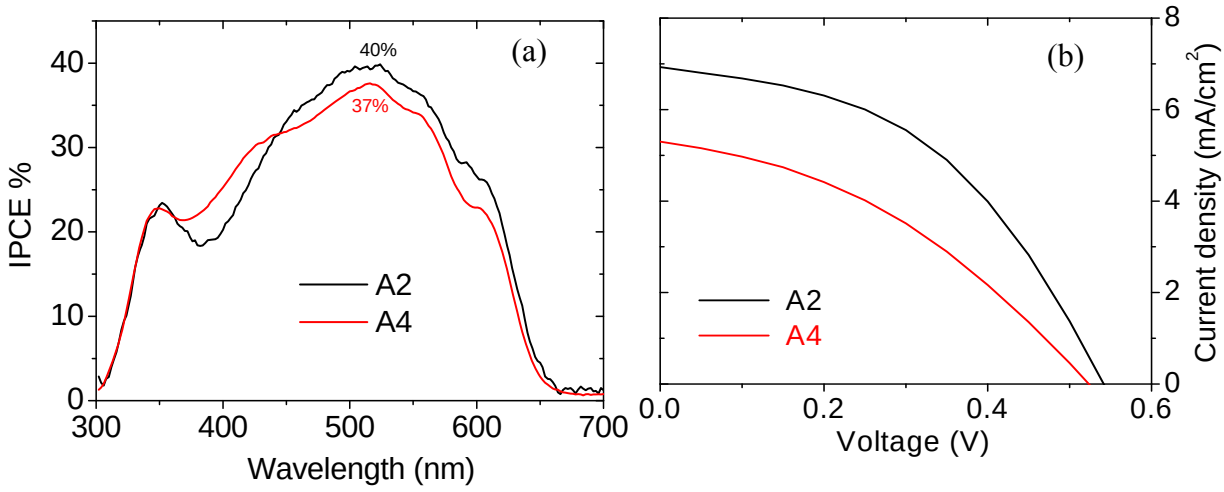

Figure 5.11: A comparison of the IPCE spectral (a) and IV characteristics (b) measured for translucent PSCs of glass/ITO/PEDOT:PSS(40nm)/ P3HT:PCBM (75nm)/Ca(10nm)/Ag(10nm)/ITO(60nm) and glass/ITO/PEDOT:PSS(40nm)/ P3HT:PCBM(75nm)/Ca(3nm)/Ag(3nm)/ITO (60nm).

Table 5.2: A summarized PV characteristics of the translucent PSCs with different Ca and Ag thickness

	IPCE (%)	V_{oc} (V)	J_{sc} (mA/cm^2)	FF (%)	PCE (%)
A2	40.0	0.54	6.89	46	1.70
A4	38.0	0.52	5.30	38	1.05

The current matching condition for solution-processed tandem PSC was also studied using optical admittance analysis. In the simulation, the Ca and Ag thickness were kept constant at 3nm each, the layer thickness of P3HT:PCBM for both the top and bottom sub-cells were optimized so that the same integrated absorptance was reached. The calculation for tandem structure of glass/ITO/PEDOT:PSS(40nm)/P3HT:PCBM(75nm)/Ca(3nm)/Ag(3nm)/ITO(*x*nm)/ PEDOT:PSS(40nm)/P3HT:PCBM(200nm)/Al(100nm) was obtained. A 200nm thick P3HT:PCBM was chosen as the active layer for top cell in this work. This is because an active layer with a layer thickness greater than 200nm might not be favourable for charge transport. According to the results shown in Figure 5.12a, no absorption matching in OSCs with the structure of: ITO/PEDOT:PSS(40nm)/P3HT:PCBM(75nm)/Ca(3nm)/Ag(3nm)/ITO(*x*nm)/ PEDOT:PSS(40nm)/P3HT:PCBM(200nm)/Al(100nm) can be obtained. The results reveal that the light distribution in the multilayer thin film system can be optimized by adjusting the ITO interlayer thickness. According to device structure of Tandem 1, more light can be absorbed in bottom cell than in the top one, which means that the active layer thickness in the bottom cell may be too thick as both cell exhibited the same absorption spectrum. A bottom cell with a layer thickness of 50nm

was tested in the device simulation. As shown in Figure 5.12(a), the tandem PSC (Tandem 2) showed two absorption matching conditions when the ITO is 0nm and 95nm. The calculation shows that 0nm ITO thickness might not be feasible in practical. The bottom cell might be washed away during the spin coating of top cell without the presence of an ITO RZ layer. In addition, pure Ag contact is not favourable for hole collection from the top cell.

According to Figure 5.12(b), the spectra response for both top and bottom cells was calculated. As can be clearly seen, bottom cell contributed more in the region where the P3HT:PCBM has the higher absorption coefficient (region II), whereas for top cell, it absorbed more light in the region I and III where P3HT:PCBM system has relatively low absorption cross section. This figure shows the photon energy distribution in tandem cell where balanced absorption is achieved. This is especially important for a proper design the structure of tandem PSCs.

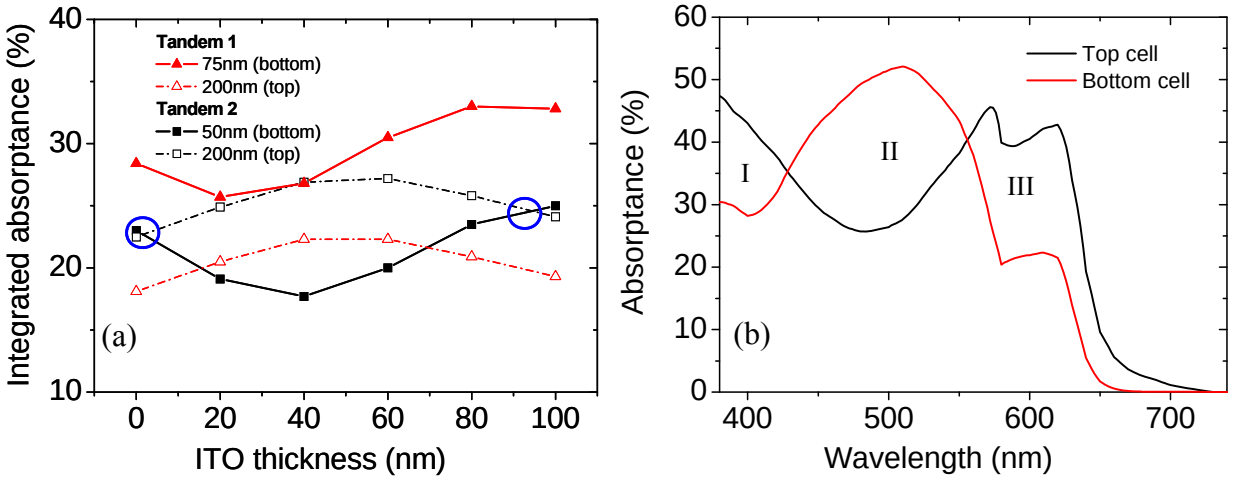

Figure 5.12: A comparison of the calculated (a) integrated absorptance and (b) spectra response of Tandem 1 and Tandem 2.

When a balanced absorption condition for the top and bottom cells was achieved, a solution-processed tandem PSC (Tandem 2) with the corresponding device structure was fabricated. The RZ was extended to the outer circuit during the fabrication process so that the bottom cell can be measured. According to Figure 5.13(a), the Voc of the bottom cell was 0.51V. It is almost similar to the one that was fabricated in Figure 5.11 (0.52V). The1.7 times improvement in the Voc was observed for the tandem PSC. However, the photogenerated current was smaller (3.19 mA/cm^2) than the bottom cell (4.42mA/cm^2) with the high possibility of the top cell was the limiting factor. This is because the photocurrent of a tandem OSC is determined by the sub-cell having the lowest current in the system, due to the series connection for individual cell. Figure 5.13(b) showed the comparison between the normalized simulated spectra response and the IPCE of the tandem cell. Both curve matched well except the shoulder at λ=600nm. This is because the simulation assumed all the interfaces are well defined and neglect the scattering effect at the interfaces. In reality, scattering effect happens at the interfaces that mostly are intermixed. A summary of the PV characteristics is shown in Table 5.3.

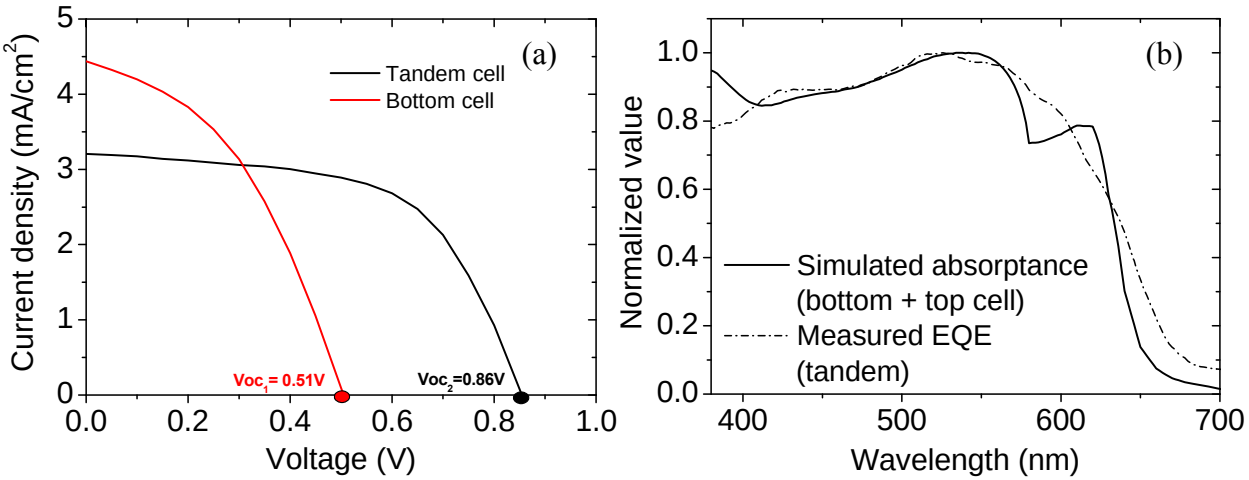

Figure 5.13: (a) The J-V characteristic and (b) A comparison between simulation and normalized spectra response of the tandem structure of glass/ITO/PEDOT:PSS(40nm)/P3HT:PCBM(50nm)/Ca(3nm)/Ag(3nm)/Optimized-ITO (95nm)/PEDOT:PSS(40nm)/P3HT: PCBM(200nm)/Al(100nm).

Table 5.3: A summarized PV characteristics of tandem PSC

	V_{oc} (V)	**J sc (mA/cm^2)**	**FF (%)**	**PCE (%)**
Bottom cell	0.51	4.42	42	0.94
Tandem cell	0.86 (1.7times)	3.19	59	1.61

5.7 Conclusion

In conclusion, optical admittance analysis was used to optimize the structure of PSCs. Translucent PSCs with a configuration of glass/ITO/PEDOT:PSS (40nm)/P3HT:PCBM (75nm)/Ca(10nm)/Ag(10nm)/ITO(60nm) were demonstrated. The results of this work have yielded translucent P3HT:PCBM based PSCs with an average transmission of more than 30% in the visible light wavelength range and a relatively high power conversion efficiency of 1.7%. The optimized ITO-based translucent cathode described in this work can be used as an optical spacer for better light harvesting in stacked translucent polymer or small molecule PV cells. 1.7 times

enhancement in Voc is demonstrated in this thesis. There are many possible applications for translucent PSCs. For example, it can be integrated with OLEDs and polymer waveguides for organic optical switches [95] and flexible optical circuits [96].

Chapter 6

Charge Transport and Device Stability Studies in Polymeric Solar Cells

The development of efficient and stable PV cells is the major challenge with the current BHJ-based PSC technology. The efficiency and operational stability of BHJ based PSCs are strongly dependent on the charge transport properties in the active layer of the device. In BHJ based PSCs, the charge carriers generated by photoinduced charge transfer from the electron donor (conjugated polymer) to the electron acceptor (Fullerene) need to be transported to the respective electrode, which depends on the charge mobility in the active material. It is well known that the nature of charge transport in polymeric semiconductors significantly varies with the film processing conditions such as the polarity of the organic solvent used for film preparation, solution concentrations, spin-coating procedures, and annealing temperatures. For example, Sirringhaus et al. have demonstrated that the charge mobility in P3HT can reach as high as 10^{-1} cm^2/Vs [97] if the orientation of the polymer chain is controlled through the fabrication process. Inigo et al. [98] have reported that the nature of charge transport in MEH-PPV films is depending on the solvent used for film preparation. It has also been reported that the formation of structural defects during polymerization significantly alters charge mobility characteristics which in turn affects the stability of the device [99]. In addition, the charge mobility in conjugated polymer/fullerene composite film depends on the phase separation process, in which

the thermal treatment or slow evaporation rate during film deposition significantly changes the nanomorphology of the composite film. The interfaces between the donor and acceptor nanophases have significant effect on the charge trapping or charge recombination behavior, which in turn influences on the device efficiency and device lifetime. Therefore the systematic investigation on the charge transport properties in the active PV materials is important to improve the device efficiency as well to investigate the device lifetime issues.

It has been shown in the literature that the charge transport properties in PV materials especially in the composition of an electron donor (p-type materials) and electron acceptor (n-type materials) can be successfully investigated using a novel technique called photoinduced charge extraction by linearly increasing voltage technique (PhotoCELIV) [107, 108]. The PhotoCELIV technique can be used to study the mobility and lifetime of both charge carriers simultaneously in the real PV device configuration. Mozer et al. have investigated the charge transport and recombination properties in MDMO-PPV:PCBM based solar cell using the PhotoCELIV technique and found that the charge mobility increases by two orders of magnitude with increasing PCBM concentration [109]. The information about the lifetime of the charge carriers and the nature of charge transport (dispersive or nondispersive) were also obtained from the shape of the PhotoCELIV transients [110]. The charge transport properties of P3HT:PCBM composite film have also been investigated [111]. The reported charge mobility value for the P3HT:PCBM composite film is 3×10^{-4} cm^2/Vs [111]. Although the charge transport properties in

P3HT:PCBM based conventional PV devices have already been studied, the effect of translucent cathode on the charge mobility in the active P3HT:PCBM film is not investigated. In this thesis, PhotoCELIV technique was used to study the charge mobility characteristics in a series of translucent PSCs, with the device architecture of ITO/PEDOT:PSS/P3HT:PCBM(200nm)/Al/ ITO(60nm), by varying the thickness of the Al layer. It has already been observed that the device efficiency of a translucent PSCs is less than the efficiency observed for a conventional PSC with a device architecture of ITO/PEDOT:PSS/P3HT:PCBM(200nm)/Al(100nm). As translucent PSCs have several advantages compared to the conventional PSC, it is important to identify the issues associated with the translucent PSCs and to find the ways to solve the issues. Therefore, the aim of this investigation is to study the effect of Al contact on the charge mobility characteristics in the photoactive layer and to correlate the charge transport parameters with the device performance parameters such as the efficiency and the stability. The charge transport and device performances were also compared between the translucent PSCs and conventional opaque PSCs. The film preparation conditions, the concentration and composition of the blends were same, so that the effect of different Al thicknesses in the translucent cathode on the charge mobility and device performance parameters can be compared.

6.1 Studies of Charge Transport Properties in Translucent Polymeric Solar Cells using PhotoCELIV technique

The charge transport properties in translucent PSCs with different Al thicknesses were studied using the PhotoCELIV technique. The experimental details of the PhotoCELIV technique is described in section 3.2.5. The device architectures used for the PhotoCELIV studies were:

Device P1: Glass/ITO/P3HT:PCBM(200nm)/Al(100nm)

Device P2: Glass/ITO/P3HT:PCBM(200nm)/Al(10nm)/ITO(60nm)

Device P3: Glass/ITO/P3HT:PCBM(200nm)/Al(5nm)/ITO(60nm)

The active PV materials used for this investigation were the composite film of P3HT:PCBM (200nm) as it is a widely used material for BHJ based PSCs. The PhotoCELIV transients in these translucent PSCs were recorded by illuminating the device through the ITO anode and by varying the rate of change of voltage ramp (A). The delay between the laser pulse and the voltage ramp was fixed to t_{del} = 20μs and the temperature was fixed to T = 295K. Figure 6.1(a) shows the room temperature PhotoCELIV transients in P1 for various rates of change of voltage ramps (A). It is observed that the transit time, refers to t_{max} value, decreases with the increase of A. This indicates that the charge mobility was dependent on the applied electric field. The variation of charge mobility with applied electric field was calculated according to Equation 3.4 and shown in Figure 6.1(b). The charge mobility varied from 2×10^{-4} cm^2/Vs to 3.5×10^{-4} cm^2/Vs for the electric fields studied, the observed charge mobility was assigned to of holes based on the mobility values obtained for pure P3HT.

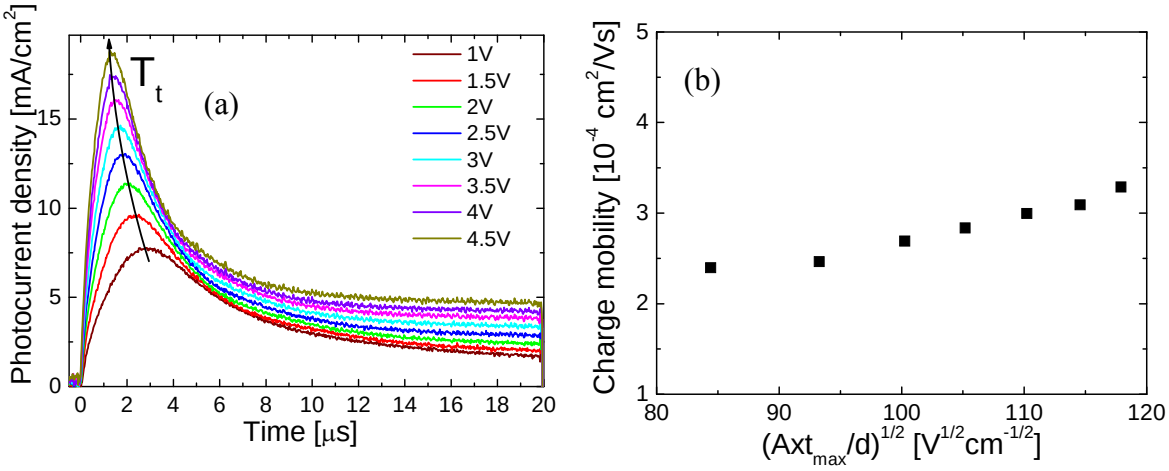

Figure 6.1: (a) PhotoCELIV transients for the device P1: ITO/P3HT:PCBM(200nm)/Al (100nm), (b) the variation of charge mobility with applied electric field.

The PhotoCELIV transients obtained for the pure P3HT film is shown Figure 6.2(a) in order to make a comparison between the charge mobility of pure P3HT film and the charge mobility obtained for the P3HT:PCBM film. The variation of charge mobility with applied electric field for pure P3HT film is also shown Figure 6.2(b). The obtained charge mobility values for the pure P3HT film and the P3HT:PCBM composite film using the PhotoCELIV technique is consistent with the reported value [111].

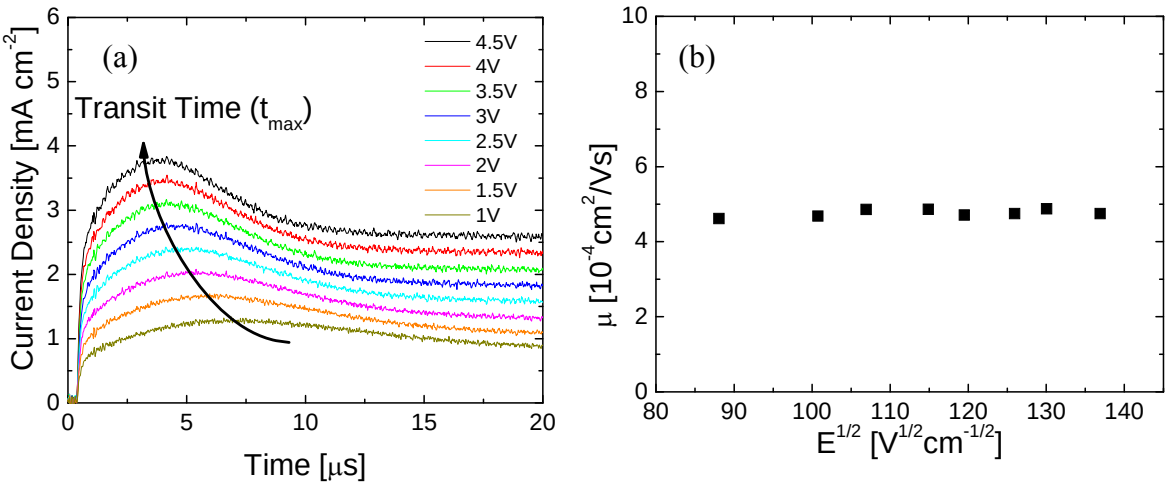

Figure 6.2: (a) PhotoCELIV transients for the device with architecture: ITO/P3HT (435nm)/Al(100nm), (b) the variation of charge mobility with applied electric field.

The charge mobility characteristics of devices of the translucent PV devices P2 and P3 have also been studied using the PhotoCELIV technique. The PhotoCELIV transients recorded for the devices P2 and P3 are shown in Figures 6.3(a) and 6.4(a) respectively. The variation of charge mobility with applied electric field for devices P2 and P3 are also shown in Figures 6.3(b) and 6.4(b) respectively. It has been observed that the PhotoCELIV transit time varies with the rate of change of voltage (A) for both of the devices P2 and P3, which indicated that the charge mobility was driven by the applied electric field. However, the charge mobility values obtained for the translucent PSC's (~10^{-5}cm^2/Vs) are more than one order magnitude less than the charge mobility values obtained for the conventional PSCs, e.g. (~10^{-4}cm^2/Vs) although the active PV material is the same for all the devices studied. In addition, it has also been observed that the charge mobility was decreasing systematically with the decrease of Al thickness in the cathode. It has been seen from the Figures 6.3(a) and 6.4(a) that the devices P1 and P2 exhibited single peak in the PhotoCELIV

transients, which was assigned to holes. However, the PhotoCELIV transients obtained for the device P3 exhibited dual peaks for all the rate of change of voltage ramps studied. The dual peaks in the PhotoCELIV transients are only observed from the translucent device with 5nm Al (in the cathode) and the obtained results are reproducible with all the studied devices with similar architecture. The translucent device with 5nm Al based on pure P3HT active layer was fabricated, and the charge mobility characteristics were studied using PhotoCELIV technique in order to identify the source for the dual PhotoCELIV peaks in P3. The PhotoCELIV transients observed for pure P3HT film with translucent device architecture (5nm Al in the cathode) exhibited a single peak. This indicates that the dual PhotoCELIV peaks obtained for device P3 is related to the charge mobility in the PCBM phase. Therefore, the second peak appeared in device P3 at longer time scale may be assigned to the trapped electrons. In addition, the width of the PhotoCELIV transients is used to quantify the dispersion in the active materials. The charge dispersion is directly proportional to the width of the PhotoCELIV transients. The observed results indicated that the charge dispersion was the highest for P3 compared to P1 and P2.

Generally, it is expected that the electrode modification mainly influences only the device performance parameters, but not the charge mobility characteristics in the photoactive materials. The obtained results from this investigation indicate that the charge mobility in the active material is also affected by the modification in the electrode. The observed results suggest that the property of the photoactive layer was changed during the fabrication of Al/ITO(60nm) cathode. The main reason for the

observed lower charge mobility with the translucent devices may be due to the migration of oxide into the photoactive film which may change the properties. In addition, the interaction between the oxide and PCBM may be the main cause for the trapping of electrons in the translucent PSCs with thin Al electrode.

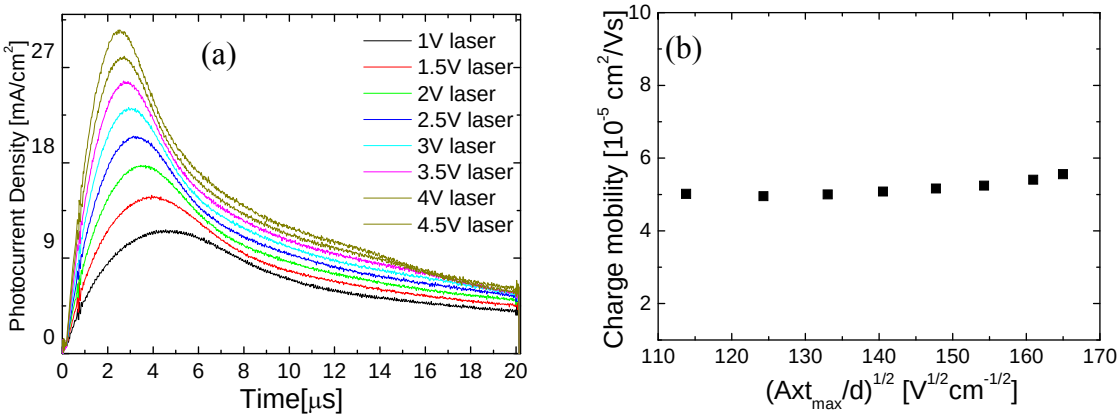

Figure 6.3: (a) PhotoCELIV transients for the device P2: ITO/P3HT:PCBM(200nm)/Al (10nm)/ITO(60nm), (b) the variation of charge mobility with applied electric field.

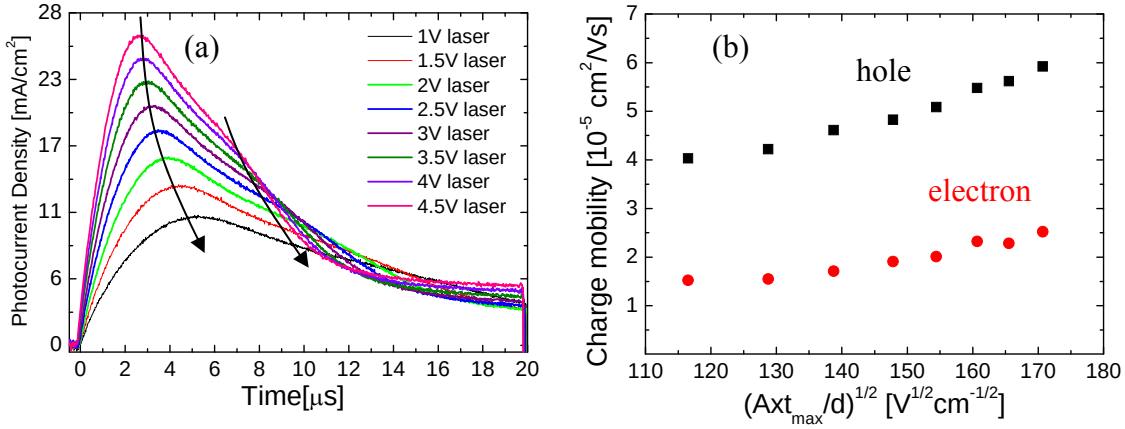

Figure 6.4: (a) PhotoCELIV transients for the device P3: ITO/P3HT:PCBM(200nm)/Al (5nm)/ITO(60nm), (b) the variation of charge mobility with applied electric field.

The current-voltage and lifetime characteristics of PSC devices were also investigated, and the results were correlated to the PhotoCELIV measurements to better understand the effect of charge mobility characteristics on the device performance.

6.2 Effect of Cathode Combination on Efficiency and Stability of Translucent Organic Solar Cells

The current-voltage and stability behaviour of the devices were investigated using Al/ITO(60 nm) cathode having different Al contact layer thicknesses. The structures of the devices used for this investigation were:

Device B1: Glass/PEDOT:PSS/ITO/P3HT:PCBM(200nm)/Al(100nm)

Device B2: Glass/PEDOT:PSS/ITO/P3HT:PCBM(200nm)/Al(10nm)/ITO(60nm)

Device B3: Glass/PEDOT:PSS/ITO/P3HT:PCBM(200nm)/Al(5nm)/ITO(60nm)

The only difference between the device architectures used for charge transport studies and device performance studies is the inclusion of PEDOT:PSS layer in the devices used for J-V and lifetime characterization. The translucent cathode used in this section was Al/ITO, which was different from the one used in the previous chapters (Ca/Ag/ITO). This is because Ca is more prone to oxidation as compared to Al. However, both Ca/Ag/ITO and Al/ITO translucent cathodes were practically functioned well in the translucent PSCs in inert environment demonstrated in this work. Devices B1, B2 and B3 were characterized under simulated AM1.5 solar irradiation with the power intensity of 100mW/cm^2. The important PV parameters were calculated and summarized in Table 6.1. The J-V characteristic curves for the

devices B1, B2 and B3 were plotted and shown in Figure 6.5. It has been observed that the PCE of solar cells decreases with decrease of Al thickness in the translucent cathode. The PCE values obtained for the devices B1, B2 and B3 are 2.31%, 1.54% and 1.15%, respectively. The short circuit current Jsc (B1: 8.27mA/cm, B2: 6.60mA/cm^2 and B3: 5.99mA/cm^2) and FF (B1: 49.0%, B2: 42.0% and B3: 36.1%) also showed the similar trend as these parameters decreases with the decrease of Al thicknesses. However, the V_{oc} remained almost similar for all devices.

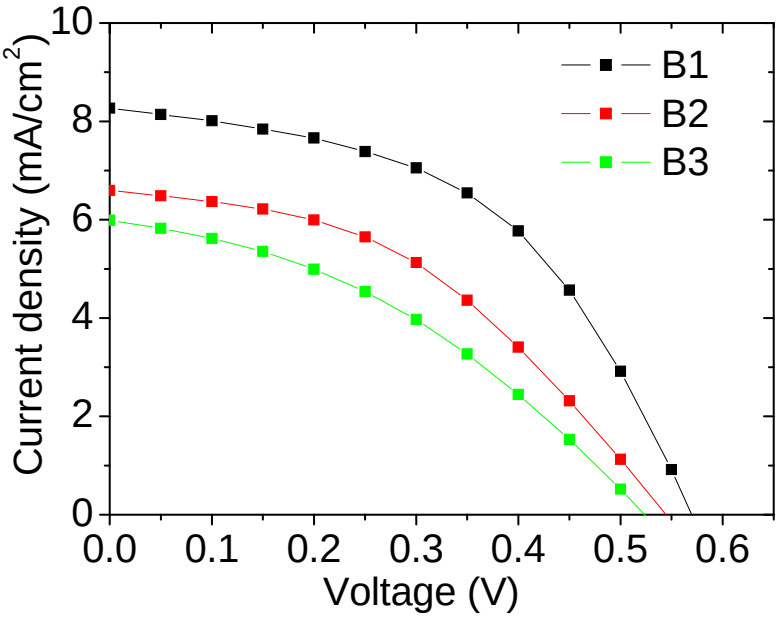

Figure 6.5: J-V characteristics of translucent PSCs of B1, B2 and B3 characterized under simulated AM1.5 solar irradiation in an inert gas glove box environment.

Table 6.1: Important PV parameters of translucent PSCs B1, B2 and B3.

	B1	B2	B3
PCE (%)	2.31	1.54	1.19
FF (%)	49.0	42.0	36.1
Jsc (mA/cm^2)	8.27	6.60	5.99
Voc (V)	0.57	0.56	0.55

It is well known that the short circuit current is directly proportional to the amount of light absorbed in the photoactive material. Therefore, we have calculated the integrated light absorptances for the devices B1, B2 and B3 using optical admittance as described in Equation 4.7 and the obtained values are listed in Table 6.2. As per the calculation, 58% of the incident light is absorbed by device B1, where B2 and B3 absorbed 51.5% and 49.4% of the incident light respectively. The calculated values of light absorptance shows good agreement with device architecture as a thinner Al used in the translucent cathode will enhance the transmittance of the device, but sacrificing the light absorption of the active layer, resulting in a relatively low photogenerated current. On top of the effect of the light absorption variation in B1, B2 and B3, the decrease of the charge mobility from B1 to B3 investigated in the previous section is also one of the factors affecting the device performance in PSCs.

Table 6.2: Calculated integrated absorptance and short circuit current density of translucent PSCs B1, B2 and B3

	B1	B2	B3
AM1.5, $\bar{A}(\lambda)$ [*simulation*] (%)	58.0	51.5	49.4
Jsc (mA/cm^2)	8.27	6.60	5.99

In addition to the J-V characteristics, the lifetime measurements of the PSCs, B1, B2 and B3, were conducted under a continuous illumination of 100 hours using a simulated AM1.5 solar irradiation in N_2 glove box. The rate of change of PCE with illumination time is shown in Figure 6.6. The measurements were done in N_2 glove box with the purpose of eliminating the effect of moisture and oxygen on the stability

of the organic semiconductor during data analysis. Hence, the effect of oxygen and moisture can be neglected.

It has been observed that the stability of the PSCs decreases with the decrease of the Al thickness in the translucent cathode. The device stability studies indicates that the normalized PCE values dropped to 80%, 45% and 30% of their original values after 100 hours of continuous illumination for the devices B1, B2 and B3, respectively. The observed device stability results show a good agreement with the charge mobility characteristics obtained from PhotoCELIV studies as the charge mobility is also decreasing with the decrease of Al thickness. Another possible reason to explain the results obtained in Figure 6.6 might be due to the formation of Schottky barrier between the P3HT/Al interfaces, which enhances the photocharge generation [100]. Although it is generally understood that the exciton dissociation occurs efficiently at the donor/acceptor interface, the P3HT/Al interface is another possible sites for charge generation. The width of the Schottky barrier at the polythiophene/Al interface has also been reported to be 60 nm which translates to a built-in-field of 1.7×10^5 V/cm^2. This very high internal field helps to separate the excitons effectively at the polymer/Al interface [101]. Hence, most of the generated excitons are effectively separated as free charges within the Schottky barrier region in the polymer/Al interface. In this work, it is suggested that the translucent PSCs with lesser Al pure element at the polymer/Al interface weaken the internal field and leads to inefficient exciton dissociation and charge carrier collection. As a result, a relatively low PCE was obtained.

In general, the stability of conjugated polymer/fullerene based solar cell depends on several factors such as complicated photochemical and oxidative process between the donor-acceptor interface and at the organic-electrode interface [102]. In addition, the physical changes in the film morphology of the blend (i.e. the phase separation between the donor- acceptor) during the continuous illumination may also affect the charge separation and charge transport properties, thus the device stability is affected. It has already been reported that the interface between the ITO/polymer does not play a significant role in the performance of the degradation of the device under illumination [102]. In the polymer/Al interface, the direct chemical reduction of the organic constituents with Al electrode and the subsequent reaction with molecular oxygen may significantly influence on the lifetime of the devices. It is also well known that the Al atoms tend to form a covalent bond with thiophene by transferring an electron from Al to the carbon atoms and to the sulphur atoms of the thiophene unit [103]. This aluminum-polymer reaction process lead to a disruption of conjugation length of the polymer and destroy the material properties in terms of device performance mainly the lifetime will be affected. In this study, the enhanced stability of the B1 may suggest that the chemical reaction between the polymer and Al electrode or the interface properties have been modified by the light illumination. In addition to this interface modification, the electron collection may be easier as the bonding between Al and thiophene unit is stronger as compared with B2 and B3. In order to further understand the degradation mechanisms of the translucent PSCs with different Al thickness used, the electronic properties at the polymer/Al interface were studied by XPS.

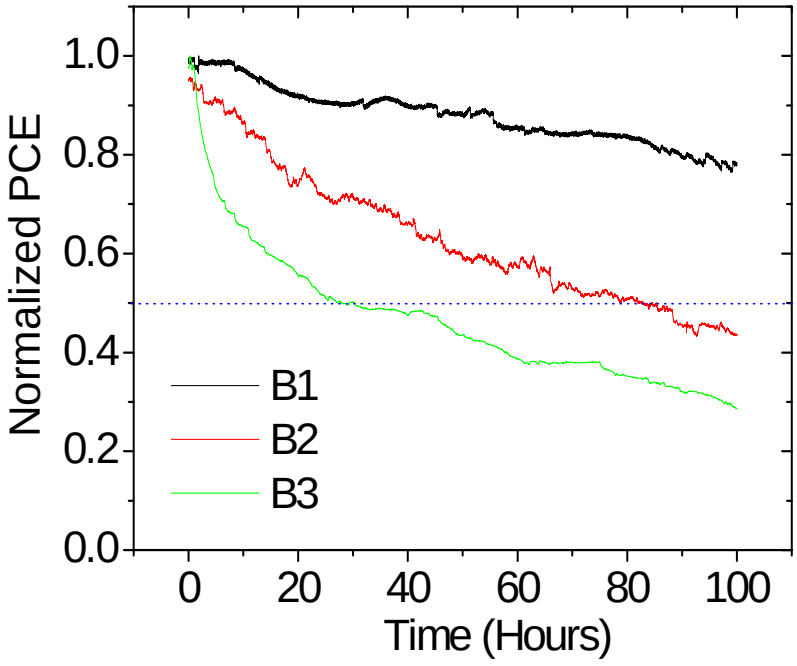

Figure 6.6: The changes of normalized PCE of B1, B2 and B3 over a period of 100 hours. The measurements were done under a continuous AM1.5G illumination of power intensity 100 mW/cm^2 in a N_2 glove box.

6.3 Polymer/Al Interfacial Properties for Translucent Polymeric Solar Cells with Different Al Thicknesses

The electronic properties at polymer/Al interface were studied by X-ray Photoelectron Spectroscopy (XPS) measurement. As shown in Figure 6.7, when 5nm of Al was used, the Al_{2p} peak was shifted to a higher binding energy (75.8eV) as compared to its elemental peak which is usually located at 73eV. This result suggested that the oxide phase formation is taking place in the polymer/Al interface. Further, there was no pure Al phase detected in this interface. For 10nm Al used in the translucent cathode, a very strong Al_{2p} elementary peak and a portion of oxide phase are detected, which suggested that the interface was a mixture of Al and AlO_x. The XPS results can be

used to explain the lowest PCE value obtained for the device B3 with Al(5nm)/ITO(60nm) translucent cathode compared to the other devices B1 and B2 with thick Al layer. In addition, the oxide formation in the active layer/Al interface was a possible factor to generate trap centers for electrons which eventually further catalysed the degradation of the cell. The pure Al detected in the polymer/Al(10nm) interface shows a better charge collection and lesser trap centers which makes the translucent PSC last longer.

The interfacial properties obtained from the XPS measurements are also consistent with the charge mobility data observed from the PhotoCELIV measurements, which was discussed in the previous section. The XPS studies showed that the oxide formation was higher with the 5nm Al electrode compared to the translucent PSCs with 10nm of Al. Therefore, the main reason for the observed lower charge mobility with the 5nm thickness of Al electrode may be assigned to the migration of oxide into the active polymer film which may trap the electrons. It was also observed that the PhotoCELIV transients for pure P3HT film with semitransparent device architecture shows single peak, which suggests that the interaction between the oxide and PCBM may be the main cause for the trapping of electrons in the translucent PSCs with thin Al electrode. The XPS results also show very good agreement with the translucent PSCs device efficiency as well as the device stability studies.

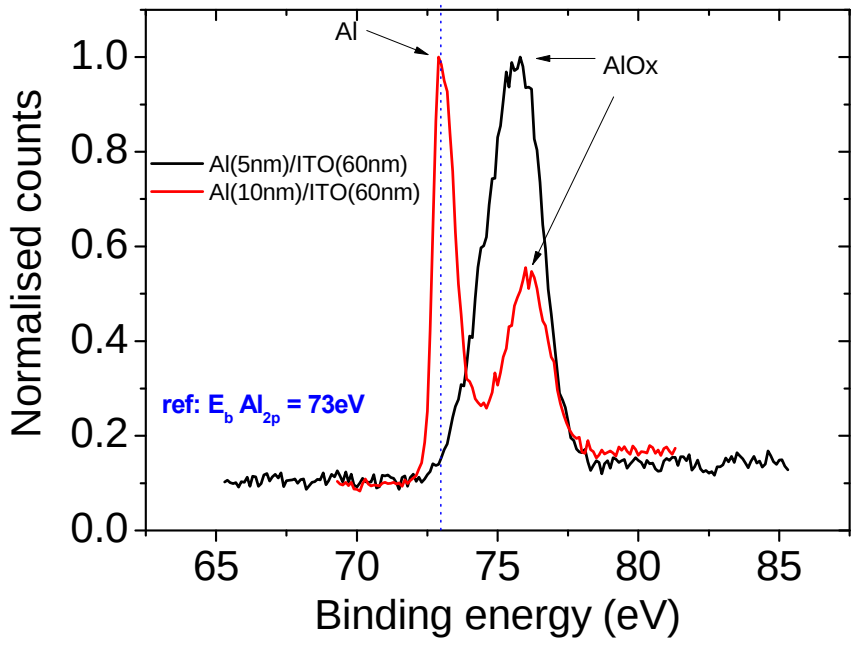

Figure 6.7: The chemical state of Al at the polymer/cathode interface with different Al thickness used in the translucent cathode.

6.4 Conclusion

In conclusion, the effect of translucent Al/ITO(60nm) cathode on the charge mobility properties, device performance and the polymer/cathode interfacial properties were investigated in detail. The charge mobility characteristics in translucent PSCs based on P3HT:PCBM film were studied using the PhotoCELIV technique. It was observed that the modifications in the electrode significantly influences on the charge mobility in the active material as the charge mobility in the translucent PSC (~$10^{-5}$$cm^2$/Vs) is almost one order of magnitude smaller than the charge mobility obtained for the conventional PSC (~$10^{-4}$$cm^2$/Vs). The translucent PSCs with very thin Al layer (5nm) show an additional PhotoCELIV peak which was assigned to the trapped electrons due to the interaction between the PCBM molecules and the migrated oxides into the film.

The device efficiency and stability of the translucent PSCs were also investigated and the results showed a similar trend as the device performance parameters (efficiency and lifetime) decreases with the reduction of Al thickness in the cathode. The interfaces between the photoactive layer/Al, by varying the thickness of the Al layer, were also studied using the XPS technique. The XPS results revealed that the oxide phase formation is taking place in the active layer/Al interface. The fully oxidized interface with Al thickness 5nm supports our observation of lower charge mobility, lower device efficiency and stability with the translucent PSCs with thin Al of 5nm.

The present investigation indicated that there is a need to search for a low work function, high transparency, and high conductivity cathode in order to achieve a stable and efficient translucent PSC. Translucent PSC serves as a building block for tandem PV configuration which realizes the stacking of two or more translucent PSCs in series to broaden the spectral absorption from the sunlight. The translucent PSC can be for applications in a variety of portable consumer electronics. The cells can also be made translucent and in different colors. These cells allow light to pass through, and yet absorb enough light to generate electricity. In the future, the see-through plastic solar cells can be used in buildings as windows that both shade and generate energy for our homes, offices and even greenhouses.

Chapter 7

Summary and Future Work

7.1 Summary

This work successfully developed a high performance translucent organic solar cell consisting of a front transparent anode, a stack of photoactive organic layers or blends that absorbs photons and converts them into electrons and holes, and an ITO-based transparent cathode. In order to optimize the absorption properties of such a thin film device, an optical admittance analysis method was used to investigate the optical response of the multilayer organic solar cells. The procedure was based on an optical admittance analysis that takes into account the interference effects in multilayer thin film systems. It enables one to calculate the optical properties of thin film organic solar cells to maximize usage of incident light radiation and also achieve the high transparency of the translucent organic solar cells.

A low process temperature high performance ITO-cathode was developed to improve the power conversion efficiency and the optical transparency of the solution-processed translucent P3HT:PCBM based solar cells. The high performance devices were prepared based on parameters obtained by optical admittance analysis. The performance of structurally identical PSCs made with a reflective metal cathode and ITO-based cathode is compared. For translucent PSCs with a 75 nm thick active P3HT:PCBM blend layer, an average transmission of more than 30% was achieved with a high PCE of 1.7% under simulated AM1.5G illumination of 100 mW/cm^2.

The results of this work also reveal that the optical simulation and the process optimization of ITO-based cathode are very important for the design and fabrication of high performance solution-processed PSCs. Translucent organic solar cell is a key component in fabricating tandem organic solar cells. The effect of the ITO interlayer thickness on the total transmittance and integrated absorptance of sub-cells in a tandem PSC was also analyzed. The results indicate that a maximum integrated transmission through a translucent bottom cell can be achieved at an ITO interlayer thickness of 50 nm, whereas the maximum light absorption occurred at an ITO interlayer thickness of 80 nm.

Following the successful demonstration of translucent PSC, the work was then expanded to study the solution-processed tandem PSCs. Optical admittance analysis was applied to calculate the photocurrent matching condition in tandem PSCs. The ITO-based cathode was used as a RZ connecting the two adjacent sub-cells in a tandem PSC. It also acted as a spacer layer to modify the light distribution in the tandem PSCs to achieve photocurrent matching condition. In this work, a 1.7 times enhancement in the Voc and an almost a double increase in PCE were achieved in tandem PSCs as compared to a single cell.

Cathode/organic material interface is crucial in organic solar cells and it plays an important role in determining both the performance and stability of organic photovoltaic devices. In this work, the effect of translucent Al(5-10nm)/ITO(60nm) cathode on the charge mobility properties, the polymer/cathode interfacial properties and the overall photovoltaic performance of the P3HT:PCBM-based PSCs was studied

using the PhotoCELIV and XPS techniques. It was observed that the charge mobility in the active region of the PSCs is dependent on the contact quality of Al/ITO(60nm) cathode on P3HT:PCBM layer. The PSCs with an Al(5nm)/ITO(60nm) had an additional PhotoCELIV peak which was assigned to the trapped electrons. These trapped electrons were formed due to the interaction between the PCBM molecules and the migrated metal oxides in P3HT:PCBM.

7.2 Future Work

Current silicon-based solar cells are very expensive thus limiting their applications. Organic and polymer-based bulk-heterojunction solar cells offer a potentially much cheaper alternative way to harness solar energy, considerable enhancement in device efficiencies are needed if this technology is to become a viable option for large scale energy production. To date, the best performing organic solar cells have reached power conversion efficiency of ~ 5% in a single cell, and ~ 7% in a tandem structure. However, the limited utilization of the solar energy, especially in the red part of the solar spectrum, and the relatively poor stability of current available OSCs are the two main factors hindering OSCs from commercialization. One of the possible solutions for this is to synthesize low band-gap semiconducting materials and incorporate them into a tandem OSC, where the individual sub-cells responds to different parts of the solar spectrum. Then, the PCE of the cell can be improved.

The solution-processed PSC technology developed in this work has the potential for application in a variety of consumer electronics, including digital electronics, automotive, outdoor lifestyle and home appliances. Further improvement

in the performance of solution-processed PSCs is required. The aspect of future work is to 1) develop more efficient semiconductors, 2) achieve microstructure control or molecular engineering of active semiconductor layer and 3) synthesize low band-gap semiconductor materials for application in solution-processed PSCs.

References

1. International Energy Agency. Key world energy statistics. Paris. (2006).
2. Intergovernmental Panel on Climate Change (IPCC). Forth Assessment Report - Climate Change 2007. Available: www.meto.gov.uk
3. Aleklett, Kjell. Dick Cheney, peak oil and the final count down. (2004, May 12). Available: www.peakoil.net
4. Chapin, D.M., Fuller, C.S., & Pearson, G.L. (1954). A new silicon p-n junction photocell for converting solar radiation into electrical power. Journal of Applied Physics, 25, 676.
5. Ginley, D.S., Green, M. A., & Collins, R.T. (2008). Harnessing materials for energy. MRS Bulletin, 33 (4), 355.
6. Slaoui, A., & Collins, R.T. (2007). Advanced inorganic materials for photovoltaics. MRS Bulletin, 32 (3), 211.
7. King, R. R., Law, D. C., Edmondson, K. M., Fetzer, C. M., Kinsey, G. S., Yoon, H., Sherif, R. A., & N. H. Karam. (2007). 40% efficient metamorphic GaInP/GaInAs/Ge multijunction solar cells. Applied Physics Letter, 90, 183516.
8. Element Distribution in the Earth's Crust. Available: http://chemistry.about.com/cs/howthingswork /f/blabundant.htm
9. Shaheen, S.E., Ginley, D.S., & Jabbour, G.E. (2005). Organic-based photovoltaics: toward low-cost power generation. MRS Bulletin, 30 (1), 10.
10. Günes, S., Neugebauer, H., & Sariciftci, N. S. (2007). Conjugated polymer-based organic solar cells. Chemical Reviews, 107, 1324.

11. Scharber, M., Mühlbacher, D., Koppe, M., Denk, P., Waldauf, C., Heeger, A. J., & Brabec, C. (2006). Design rules for donors in bulk-heterojunction solar cells - towards 10 % energy-conversion efficiency. Advanced Materials, 18, 789.
12. Burroughes, J. H., Bradley, D. D. C., Brown, A. R., Marks, R. N., Mackay, K., Friend, R. H., Burns, P. L., & Holmes, A. B. (1990). Light emitting diodes based on conjugated polymers. Nature, 347, 539.
13. Kallmann, H., & Pope, M. (1959). Photovoltaic effect in organic crystals. Journal of Chemical Physics, 30, 585.
14. Tang, C.W., & Albrecht, A.C. (1975). Photovoltaic effects of metalchlorophyll-a-metal sandwich cells. Journal of Chemical Physics, 62, 2139.
15. Chamberlain, G.A. (1983). Organic solar cells: A review. Solar Cells, 8, 47.
16. Wöhrle, D. & Meissner, D. (1991). Organic solar cells. Advanced Materials, 3, 129.
17. Peumans, P., Yakimov, A., & Forrest, S.R. (2003). Small molecular weight organic thin-film photodetectors and solar cells. Journal of Applied Physics, 93, 3693.
18. Maennig, B., Drechsel, J., Gebeyehu, D., Simon, P., Kozlowski, F., Werner, A., Li, F., Grundmann, S., Sonntag, S., Koch, M., Leo, K., Pfeiffer, M., Hoppe, H., Meissner, D., Sariciftci, S., Riedel, I., Dyakonov, V., & Parisi, J. (2004). Organic p-i-n solar cells. Applied Physics A: Materials Science & Processing, 79, 1–14.
19. Skotheim, T.A. (1986). Handbook of Conducting Polymer. Vol. 1-2, New York: Marcel Dekker, Inc.

20. Nalwa, H.S. (1997). Handbook of Organic Conductive Molecules and Polymers. Vol.1-4, Chichester, U.K.: John Wiley & Sons Ltd.

21. Skotheim,T.A., Elsenbaumer, R.L., & Reynolds, J.R. (1998). Handbook of Conducting Polymers. New York: Marcel Dekker, Inc.

22. Hadziioannou, G., & Hutten, P.F. (2000). Semiconducting Polymers. Weinheim: Wiley-VCH.

23. Morel, D.L., Gosh, A.K., Feng, T., Stogryn, E.L., Purwin, P.E., Shaw, R.F., & Fishman, C. (1978). High-efficiency organic solar cells. Applied Physics Letter, 32, 495.

24. Gosh, A.K., & Feng, T. (1978). Merocyanine organic solar cells. Journal of Applied Physics, 49, 5982.

25. Tang, C.W. (1986). Two-layer organic photovoltaic cell. Applied Physics Letter. 48, 183.

26. Ma, W., Yang, C., Gong, X., Lee, K., & Heeger, A. J. (2005). Thermally stable, efficienct polymer solar cells with nanoscale control of the interpenetrating network morphology. Advanced Functional Materials, 15, 1617.

27. Kim K.K., Liu, J.W., Namboothiry, M. A. G., & Carroll, D. L. (2007). Roles of donor and acceptor nanodomains in 6% efficient thermally annealed polymer photovoltaics. Applied Physics Letter, 90, 163511.

28. Koetse, M. M., Sweelssen, J., Hoekerd, T., Schoo, F. M., Veenstra, S. C., Kroon, J. M., Yang, X., & Loos, J. (2006). Efficient polymer:polymer bulk heterojunction solar cells. Applied Physics Letter, 88, 083504.

29. Kim, J. Y., Kim, S. H., Lee, H. H., Lee, K., Ma, W., Gong, X., & Heeger, A. J. (2006). New architecture for high-efficiency polymer photovoltaic cells using solution-based titanium oxide as an optical spacer. Advanced Materials, 18, 572.

30. Kietzke, T., Neher, D., & Hörhold, H. H. (2005). Efficient polymer solar cells based on M3EH-PPV. Chemistry of Materials, 17, 6532.

31. Hoppe, H., & Sariciftci, N. S. (2004). Organic solar cells: an overview Journal of Materials Research, 19, 1924.

32. O'Regan, B., & Graetzel, M. (1991). A low cost, high efficiency solar cell based on dye-sensitized colloidal TiO2 films. Nature, 353, 737.

33. Green, M.A., Emery, K., Büücher, K., King, D.L., Igari, S. (1998). Solar cell efficiency tables (Version 12). progress in photovoltaics: research and applications, 6, 265-270.

34. Peumans, P., Yakimov, A., & Forrest, S.R. (2003). Small molecular weight organic thin-film photodetectors and solar cells. Journal of Applied Physics, 93, 3693-3723.

35. Dresselhaus, M.S., Dresselhaus, G., & Eklund, P.C. (1996). Science of fullerenes and carbon nanotubes. San Diego, CA: Academic Press.

36. Lee, C.H., Yu, G., Moses, D., Pakbaz, K., Zhang, C., Sariciftci, N.S., Heeger, A.J., & Wudl, F. (1993). Sensitization of the photoconductivity of conducting polymers by C60 photoinduced electron transfer. Physical Review B, 48, 15425.

37. Morita, S., Zakhidov, A.A., & Yoshino, K. (1992). Doping effect of buckminsterfullerene in conducting polymer: Change of absorption spectrum and quenching of luminescene. Solid State Communications, 82, 249.

38. Morita, S., Kiyomatsu, S., Yin, X.H., Zakhidov, A.A., Noguchi, T., Ohnishi, T., & Yoshino, K. (1993). Doping effect of buckminsterfullerene in poly(2,5-dialkoxy-p-phenylene vinylene). Journal of Applied Physics, 74, 2860.

39. Sariciftci, N.S., Smilowitz, L., Heeger, A.J., & Wudl, F. (1992). Photoinduced electron transfer from a conducting polymer to buckminsterfullerene. Science, 258, 1474.

40. Braun, D., & Heeger, A.J. (1991). Visible light emission from semiconducting polymer diodes. Applied Physics Letter, 58, 1982.

41. Shinar, J. (2004). Organic light-emitting devices: a survey. New York: Springer.

42. Peet, J., Kim, J.Y., Coates, N.E., Ma, W.L., Moses, D., Heeger, A.J., & Bazan, G.C. (2007). Efficiency enhancement in low-bandgap polymer solar cells by processing with alkane dithiols. Nature Materials, vol 6, 497.

43. Marks, R. N., Halls, J. J. M., Bradley, D. D. C., Friend, R. H., Holmes, A. B. (1994). The photovoltaic response in poly(p-phenylene vinylene) thin-film devices. Journal of Physics: Condensed Mater, 6, 1379.

44. Barth, S., Bässler, H., Rost, H., Hörhold, H. H. (1997). Intrinsic photoconduction in PPV-Type conjugated polymers. Physical Review Letters, 79, 4445.

45. Miranda, P.B., Moses, D., Heeger, A. J. (2001). Ultrafast photogeneration of charged polarons in conjugated polymers. Physical Review B, 64, 81201.

46. Sariciftci, N.S., Smilowitz, A. J. Heeger, Wudl, F. (1992). Photoinduced Electron Transfer from a conducting polymer to bulkminsterfullerene. Science, 258, 1474-1476.

47. Brabec, C. J., Zerza, G., Cerullo, G., De Silvestri, S., Luzzati, S., Hummelen, J. C., & Sariciftci, N. S. (2001). Tracing photoinduced electron transfer process in conjugated polymer/fullerene bulk heterojunctions in real time. Chemistry Physics Letter, 340, 232.

48. Parker, I.D. (1994). Carrier tunneling and device characteristics in polymer light-emitting diodes. 75, 1656.

49. Geens, W., Aernouts, T., Poortmans, J., & Hadziioannou, G. (2002). Organic co-evaporated films of a PPV-pentamer and C60: Model systems for donor/acceptor polymer blends. Thin Solid Films, 403, 438.

50. Veenstra, S. C., Malliaras, G. G., Brouwer, H. J., Esselink, F. J., Krasnikov, V.V., van Hutten, P.F., Wildeman, J., Jonkman, H.T., Sawatzky, G.A., & Hadziioannou, G. (1997). Sexithiophene-C60 blends as model systems for photovoltaic devices. Synthetic Metals, 84, 971.

51. Peumans, P., Yakimov, A., & Forrest, S. R. (2003). Small molecular weight organic thin-film photodetectors and solar cells. Journal of Applied Physics, 93, 3693.

52. Hiramoto, M., Kishigami, Y., & Yokoyama, M. (1990). Doping effect on the two layer organic solar cell. Chemistry Letters, 19, 119.

53. Rostalski, J., & Meissner, D. (2000). Photocurrent spectroscopy for the investigation of charge carrier generation and transport mechanisms in organic p/n-junction solar cells. Solar Energy Materials and Solar Cells, 63, 37.

54. Halls, J. J. M., Pichler, K., Friend, R.H., Moratti, S.C., & Holmes, A.B. (1996). Exciton diffusion and dissociation in a poly(pphenylenevinylene)/C60 heterojunction photovoltaic cell. Applied Physics Letter, 68, 3120.

55. Halls, J. J. M., & Friend, R. H. (1997). The photovoltaic effect in a poly(p-phenylenevinylene)/perylene heterojunction. Synthetic Metals, 85, 1307.

56. Sariciftci, N.S., Braun, D., Zhang, C., Srdanov, V. I., Heeger, A. J., Stucky, G., & Wudl, F. (1993). Semiconducting polymerbuckminsterfullerene heterojunctions: Diodes, photodiodes, and photovoltaic cells. Applied Physics Letter, 62, 585 (1993).

57. Jenekhe, S.A., & Yi, S. (2000). Efficient photovoltaic cells from semiconducting polymer heterojunctions. Applied Physics Letter, 77, 2635 (2000).

58. Tsuzuki, T., Shirota, Y., Rostalski, J., Meissner, D. (2000). The effect of fullerene doping on photoelectric conversion using titanyl phthalocyanine and a perylene pigment. Solar Energy Materials and Solar Cells, 61, 1.

59. Uchida, S., Xue, J., Rand, B. P., & Forrest, S. R. (2004). Organic small molecule solar cells with a homogeneously mixed copper phthalocyanine: C60 active layer. Applied Physics Letter, 84, 4218.

60. Xue J., Uchida, S., Rand, B.P., & Forrest, S.R. (2004). 4.2% efficient organic photovoltaic cells with low series resistances. Applied Physics Leter, 84, 3013.

61. Li, Y. Q., Tan, L. W., Hao, X. T., Ong, K. S., Zhu, F.R., & Hung, L. S. (2005) Flexible top-emitting electroluminescent devices on polyethylene terephthalate substrates. Applied Physics Letter, 86, 153508.

62. Law, C. W., Lau, K. M., Fung, M. K., Chan, M. Y., Wong, F. L., Lee, C. S., & Lee, S. T. (2006). Effective organic-based connection unit for stacked organic light-emitting devices. Applied Physics Letter, 89, 133511.

63. White, M. S., Olson, D. C., Shaheen, S. E., Kopidakis, N., & Ginley, D. S. (2006). Inverted bulk-heterojunction organic photovoltaic device using a solution-derived ZnO underlayer. Applied Physics Letter. 89, 143517.

64. O'Connor, B., An, K. H., Pipe, K. P., Zhao, Y. Y. Y., & Shtein, M. (2006). Enhanced optical field intensity distribution in organic photovoltaic devices using external coatings. Applied Physics Letter, 89, 233502.

65. Xue, J., Uchida, S., Rand, B. P., & Forrest, S. R. (2004). Asymmetric tandem organic photovoltaic cells with hybrid planar-mixed molecular heterojunctions. Applied Physics Letter, 85, 5757.

66. Dennler, G., Prall, H. J., Koeppe, R., Eggiger, M., Autengruber, R., & Sariciftci, N. S. (2006). Enhanced spectral converage in tandem organic solar cells. Applied Physics Letter, 89, 073502.

67. Shrotriya, V., Wu, E. H. E., Li, G., Yao, Y. and Yang, Y. (2006). Efficient light harvesting in multiple-device stacked structure for polymer solar cells. Applied Physics Letter, 88, 064104.

68. Colsmann, A., Junge, J., Kayser, C., & Lemmer, U. (2006). Organic tandem solar cells comprising polymer and small-molecule subcells. Applied Physics Letter, 89, 203506.

69. Bailey-Salzman, R. F., Rand, B. P., & Forrest, S. R. (2006). Semitransparent organic photovoltaic cells. Applied Physics Letter, 88, 233502.

70. Gadisa, A., Tvingstedt, K., Admassi,e S., Lindell, L., Crispin, X., Andersson, M. R., Salaneck, W. R., & Inganäs, O. (2006). Transparent polymer cathode for organic photovoltaic devices. Synthetic Metals, 156, 1102.

71. Kawano K., Ito, N., Nishimori, T., & Sakai, J. (2006). Open circuit voltage of stacked bulk heterojunction organic solar cells. Applied Physics Letter. 88, 073514.

72. Gu, G., Bulovi, V., Burrows, P. E., Forrest, S. R., and Thompson, M. E. (1996). Transparent organic light emitting devices. Applied Physics Letter, 68, 2606.

73. Kim, J. Y., Lee, K. H., Coates, N. E., Moses, D., Nguyen, T. Q., Dante, M., & Heeger. A. J. (2007). Efficient tandem polymer solar cells fabricated by all-solution processing. Science, 317, 222.

74. Yakimov, A., & Forrest, S. R. (2002). High photovoltage multiple-heterojunction organic solar cells incorporating interfacial metallic nanoclusters. Applied Physics Letter, 80, 1667.

75. Peumans, P., Bulovic, V., Forrest, S. R. (2000).Efficient photon harvesting at high optical intensities in ultrathin organic double-heterostructure photovoltaic diodes. Applied Physics Letter, 76, 2650.

76. Lenes, M., Koster, L. J. A., Mihailetchi, V. D., Blom, P. W. M. (2006). Thickness dependence of the efficiency of polymer:fullerene bulk heterojunction solar cells. Applied Physics Letter, 88, 243502.

77. Mc Crackin, L.L., & Passaglia, E. (1963). Measurement of the thickness and refractive index of very thin films and the optical properties of surfaces by Ellipsometry. Journal of Research of the National Bureau of Standards – A. Physics and Chemistry, 67A, 363-377.

78. Muller, R.H. (1969). Defination s and Conventions in Ellipsometry. Surface Science, 16, 14-33.

79. The Nobel Prize in Physics 1981. Available: http://nobelprize.org/physics/laureates/1981/index.html.

80. Reference Solar Spectral Irradiance: Air Mass 1.5. Available : http://rredc.nrel.gov/solar/spectra/am1.5

81. Macleod, H A. Thin-film optical filters, 2nd ed. (1986). Bristol: Adam Hilger Ttd.

82. Zhu. F. R., Jennings. P., Cornish. J., Hefter. G.. & Luczak, K. (1997). Optimal optical design of thin-film photovoltaic devices. Solar Energy Materials and Solar Cells 49, 163.

83. Hoppe, H., Shokhovets, S., & Gobsch, G. (2007). Inverse relationship between photocurrent and absorption layer thickness in polymer solar cells. Physica Status Solidi, 1. 40.

84. Rand, B. P., Xue, J., Uchida, S., & Forrest, S. R. (2005). Mixed donor-acceptor molecular heterojunctions for photovoltaic applications. I. Material Properties. Journal of Applied Physics. 98, 124902.

85. Rand, B. P., Xue, J., Uchida, S., & Forrest, S. R. (2005). Mixed donor-acceptor molecular heterojunctions for photovoltaic applications. II. Device performance. Journal of Applied Physics. 98, 124903.

86. P. F. Carcia, R. S. Mclean, M. H. Reilly, Z. G. Li, L. J. Pillione and R. F. Messier. (2003). Influence of energetic bombardment on stress, resistivity, and microstructure of indium tin oxide films grown by radio frequency magnetron sputtering on flexible polyester substrates Journal of Vacuum Science & Technology A: Vacuum, Surfaces, and Films, 21, 745.

87. Cui, Y. R., & Xu, X. H. (1984). Deposition of transparent conducting indium tin oxide thin films by reactive ion plating. Thin Solid Films, 115, 195.

88. Coutal, C., Azema, A., and Roustan, J. C. (1996). Fabrication and characterization of ITO thin films deposited by excimer laser evaporation. Thin Solid Films, 288, 248.

89. Krokoszinski, H. J., & Oesterlein,R. (1990). Post-deposition annealing effects in electron-beam-evaporated indium tin oxide thin films. Thin Solid Films, 187, 179.

90. Zhu, F. R., Huan, C. H. A., Zhang, K., & Wee, A. T. S. (2000). Investigation of annealing effects on indium tin oxide thin films by electron energy loss spectroscopy. Thin Solid Films, 359, 244.

91. Morikawa, H., & Fujita,M. (2000). Crystallization and electrical property change on the annealing of amorphous indium-oxide and indium-tin-oxide thin films. Thin Solid Films, 359, 61.

92. Lee, D. Y., Lee, S. J., Song, K. M., & Baik, H. K. (2003). A study for the bias control of indium–tin–oxide films synthesized by cesium assisted radio frequency magnetron sputtering. Journal of Vacuum Science & Technology A: Vacuum, Surfaces, and Films, 21, 1069.

93. Ng, G. M., Kietzke, E.L., Kietzke, T., Tan, L.W., Liew, P.K., & Zhu, F. R. (2007). ITO-based Cathode for Application in Semitransparent Organic Photovoltaic Cells. In: Symposium Z, 2007 MRS Spring Meeting, San Francisco, April 9-13.

94. Ng, G. M., Kietzke, E.L., Kietzke, T., Tan, L.W., Liew, P.K., & Zhu, F. R. (2007). Optical enhancement in semitransparent polymer photovoltaic cells. Applied Physics Letter, 90, 103505.

95. Xue, J. G., & Forrest,S. R.. (2003). Organic optical bistable switch. Applied Physics Letter, 82, 136

96. Ohmori, Y., Kajii, H., Kaneko, M., Yoshino, K., Ozaki, M., Fujii, A., Hikita, M., Takenaka, H., & Taneda, T. (2004). Realization of polymeric optical integrated devices utilizing organic light-emitting diodes and photodetectors fabricated on a polymeric waveguide. IEEE Journal of Selected Topics in Quantum Electronics, 10, 70.

97. Sirringhaus, H., Brown, P. J., Friend, R. H., Nielsen, M. M., Bechgaard, K., Langeveld-Voss, B. M. W., Spiering, A. J. H., Janssen, R. A. J., Meijer, E. W., Herwig, P., & Leeuw, D. M. (1999). Two-dimensional charge transport in self-organized, high-mobility conjugated polymers, Nature, 401, 685..

98. Inigo, A.R., Tan, C. H., Fann, W., Huang, Y. S., Perng, G. Y., & Chen, S. (2001). Non-dispersive Hole Transport in a Soluble Poly(p-phenylene vinylene), Advanced Materials, 13, 504.

99. Chen, Z. K., Lee, N. H. S., Huang, W., Xu, Y.S., & Cao, Y. (2003). New phenyl-substituted PPV derivatives for polymer light-emitting diodes-synthesis, characterization and structure-Property Relationship Study. Macromolecules, 36, 1009.

100. Pandey, S. S., Nagamatsu, S., Takashima, W., & Kaneto, K. (2000). Mechanism of Photocarrier Generation and Transport in Poly(3-Alkylthiophene) Films. Japanese Journal of Applied Physics. 39, 6309.

101. Kaneto, K., Takayama, K., Takashima, W., Endo, T., & Rikukawa, M. (2002). Photovoltaic effect in schottky junction of poly(3-alkylthiophene)/Al with various alkyl chain lengths and regioregularities. Japanese Journal of Applied Physics. 41, 675.

102. Krebs, F. C., Carlé, J. E., Cruys-Bagger, N., Andersen, M., Lilliedal, M. R., Hammond, M. A., & Hvidt, S. (2005). Lifetimes of organic photovoltaics: photochemistry, atmosphere effects and barrier layers in ITO-MEHPPV:PCBM-aluminium devices. Solar Energy Materials & Solar Cells, 86, 499–516.

103. Lazzaronia, R., Lögdlund, M., Calderone, A., Brédas, J. L., Dannetun, P., Fauquet, C., Fredriksson, C., Stafström, S., & Salaneck, W. R. (1995). Chemical and electronic aspects of metal/conjugated polymer interfaces. Implications for electronic devices. Synthetic Metals, 71, 2159-2162.

104. Parthasarathy, G., Adach, C., Burrows, i, P. E., and Forrest, S. R. (2000). High-efficiency transparent organic light-emitting devices. Applied Physics Letter, 76, 2128-2130.

105. Chen, H. Y., Qiu, C. F., Wong, M., and Kwok, H. S. (2003). DC sputtered indium-tin oxide transparent cathode for organic light-emitting diode. IEEE Electron Device Letters, 24, 315-317.

106. Choi, H. W., Kim, S. Y., Kim, K. B., Heung, Y. H., and Lam, T. J. (2005). Enhancement of hole injection using O_2 plasma-treated Ag anode for top-emitting organic light-emitting diodes. Applied Physics Letters, 86, 012104.

107. Juška, G., Arlauskas, K., & Viliūnas, M., Kočka, J. (2000). Extraction current transients: new method of study of charge transport in microcrystalline silicon. Physical Review Letters, 84, 4946.

108. Juška, G., Arlauska, K., Viliūnas, M., & Genevičius, K., Österbacka, R., & Stubb, H. (2000). Charge transport in π-conjugated polymers from extraction current transients. Physical Review B, 62, R16235.

109. Dennler, G., Mozer, A.J., Juška, G., Pivrikas, A., Österbacka, R., Fuchsbauer, A., Sariciftci, N.S. (2006). Charge carrier mobility and lifetime versus composition of conjugated polymer/fullerene bulk-heterojunction solar cells. Organic Electronics, 7, 229.

110. Mozer, A. J., Sariciftci, N. S., Lutsen, L., Vanderzande, D., Österbacka, R., Westerling, M, Juška, G. (2005). Charge transport and recombination in bulk heterojunction solar cells studied by the photoinduced charge extraction in linearly increasing voltage technique. Applied Physics Letters, 86, 112104.

111. Sliaužys, G., Juška, G., Arlauskas, K., Pivrikas, A., Österbacka, R., Scharber, M., Mozer, A., Sariciftci, N.S. (2006). Recombination of photogenerated and injected charge carriers in π-conjugated polymer/fullerene blends. Thin Solid Films, 511, 224.

112. Katiyar, M., Yang, Y.H., & Ableson, J.R. (1995). Hydrogen-surface reactions during the growth of hydrogenated amorphous silicon by reactive magnetron sputtering: A real time kinetic study by in situ infrared absorption. Journal of Applied Physics. 77, 6247.